SEPARATION CONTROL OVER LOW PRESSURE TURBINE BLADES USING PLASMA ACTUATORS

A Dissertation

Submitted to the Graduate School

of the University of Notre Dame

in Partial Fulfillment of the Requirements

for the Degree of

Doctor of Philosophy

by

Junhui Huang, B.E., M.E., & M.S.

Thomas C. Corke, Director

Graduate Program in Aerospace & Mechanical Engineering

Notre Dame, Indiana

July 2005

SEPARATION CONTROL OVER LOW PRESSURE TURBINE BLADES USING PLASMA ACTUATORS

Abstract

by

Junhui Huang

This work involved the documentation and control of flow separation that occurs over low pressure turbine (LPT) blades at low Reynolds numbers. A specially constructed linear cascade was utilized to study the flow field over a generic LPT cascade consisting of Pratt & Whitney "PakB" shaped blades. Flow visualization, pressure measurements, LDV measurements, and hot-wire measurements were conducted to examine the flow fields with and without separation control. Experimental conditions were chosen to give a range of chord Reynolds numbers from $10,000$ to $100,000$, and a range of freestream turbulence intensities from $u'/U_\infty = 0.08\%$ to 2.85%.

The blade pressure distributions were measured and used to define a region of separation that depends on the freestream conditions. The location of separation was found to be relatively insensitive to the experimental conditions. However, the reattachment location was very sensitive to the Reynolds number and the turbulence intensity.

Separation control was performed using plasma actuators. Both steady and unsteady actuation were implemented and found to work well. For the steady actuators, it was found that the separation control is the most effective when applied slightly upstream the separation location. There exists a threshold plasma ampli-

tude for the actuator to take effect for separation control. However, the effectiveness of the actuator is saturated when the plasma amplitude is greater than certain value. The effectiveness of the steady actuator is not sensitive to the orientation of the plasma electrodes. For the unsteady actuators, there exists an optimum excitation frequency at which the unsteady actuator was the most effective. The optimum excitation frequency was corresponded to the unity Strouhal number, which is defined as $S_t = f L_{sep}/U_{mid-channel}$. It was also found that lowest plasma duty cycle (10% in this work) was as effective as the highest plasma duty cycle (50% in this work). This has an advantage for reducing the power to the actuators.

The comparison between the steady and unsteady actuators showed that the unsteady actuators worked better than the steady ones. The mechanisms of the steady and unsteady plasma actuators were studied. It was suggested by the experimental results that the mechanism for the steady actuators is turbulence tripping, while the mechanism for the unsteady actuators is to generate a train of spanwise structures that promote mixing.

CONTENTS

TABLES

FIGURES

SYMBOLS

Symbol	Meaning
C	blade chord length
C_x	axial chord length
C_p	pressure coefficient $((p - p_\infty)/(\frac{1}{2}\rho U_\infty^2))$
$FSTI$	freestream turbulence intensity (u'/U_∞)
L_{sep}	length of separation region
L_{ss}	length of suction surface
M	mesh of grids
Re_c	Reynolds number based on axial chord length and inlet velocity
Re_{ss}	Reynolds number based on suction surface length and exit velocity
S	spacing between two blades
S_t	Strouhal Number $(fL_{sep}/U_{mid-channel})$
Tu, TI	turbulence intensity (u'/U_∞)
U_∞	freestream velocity
U_c	convection velocity of spanwise vortices
$U_{mid-channel}$	local freestream velocity in the blade passage
e	elementary charge
$\vec{f}$	body force generated by plasma actuators
f	excitation frequency of unsteady actuator
kT_e, kT_i	electron and ion temperatures
p	static pressure

q	dynamic pressure
s	surface coordinate
u, v	velocity components
u', v'	rms velocity components
x, y	axial coordinates
z	spacing of vortex generator tabs
β	duty cycle of plasma during unsteady pulsing
γ	stagger angle of "PakB" blades (26°)
δ	boundary layer thickness
ϵ_0	permittivity of free space (8.854×10^{-12} F/m)
λ	Debye length
ρ	density of air, net charge density of plasma

CHAPTER 1

MOTIVATION AND BACKGROUND

1.1   Motivation

Turbine engines are usually designed for peak performance at high Reynolds number conditions, such as taking off and landing. But during high altitude cruise, the operating Reynolds number for the low pressure turbine (LPT) in an aircraft gas turbine engine can drop below 25,000 due to the low air density. The optimally designed engines for high Reynolds number conditions may perform poorly under various off-design conditions and have a substantial loss of engine efficiency. Sharma [24] indicated a nearly 300% rise in the loss coefficient at Reynolds numbers below 95,000 compared to that at higher Reynolds numbers (see Figure 1.1). The high total pressure loss at low Reynolds numbers is primarily associated with a laminar separation over the trailing half of the blade suction surface.

A solution to this problem is to apply a control method to eliminate the flow separation that occurs on the LPT blade at low Reynolds numbers. The simplest way is to apply vortex generators to the blade surface. These devices are small plates mounted on the blade surface to generate a pair of asymmetric streamwise vortices, which introduce high momentum fluid down to the blade surface and mix them with low momentum fluid, thus preventing flow separation. Vortex generators are easy to use and effective in separation control. However, they cannot be "turned off" and will cause parasitic drag when not needed. This is also a drawback for all
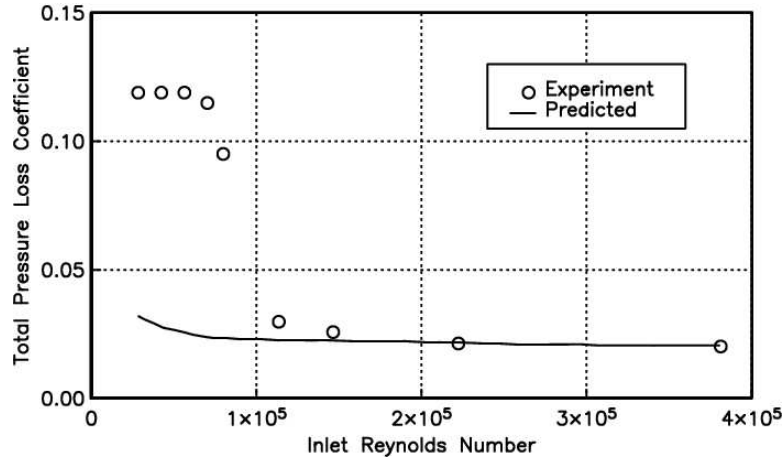
Figure 1.1. Pressure loss of LPT vs. Reynolds number (from Sharma [24]).

passive control methods. For this reason, active control methods are preferred to passive ones. One of the active control methods is vortex generator jets (VGJs). When operated, the VGJs generate streamwise vortices on the blade surface, just as the passive vortex generators do. The vortices mix the low and high momentum fluids together to prevent flow separation. Active control methods can be shut down when not needed. However, they have disadvantages too. For example, most of the active control methods require additional power and/or weight.

1.2   Review of Separation Control

Separation occurs when the flow does not have sufficient momentum to over-come the adverse pressure gradient and the viscous dissipation along the flow path. Separation control methods are designed to augment the momentum level of the flow. These methods can be categorized as passive methods and active methods. Passive techniques have the advantage of requiring neither additional power nor additional weight. However, a passive control strategy which is successful at low Reynolds number may increase the blade's drag at higher Reynolds numbers. On

TABLE 1.1

TYPICAL SEPARATION CONTROL METHODS

Control Method	Category	Mechanism
Trips	Passive	Causing Boundary Layer Transition to Turbulent
Roughness	Passive	Causing Boundary Layer Transition to Turbulent
Vortex Generators	Passive	Boundary Layer Mixing
Bumps and Dimples	Passive	Boundary Layer Mixing
Boundary Layer Suction	Active	Removal of Low-Momentum from Near-Wall Flow
Leading Edge Flap	Active	Momentum Addition to Near-Wall Flow
Tangential Steady Blowing	Active	Momentum Addition to Near-Wall Flow

the contrary, active techniques can be shut off when not required. This is especially desired for turbine applications. Table 1.1 lists several typical separation control methods and their mechanisms.

Control of flow separation has been extensively studied for decades. Bearman and Harvey [1] used dimples to control the circular cylinder flow. Lin et al. [?] conducted experiments to evaluate boundary separation control on a two-dimensional single-flap, three-element, high-lift system with small surface-mounted vortex generators. The effectiveness of vortex generators of different sizes were investigated. It was found that vortex generators as small as 0.18% of total chord installed on the flap can effectively control flap separation. Both counter-rotating and co-rotating streamwise vortices generated by vortex generators were effective in reducing flow separation on the flap. An in-depth review of boundary layer separation control using vortex generators is presented by Lin [?]. Johnston and Nishi [?] explored the capability of separation control of a turbulent boundary layer on a flat plate using vortex generator jets. Spanwise arrays of small, skewed, and pitched jets were employed to generate streamwise vortices. It was found that the skewed jets were

effective in separation control. But when the jets pointed directly upstream, they were ineffective. The reattachment location seemed more strongly affected than the separation location. Compton and Johnston [?] conducted similar experiments and found that the maximum vorticity levels are strongly dependent on the jet velocity and the skew angle, and an optimal jet skew angle to be between 45° and 90°.

Narayanan et al. [?] performed a control experiment on the wall-bounded separation by using a jet and examined the proper frequency condition for separation control. Rixon and Johari [?, ?] studied the development of a steady vortex generator jet in a turbulent boundary layer using Particle Image Velocimetry (PIV). The jet was pitched 90° and skewed 45°. They found that the jet created a pair of streamwise vortices. One of them was stronger and dominated the flow field. The circulation, peak vorticity, and wall-normal position of the primary vortex increased linearly with the jet velocity.

Magill and McManus [?] demonstrated the separation control using pulsed vortex generator jets (PVGJs) on a fighter configuration with swept wings and a transonic airfoil section. It was found that the PVGJs can enhance the lift of the fighter configuration in post-stall flight. For the transonic airfoil section, the PVGJs can increase the lift and lift-to-drag ratios, but they were less effective at supercritical speeds. Jiang et al. [?] carried out the direct numerical solutions for separation control with pulsed jets. They studied the role of the Kelvin-Helmholtz instability mechanism in the wing separation. The instability was found to dominate from the leading edge to the trailing edge. Seifert et al. [?] conducted experiments on four different airfoils to examine the control effect using oscillatory blowing. It was found that the oscillatory blowing can delay separation from a symmetric airfoil much more effectively than the steady blowing. It was also found that blowing from the flap shoulder was more effective than blowing at the leading edge, provided

the flow separated from the flap and not from the main body of the airfoil. The most effective excitation frequency seemed to be the one that gave a unity reduced frequency based on the distance between the actuator and the trailing edge of the airfoil.

Separation control using Lorentz force has been presented by Weier et al. [?]. In their experiment, the Lorentz force was generated by using a strip-wise arrangement of electrodes and permanent magnets of alternating polarity and magnetization. Separation control by Lorentz force was demonstrated in a saltwater flow passing an inclined flat plate. The flat plate was set at an angle of attack of 18°. Flow visualization showed that the flow separated from the leading edge of the plate when Lorentz force was off. When Lorentz force was on, the flow was attached on the whole range of the suction side. This control method was also applied to two airfoils similar to a NACA-0017 airfoil. The lift and the drag was measured using a force balance. It was found that when electromagnetic forces of sufficient strength was applied, stall was delayed to higher angles of attack resulting in an increase in maximum lift and a decrease in total drag of the airfoils. Nishizawa et al. [?] developed a self-contained, close-loop control system to control the flow separation on a downward slope. Their control system consisted of a separation detector, an actuator, and a control algorithm. The separation detector was a MEMS based cantilever sensor, which could detect the flow direction. The actuator was made of a speaker, which could generate sinusoidal fluctuations. Unsteady actuation was employed and the excitation frequency was chosen to be 100 Hz. The actuation was applied far upstream the separation location. It was demonstrated that the speaker actuation eliminated the flow separation according to the hot-wire measurements. However, the actuation only worked well when the freestream velocity was greater than 10 m/s. When the freestream velocity was less than 10 m/s, on the contrary,

the actuation caused a larger separation bubble.

1.3   Review of Low Pressure Turbine Research

The aim of this research work is focused on the documentation and control of the flow separation on low pressure turbine blades that occurs at low Reynolds numbers. Many similar research works have been done in the past decade. Sohn et al. [27, 28] and Shyne et al. [26] conducted thorough experiments to study the boundary layer on the suction surface of LPT blades. Figure 1.2 shows their experimental setup. A contoured top wall was designed to give the same pressure distribution over the bottom flat plate as that of a LPT blade. They examined the effects of the Reynolds number and the freestream turbulence intensity (FSTI) on the flow separation and the transition of the boundary layer. Table 1.2 summarizes the results of their experiment. In this table, "S" means the flow separation was observed and "T" means the transition from laminar to turbulent was observed.
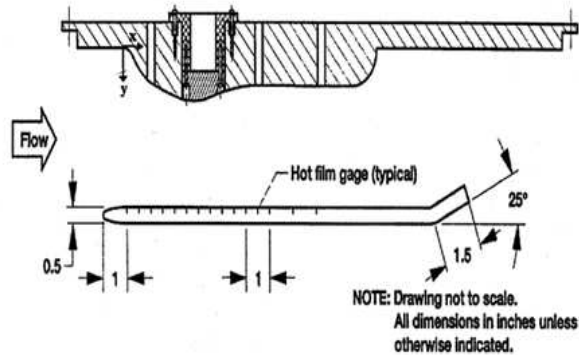
Figure 1.2. The experimental setup of Sohn [27]'s experiment.

Figure 1.3 shows a picture taken from the flow visualization for $Re_{ss} = 50,000$ and FSTI=1%. A separation bubble on the bottom flat plate (simulated suction surface) is clearly seen. It was found that the front part of the separation bubble was

TABLE 1.2

SUMMARY OF SOHN [27]'S EXPERIMENT

	Re_{ss}=35,000	Re_{ss}=70,000	Re_{ss}=100,000	Re_{ss}=250,000
FSTI=1.0%	S,T	S,T	S,T	T
FSTI=2.0%	S,T	S,T	S,T	T
FSTI=3.0%	S,T	S,T	S,T	T
FSTI=4.0%	S,T	S,T	(Not Done)	(Not Done)

laminar and steady. However, the transition and the reattachment processes were unsteady. Figure 1.4 shows the pressure distribution along the flat plate. There is a nearly-constant region in the pressure profiles. This nearly-constant region was identified as the front part of the separation bubble. For all the cases where the flow separation was observed, the boundary layer separated as a laminar one and transitioned to turbulent some distance downstream of the separation point. As the Reynolds number increased, the separation onset location slightly moved downstream while the transition onset location moved upstream. As the freestream turbulence intensity increased, the transition onset point moved forward toward the leading edge, and the transition length shrank. However, it seemed that the freestream turbulence intensity had little or no effect on the separation onset location. The transition onset point and end point moved upstream as FSTI increased. The transition length also decreased as FSTI increased.

Halstead et al. [8, 9, 10, 11] performed both experimental and numerical research to understand boundary layer development on airfoil surfaces in multistage, axial-flow compressors and low pressure turbines (LPTs). For both compressor and turbine blading, the experimental results showed large extents of laminar and transitional flow on the suction surface of embedded stages, with the boundary layer generally
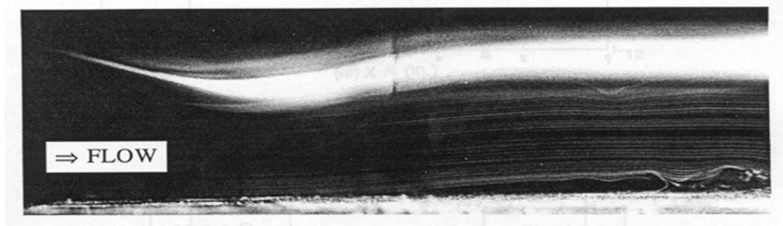
Figure 1.3. The flow visualization of the separation bubble (from Sohn [27]).
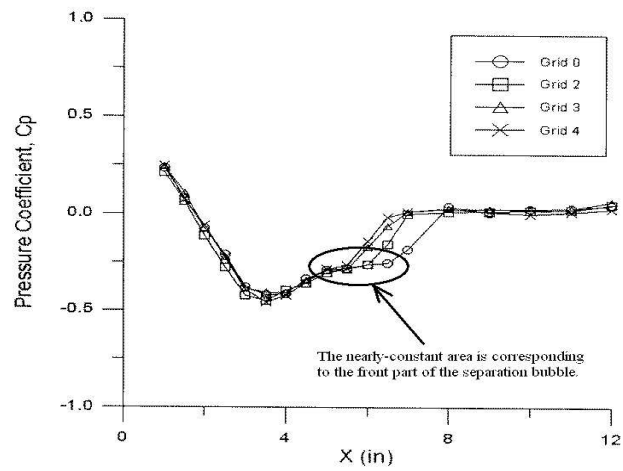
Figure 1.4. The pressure distribution over the flat plate (simulated suction surface) for Re_{ss}=70k (from Sohn [27]).

developing along two distinct but coupled paths: one lied approximately under the wake trajectory while the other lied between wakes. The wake path and the non-wake path were coupled by a calmed region which was effective in suppressing flow separation and delaying transition in the non-wake path. In their experiments, both bypass transition and separated-flow transition were observed, while classical Tollmien-Schlichting transition did not play a significant role.

Qiu et al. [22] studied the flow over a low pressure turbine blade in a cascade simulator (see Figure 1.5). Their work was focused on the flow separation and the transition of the boundary layer (or shear layer in case of separation) from laminar to turbulent. Four Reynolds numbers (Re_{ss}=50,000, 100,000, 200,000, and 300,000) and three freestream turbulence intensities (FSTI=0.5%, 2.5%, and 10%) were examined in their experiment. Table 1.3 summarizes the results of their experiment. Again, in this table, "S" means the separation was observed and "T" means the transition was observed.
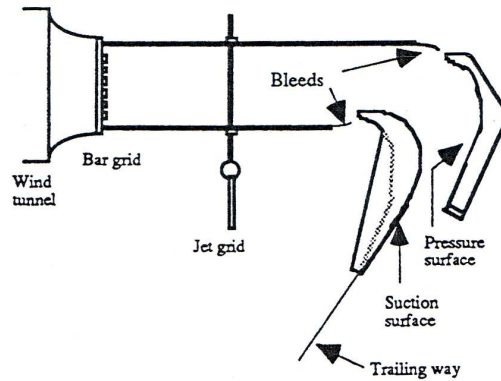
Figure 1.5. The cascade simulator from Qiu [22]'s experiment.

The flow for $Re_{ss} = 100,000$ and FSTI=2.5% was discussed in detail. The pressure distributions and boundary layer velocity profiles showed that, for this case,

TABLE 1.3

SUMMARY OF QIU [22]'S EXPERIMENT

	Re_{ss}=50,000	Re_{ss}=100,000	Re_{ss}=200,000	Re_{ss}=300,000
FSTI=0.5%	S	S,T	S,T	S,T
FSTI=2.5%	S,T	S,T	S,T	T
FSTI=10.0%	S,T	S,T	T	(Not Done)

the flow separated between $x/C_x = 69\%$ and 74%. The boundary layer was laminar from the leading edge to the separation location. Then the separated shear layer transitioned to turbulent. Finally the flow reattached to the blade near the trailing edge. They observed the flow transition in all cases they examined except for one (Re_{ss}=50,000 and FSTI=0.5%). The speed with which the boundary layer completed the transition increased as the Reynolds number and freestream turbulence intensity increased.

Hollon et al. [12, 13] used the smoke wire and Digital Particle Image Velocimetry (DPIV) techniques to study the flow in a cascade of "PakB" blades. The Reynolds number varied from Re_{ss}=30,000 to 90,000. The locations of separation and transition were determined to be approximately 45% and 77% of the suction surface length, respectively, and appeared to be independent of Reynolds number, turning angle, and the freestream turbulence intensity. Lake et al. [16] investigated the flow separation over Pratt & Whitney shaped "PakB" blades. Three Reynolds numbers ($Re_c = 50,000, 100,000,$ and $200,000$) and two turbulence intensities (FSTI=1% and 4%) were studied. The separation area extended from $70\%C_x$ to the trailing edge of the suction side when $Re_c = 50,000$ and FSTI=1%. When the Reynolds number and/or the turbulence intensity increased, the extent of the separation bubble decreased. Schobeiri et al. [?] conducted experiments to study the effect of the

unsteady inlet flow on the flow separation and the boundary layer transition on low pressure turbine blades. Special wake generators were designed and built to produce unsteady inlet flow conditions with different passing frequency, wake velocity, and turbulence intensity. One steady and two unsteady inlet flow conditions were studied. Surface pressure measurements were conducted for four different Reynolds numbers (Re_{ss} = 50,000, 75,000, 100,000, and 125,000). It was found that unsteady inlet flow conditions decreased the separation zone on the blade. Passing the wake flow with its highly turbulent vortical core over the separation region caused a periodic contraction and expansion of the separation zone. It was proposed that, in conjunction with the pressure gradient and periodic wakes, the temporal gradient of the turbulence fluctuation provided high momentum and energy transfer into the boundary layer energizing the separation zone and causing it to partially or entirely disappear.

In addition to a large amount of experimental work on the boundary layer development over the LPT blades, there are also some numerical simulations in this area. Dorney et al. [6, 7] solved both thin-layer and full Navier-Stokes equations for a low pressure turbine geometry. In their research, two turbulence models (a modified Baldwin and Lomax model and a two-equation $k - \epsilon$ model) were used. Reynolds numbers varied from Re_c=40,000 to Re_c=120,000, and the turbulence intensity varied from 3% to 6%. Laminar, turbulent, and transitional simulations were performed. It was found that the Mach number distribution showed good agreement to the design intent for both turbulent and transitional simulations. The predicted losses and efficiency were highly dependent on the assumed state of the boundary layers (laminar, turbulent, or transitional). Huang et al. [15] made use of empirical correlations to predict both separated-flow and attached-flow transition. Suzen et al. [30] developed a new intermittency transport equation in a numerical simulation of

the flow around LPT blade. The intermittency was taken into account by modifying the eddy viscosity with the intermittency factor. The Reynolds numbers varied from Re_{ss}=50,000 to Re_{ss}=300,000, and the turbulence intensities varied from 2.5% to 10%. It was found that the onset of transition moved upstream when the Reynolds number and/or the turbulence intensity increased. The size of separation bubble decreased as the Reynolds number and/or the turbulence intensity increased.

Some effort has been devoted to control the flow separation over LPT blades. Byerley et al. [4] used Gurney flaps to control laminar separation on a linear cascade of seven "Langston" blades. "A Gurney flap is a mechanically simple device consisting of a short, flat plate attached to the pressure side of an airfoil near the

Figure 1.6. The "Langston" blade with a Gurney flap attached to the pressure surface near the trailing edge (from Byerley [4]).

trailing edge" [4] (see Figure 1.6).

Five different sizes of Gurney flaps were tested. Laser thermal tuft technique and pressure measurement were employed. Three Reynolds numbers ($Re_c = 28,000$, $65,000$, and $167,000$) and one turbulence intensity (FSTI=0.8%) were examined. Flow separation was observed under two lower Reynolds numbers. The second largest Gurney flap completely eliminated separation under the lowest Reynolds number (Re_c=28,000). However, the Gurney flaps increased the loss coefficient for all Reynolds numbers above 28,000, which indicated the need to retract the Gurney

flap for the cases when Reynolds number is high enough that separation is not present.

Lake et al. [16] introduced the dimples into the LPT blades. The dimples were cut into the suction side of the blade to a depth of 1.588 mm. ($\frac{1}{16}$ in.) using a 5.08 cm. (2 in.) diameter ball end mill. The dimples were 2.22 cm. (0.875 in.) apart center-to-center. They found this method reduced the loss coefficient by 58% at the lowest Reynolds number ($Re_c = 50,000$) without incurring much penalties at higher Reynolds numbers. Lake et al. [17] evaluated the effectiveness of both v-grooves and dimples to control boundary layer separation on the "PakB" turbine blade. They demonstrated that dimples were effective across a wide range of Reynolds numbers and freestream turbulence intensities because they generated streamwise vortices.

Bons et al. [2] examined the control effect of vortex generator jets (VGJs) on LPT blade separation. The jet holes were located at $73\%C_x$. They had a pitch angle of $30°$ and a skew angle of $90°$ (see Figure 1.7). The diameter of the jet holes was 1 mm. and the spacing between every two holes was 10 mm. This configuration could generate single, dominant, slowly-decaying streamwise vortex per hole. It was shown that this single-sign vortex energized the separating boundary layer by effectively bringing high momentum freestream fluid down to the wall, hence postponing the boundary layer separation. Pressure distributions over the suction and pressure surfaces, velocity profiles in the boundary layer, and the wake profiles were documented. The effects of the blowing ratio B, Reynolds number Re_c, and the freestream turbulence intensity FSTI were studied. The separation region at low Reynolds number was found to be much larger than that at higher Reynolds numbers. When the jets were blowing, the separation point was postponed from $73\%C_x$ to after $79\%C_x$. The wake velocity profile became narrower and shallower than that without blowing. The control ability of the VGJs was verified by the

integrated momentum deficit θ_{def} which is defined as

$$\theta_{def} = \int \frac{u}{U_{local}} \left(1 - \frac{u}{U_{local}}\right) dy. \tag{1.1}$$

Figure 1.8 shows the momentum deficit θ_{def} for the ASC blade (the blade with VGJs) as a function of the blowing ration B. The momentum deficit was reduced about 65% for blowing ratio $B=1$. However, there was little change in the benefit of control up to $B=4$. There existed a threshold value of B for VGJs to have considerable effect on flow control. It was suggested this threshold value was related to the location of the jet holes. At high Reynolds numbers or high freestream turbulence intensities, the jet blowing had little obvious effect.
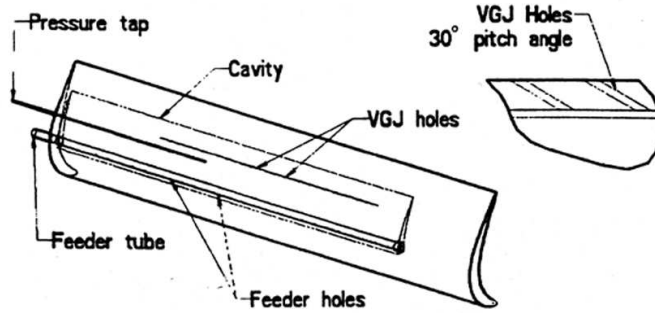
Figure 1.7. The active separation control (ASC) blade geometry (from Bons [2]).

In addition to steady vortex generator jets, pulsed vortex generator jets were also employed by Bons [3] to control the flow separation over LPT blades. In their experiment, two spanwise rows of jet holes were used, at $45\%C_x$ and $63\%C_x$, respectively. The jet holes have a diameter of 1 mm. and a spacing of 10 mm. Again, the jet holes had a pitch angle of 30° and a skew angle of 90°.

The forcing frequency was varied from 10 Hz to 100 Hz but it was found that the bulk effect on separation appeared to be insensitive to the frequency. The
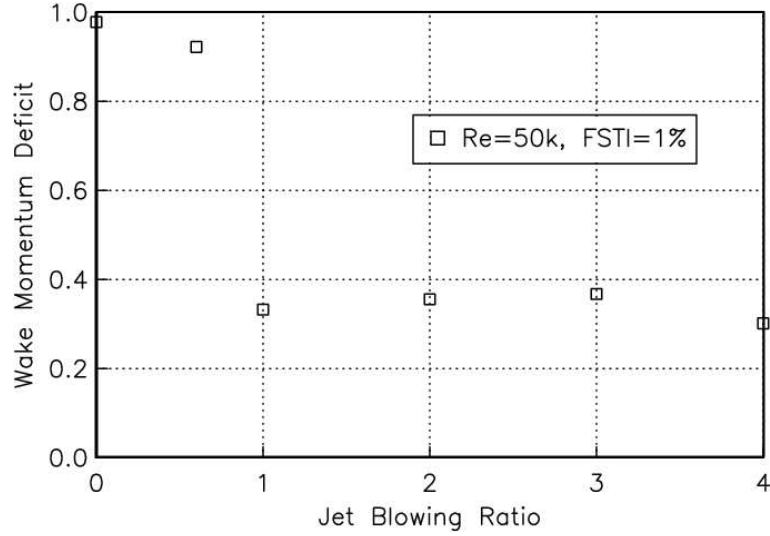
Figure 1.8. Wake momentum deficit vs. blowing ratio (from Bons [2]).

duty cycle was chosen to be 50%. The pulsed vortex generator jets were more effective in separation control when injected at $63\%C_x$ than at $45\%C_x$. Figure 1.9 shows the wake loss coefficient with respect to blowing ratio. An improvement of greater than 50% reduction in wake loss coefficient was found at B=0.2. This was nearly the same effect as that for steady blowing but with an order of magnitude less mean mass flow. They claimed that the jet pulse influenced the boundary layer through the mechanisms of early boundary layer transition and vortical entrainment of freestream fluid. The location of the jet injection is a critical factor in determining the effectiveness of pulsed blowing.

There has been much research devoted to the flow separation over low pressure turbine blades, as reviewed in this section. These research work can be summarized as following:

1. Experimental results showed that flow separation occurs on the suction surface of the low pressure turbine blades at low Reynolds numbers, which leads to a high pressure loss.

2. The Reynolds numbers studied in these work varied from $Re_{ss} = 30,000$ to

15
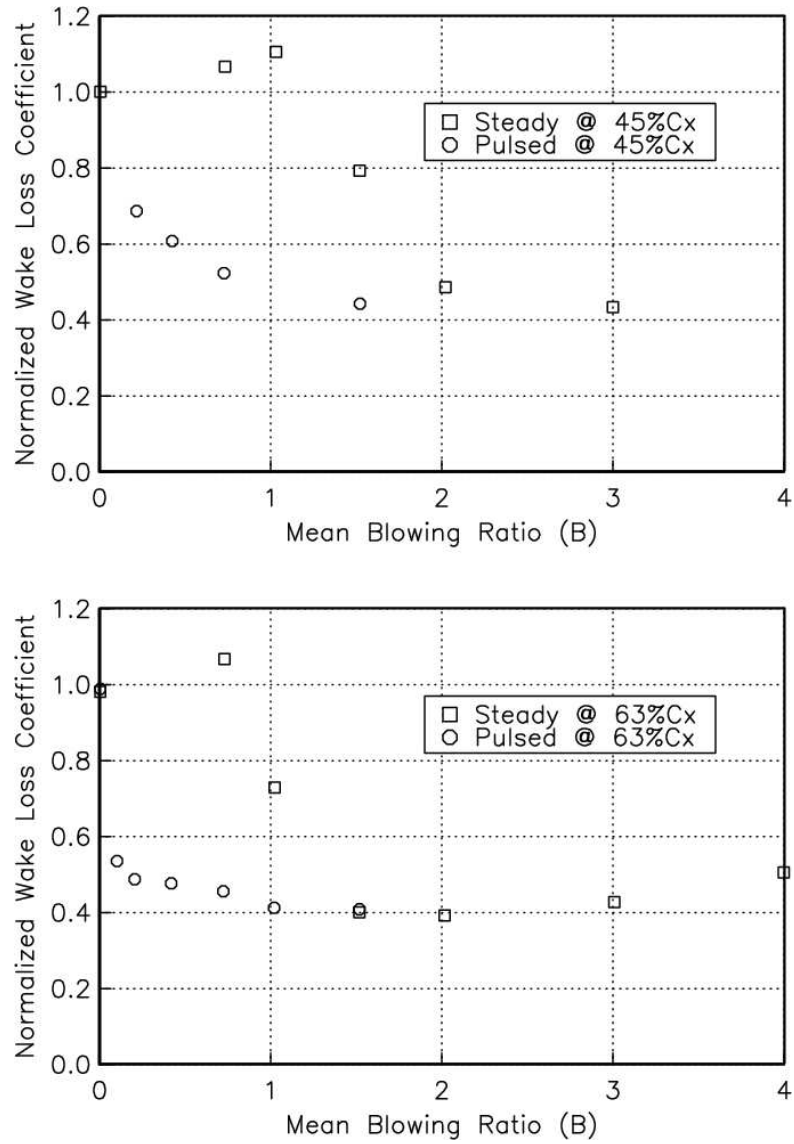
Figure 1.9. The wake loss coefficient normalized by the loss coefficient for $B=0$ versus the blowing ratio (from Bons [3]). Data for pulsed blowing at 10 Hz and 50% duty cycle versus steady blowing at $Re_c=25,000$.

16

350,000 and the freestream turbulence intensities varied from FSTI=0.5% to 10%.

3. Flow characteristics, such as the location of separation, the location of reattachment, and the transition of the boundary layer, depend on the Reynolds number and the freestream turbulence intensity.

4. There were attempts to control separation in laboratory experiments. The vortex generator jets generated streamwise vortices which mixed the high momentum and low momentum fluids together thus preventing the flow separation. The Gurney flap and the dimples worked well at low Reynolds numbers but caused parasitic drag at high Reynolds numbers.

5. There exist some numerical simulations of the flow inside low pressure turbine blade passage. But comparisons to experimental results need to be made.

1.4   Research Related to Plasma Actuators

The approach of separation control in this research work is based on the use of plasma actuators. Plasma actuators consist of two electrodes separated by a dielectric layer. One of the electrodes is exposed to the air while the other electrode is covered by the dielectric material. When a high a.c. voltage is supplied to the electrodes, the air ionizes at the edge of the electrode that is exposed to the air. The ionized air (plasma) in the presence of an electric field gradient produces a body force on the ambient air.

Plasma actuators have drawn a lot of attention and been used in many applications in recent years. Roth et al. [?] demonstrated the possibility of flow control using uniform radio frequency (RF) glow discharge surface plasma on flat panels with either streamwise or spanwise arrays of symmetric or asymmetric electrodes in a low speed wind tunnel. The symmetric streamwise electrode configurations tripped the laminar flow transition to turbulence and caused large increases in panel drag. Smoke wire flow visualization and mean velocity profiles also showed that the vortical structures were induced by the plasma. Matlis [?] used an azimuthal array of plasma actuators to excite oblique waves with a prescribed amplitude, frequency

and azimuthal wave number near the tip of a sharp cone at Mach 3.5. Corke et al. [?] used the plasma actuators as flow control devices on a NACA-0009 airfoil. By using steady plasma actuators on the upper surface of the airfoil, the lift was enhanced for a full range of angle of attack up to stall.

Based on the idea that mechanical spanwise oscillations of a wall can reduce viscous drag by up to 40%, Wilkinson [?] tried to simulate an oscillating wall by means of plasma arrays. The velocity profiles measured by the hot-wire at several streamwise locations showed that the plasma actuator generated wall jets. The plasma-induced velocity in the still air was as large as 1.6 m/s. However, the measurements of the unsteady plasma showed that the plasma-induced oscillations rolled off rapidly with frequency and were not able to meet the requirements for a low speed test. Artana et al. [?] investigated the ability of an electrohydrodynamic actuator to modify the characteristics of a flow over a flat plate. The electrodes were flush mounted on the flat plate. A high d.c. voltage ($\approx$ 30 kV) was supplied to the electrodes to generate a plasma sheet on the surface of the flat plate. The flow visualization and the PIV measurements showed that the plasma sheet induced an acceleration of the flow close to the surface.

Enloe et al. [?] conducted optical, electrical, and thrust measurements to understand the physics of plasma actuators. It was found that the plasma actuator is a form of dielectric barrier discharge. Although the plasma appears as a relatively uniform discharge to unaided eyes, there exists temporal and spatial structures in the plasma. The spatial structure showed asymmetry during one cycle of driving signal. However, this asymmetry does not control the direction of the momentum coupling. Instead, the interaction of the plasma with the applied electric field in the discharge is responsible for the body force and subsequent momentum transfer to the neutral fluid through plasma-neutral collisions.

Orlov and Corke [?] developed a model for the body force generated by the plasma actuators that can account for the space-time changes in the plasma volume. In their model, the body force per volume of plasma is given as

$$\vec{f} = \rho\vec{E} = -\left(\frac{\epsilon_0}{\lambda_D^2}\right)\phi\vec{E}, \qquad (1.2)$$

where $\vec{f}$ is the body force generated by the plasma plasma actuators, ρ is the net charge density of the plasma, ϵ_0 is the permittivity of the free space, λ_D is the Debye length, ϕ is the electric potential, and $\vec{E}$ is the electric field strength. The Debye length is the characteristic length for electrostatic shielding in a plasma. It varies with plasma density and temperature as

$$\frac{1}{\lambda_D^2} = \frac{e^2 n_0}{\epsilon_0}\left(\frac{1}{kT_i} + \frac{1}{kT_e}\right), \qquad (1.3)$$

where kT_i and kT_e are the ion and electron temperatures, n_0 is the plasma density, and e is the elementary charge.

They also modeled the plasma actuator using a network of lumped element circuit, as Enloe et al. [?] did. Figure 1.10 shows the lumped element model used by Orlov and Corke [?]. There are three capacitances in the circuit. Capacitance $C1$ represents the capacitance between the exposed electrode and the top surface of the dielectric material. Capacitance $C2$ represents the capacitance between the top surface of the dielectric and the covered electrode. Capacitance $C3$ represents the capacitance between the two physical electrodes. Using this model, it was found that the dependence of the dissipated power by plasma on the applied voltage is a power law with a coefficient of 7/2. The same dependence was observed in the experiment by Post [?] (see Figure 1.11), where the maximum induced velocity in jet generated by plasma actuator was related to the amplitude of the applied voltage as

$$U_{max} \propto V_{app}^{7/2}. \qquad (1.4)$$

19
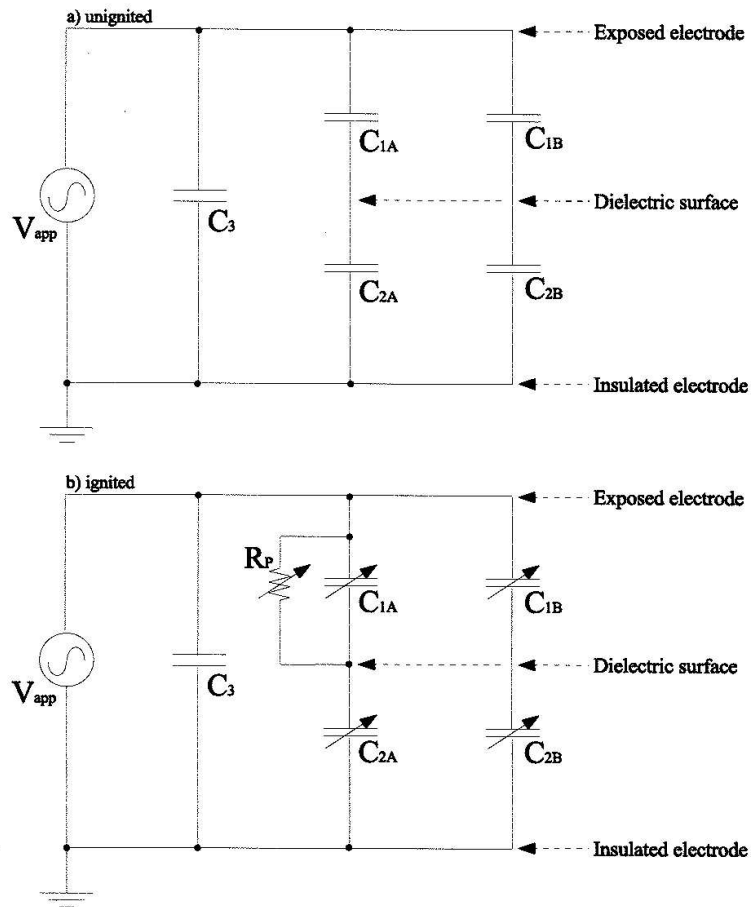
Figure 1.10. Lumped element circuit model of a single dielectric aerodynamic plasma actuator (from Orlov and Corke [19]).
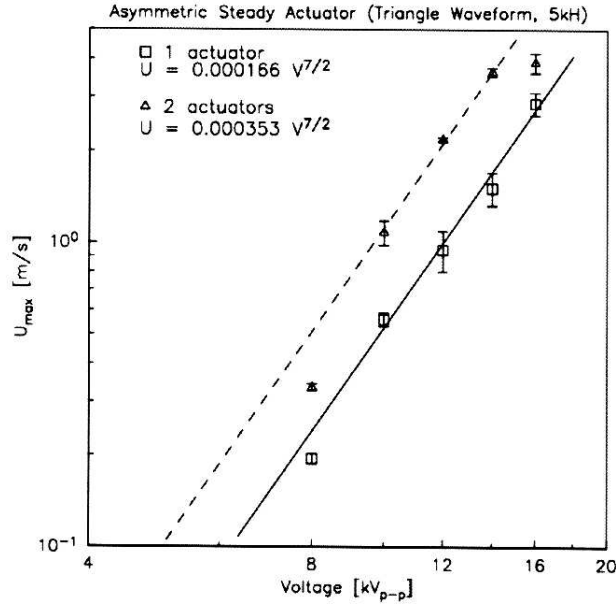
Figure 1.11. Relationship between actuator voltage and velocity output for one and two steady actuators (from Post [?]).

Corke et al. [?] used weakly-ionized plasma actuators to control the leading edge separation on a NACA-0015 airfoil. They put two spanwise plasma actuators on the suction side of the airfoil, one at the leading edge and the other one at 90% of the chord length, to simulate the leading edge and trailing edge flaps. The leading edge plasma actuator was operated in both steady and unsteady manners. The steady actuator was able to reattach the flow for angles of attack up to 19°, which was 4° past the normal stall angle. Figure 1.12 shows the measured lift coefficient versus angle of attack for the airfoil with the leading edge plasma actuator off and on in steady operation. The lift forces were measured by a force balance. The curves correspond to numerical simulations using a modified version of CFL3D [?]. The unsteady actuator was found to work even better, which was able to reattach the flow up to 9° past the normal stall angle. The trailing edge actuator was operated in a steady manner. When it was operated, it produced the same effect as a plane
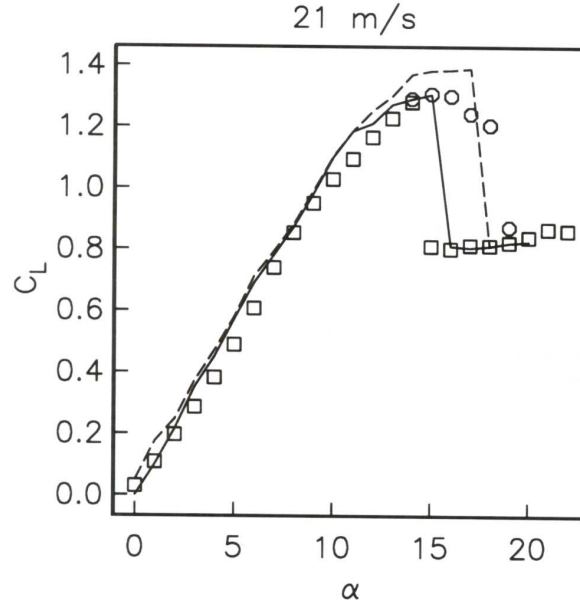
Figure 1.12. Lift coefficient versus angle of attack for NACA-0015 airfoil with leading edge actuator off and on in steady operation (from Corke [?]).

trailing edge flap. This included a uniform shift at all angles of attack of the lift coefficient, and a shift toward higher C_L of the drag bucket. They also study the effect of the excitation frequency of the leading edge actuator on the separation control. It was found that an optimum excitation frequency was corresponded to $S_t = fc/U_\infty = 1$, as shown in Figure 1.13.

Post and Corke [?] successfully demonstrated the leading-edge separation control on high angle of attack airfoil using plasma actuators. Two plasma actuators were employed and the plasma actuators were oriented to produce steady two-dimensional wall jets in the flow direction. It was found that the reattached flow induced by the actuator led to a significant suction-pressure recovery and drag reduction that yielded as much as a 400% increase in the L/D ratio.

Plasma actuators for leading edge separation control of the dynamic stall vortex on an oscillating NACA-0015 airfoil were investigated by Post [?]. Flow visualization
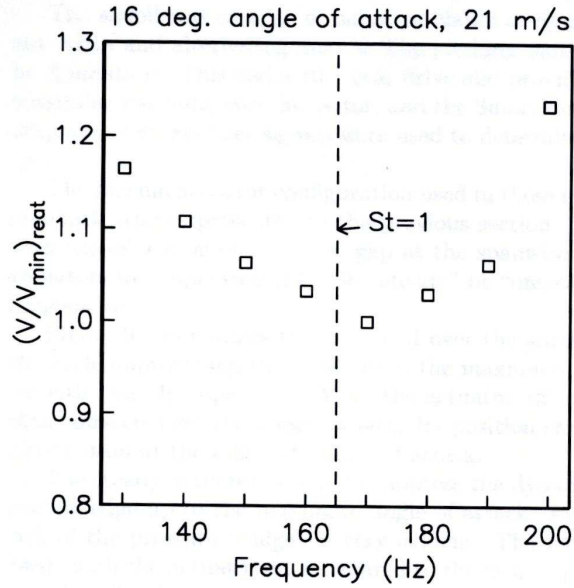
Figure 1.13. Minimum voltage required to reattach the flow as a function of the actuator frequency for unsteady operation (from Corke [?]).

and pressure measurements were conducted to investigate the effectiveness of the plasma actuators. The airfoil could be oscillated about its quarter chord location with any mean and alternating angles. The effectiveness of both steady and unsteady plasma actuators were examined. Figure 1.14 shows both the flow field over the suction surface of the oscillating airfoil and the surface pressure distribution for the cases with the actuator off and on in steady operation. The angle of attack cycle was given by $\alpha(t) = 15° + 10° sin(\omega t)$, with a reduced frequency of $k = 0.08$. It can be seen that, with the plasma actuator off, the dynamic stall vortex forms at the leading edge and convects downstream. Its position can be tracked by the location of the "bulge" in the C_p distribution at different angles of attack. The steady plasma actuator was able to suppress the dynamic stall vortex. At the maximum angle of attack, $\alpha = 25°$, the complete lack of the pressure "bulge" is evident.

23
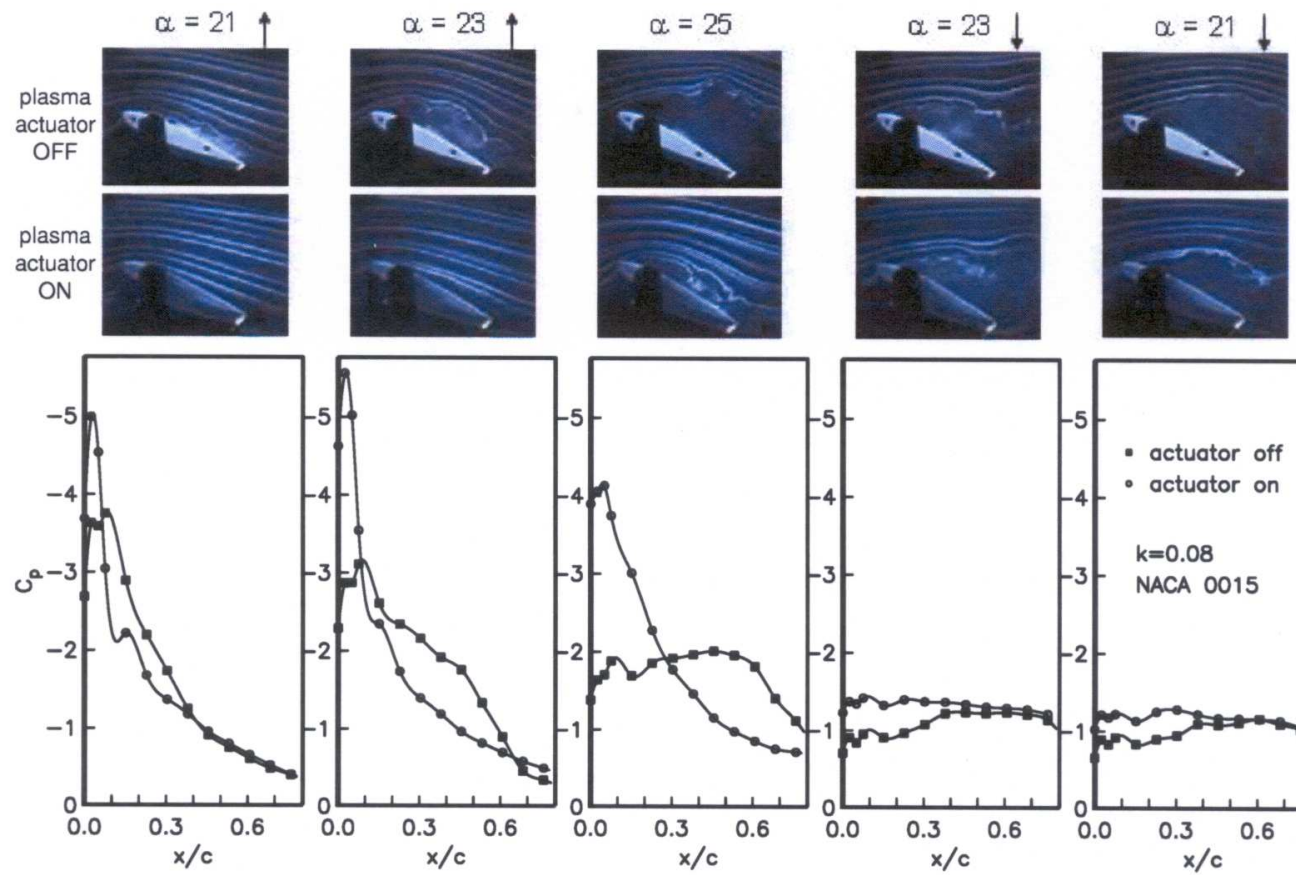
Figure 1.14. Flow visualization and pressure coefficient distributions for angles of attack near and at the peak of the oscillatory cycle (from Post [?]).

For the unsteady plasma actuators, the actuation frequency (80 Hz) that makes the Strouhal number unity did not work as well as a lower frequency (20 Hz). The rational for the 20 Hz excitation is that this frequency would excite approximately two vortices for each half cycle of the pitching motion. With the 20 Hz excitation, the lift was improved by 10%.

A review of plasma actuators was presented by Corke and Post [?]. It can be seen that the plasma actuator is a very promising active control method. It has many advantages. For example, it does not consume much energy. The typical power consumption of a plasma actuator is $2 \sim 50$ W for 12 inch span [?]. Another advantage of plasma actuators is that it can be built flush to the blade surface. Therefore it will not cause parasitic drag when not operated.

1.5   Objectives

The experimental and numerical work have shown that the flow separation occurs on the suction side of the low pressure turbine (LPT) blades at low Reynolds numbers. Some work have been done to control the flow separation using vortex generator jets. Although encouraging results have been obtained using this control method, it has its disadvantages. The approach of separation control in this research work is based on the use of plasma actuators. The objectives of this research work are:

1. To document the pressure distributions and the velocity profiles around a generic LPT made up of a linear cascade of "PakB" blades. The solidity of the cascade is 1.13, which is the same as that used by Bons [2].

2. To study the effects of Reynolds number and turbulence intensity on the separation and reattachment locations on the blade. This is done with surface pressure measurements and velocity profiles measurements using Laser Doppler Velocimetry (LDV).

3. To demonstrate the ability of steady and unsteady plasma actuators to control the flow separation on the "PakB" blades. This is done with pressure measurements and LDV measurements.

4. To optimize the configuration of steady plasma actuators to get the most effective separation control. This includes the location of the plasma actuator, the number of the plasma actuators, the orientation of the electrodes, and the plasma voltage amplitude.

5. To understand the mechanism of steady and unsteady plasma actuators. This is done using flow visualization and power spectrum measurements of velocity fluctuations in the flow over the "PakB" blade.

CHAPTER 2

EXPERIMENTAL SETUP AND CONDITIONS

2.1   Wind Tunnel

A specially designed wind tunnel was built for this research work. Figure 2.1 shows a schematic of the tunnel. The wind tunnel is an open-loop type. The air is drawn into the wind tunnel through a section consisting of a four-inch-thick honeycomb and five low-solidity screens. The air then passes through a 6:1 area ratio contraction section. The contraction shape is a fifth order polynomial. The combination of honeycomb, screens and contraction gives a freestream turbulence intensity at the exit of contraction of $u'/U_\infty = 0.08\%$.

A straight section following the contraction gives access to placing turbulence generating devices upstream of the linear cascade, which is hosted in a turning section. The inlet to the cascade has a 36.5 in (92.71 cm) square cross section dimension. The turning angle of the cascade section is 95°. Two "tail boards" were attached to the trailing edge of the most outboard and inboard blades to aid the flow in negotiating the turn, and to maintain the correct pressure gradient on the blade. The angles of the tail boards were adjusted so that at high chord Reynolds numbers, the pressure distribution on the blades agreed with inviscid (Euler) calculation [23].

The top wall of the cascade section is made of lexan and side walls are made of plexiglas to give optical access to LDV measurements and flow visualization.

Following the cascade section is a straight section and a diffusion section. The

27
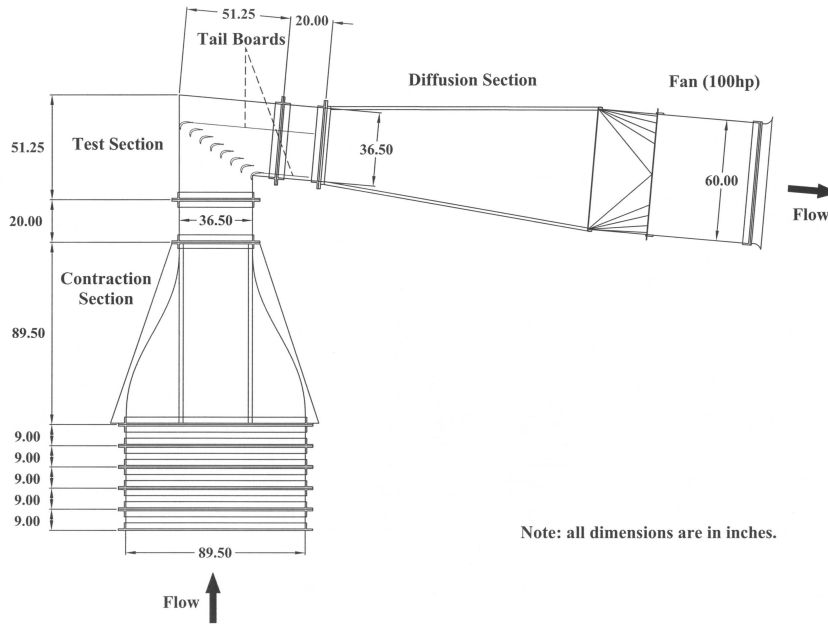
Figure 2.1. Schematic of the wind tunnel.

fan is located downstream of a square-to-circular transition section which matches up with the outlet of the diffusion section. The fan is five feet in diameter with manual variable pitch. It is powered by a 100 hp motor. At the maximum rpm, the fan will deliver $79,000$ cfm. For the current blade design, this will give a range of chord Reynolds numbers of $0 \leqslant Re_c \leqslant 650,000$. A photograph of the wind tunnel is shown in Figure 2.2.

2.2   Linear Cascade

The linear cascade hosted in the test section consists of nine blades. These blades bear the "PakB" shape, which was designed for a typical low pressure turbine by Pratt & Whitney Company. Figure 2.3 shows a single "PakB" blade.

The "PakB" blades were molded using urethane. Figure 2.4 shows the steel mold used to fabricate the blades. The blade chord length is $C = 7.0$ in (17.78 cm).

28

Figure 2.2. An open-loop wind tunnel was used in this work.
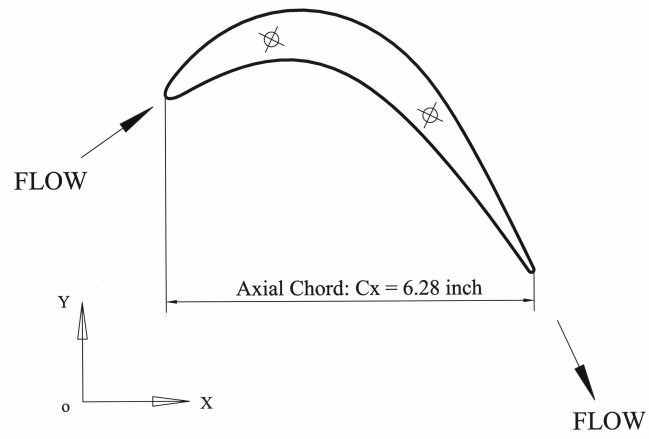
Figure 2.3. The "PakB" blade has an axial chord length of 6.28 in (15.95 cm).

However, in order to be consistent with Bons [2], the axial chord length is used throughout this dissertation. Since the stagger angle of the blade is $\gamma = 26°$, the axial chord length of the blades is $C_x = Ccos\gamma = 6.28$ in (15.95 cm). The spacing between every two blades is $S = 5.56$ in (14.12 cm). This gives a solidity of $C_x/S = 1.13$. The linear cascade has an inlet angle of 55° and a design exit angle of 30°, as shown in Figure 2.5. A photograph of the "PakB" cascade is also shown in Figure 2.6.
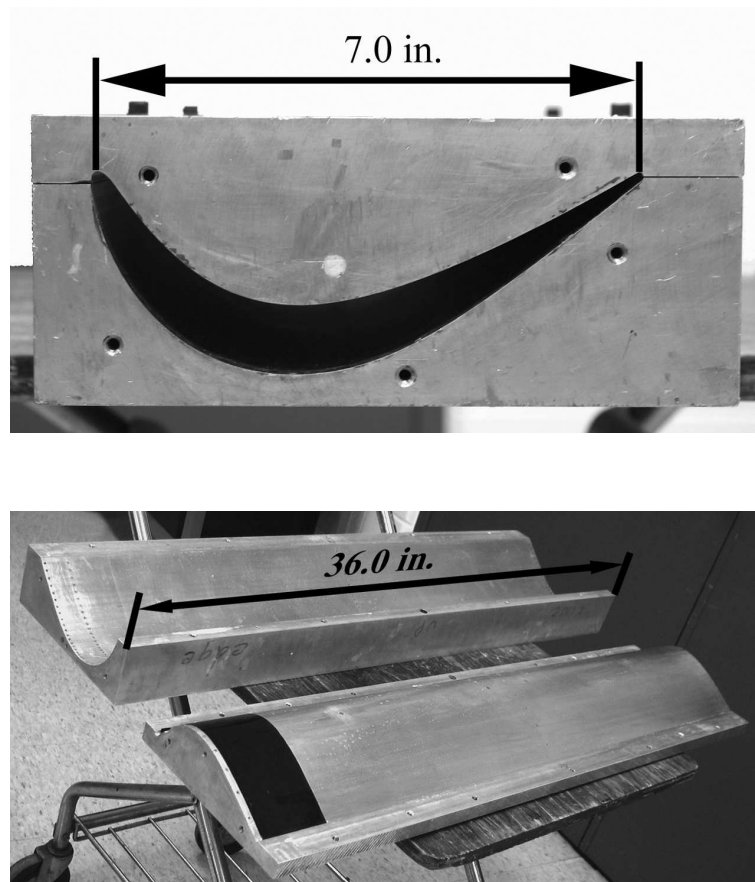
Figure 2.4. A CNC-machined aluminum mold was used to fabricate "PakB" blades (top: side view, bottom: top view).
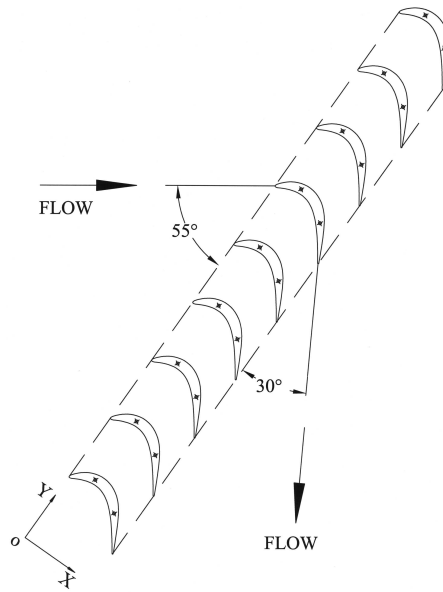
Figure 2.5. The linear cascade consists of nine "PakB" blades.
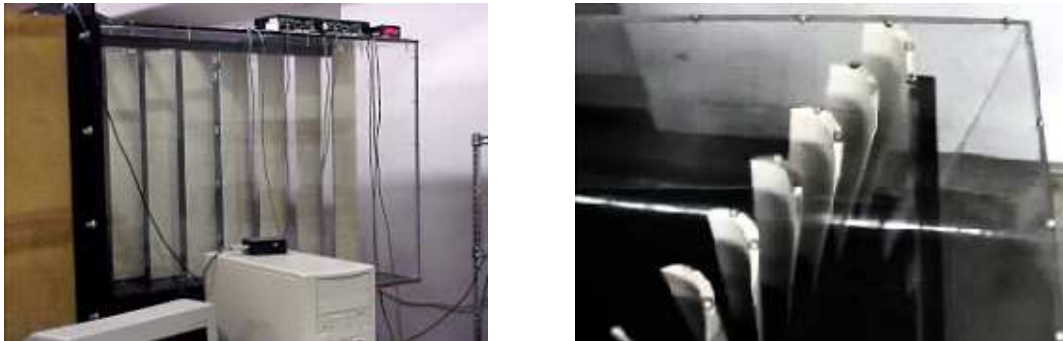
Figure 2.6. The "PakB" cascade is hosted in the turning section of the wind tunnel (left: side view, right: top view).

2.3 Turbulence Generators

The turbulence intensity is an important parameter in this research work. The turbulence intensity in the freestream of the wind tunnel is 0.08%. To obtain a range of higher turbulence intensities several turbulence generators were designed and two were used in this experiment. The one labeled "Grid 3" was a perforated plate with 0.25 in (6.35 mm) diameter holes, a mesh size of 0.313 in (7.95 mm), and a solidity of 0.42. The grid was held in a frame which fit within the straight section upstream of the "PakB" cascade. The position of the frame could be moved to place the grid at different streamwise distances from the cascade. This distance is referenced to the leading edge of the center blade.

The other turbulence generator, labeled "Grid 0", was a mesh of 0.1875 in (4.76 mm) diameter cylinders. The mesh size (centerline spacing) in this grid was 1.0 in (2.54 cm). This was also held in a frame which fit in the section upstream of the cascade. Figure 2.7 shows a photograph of these two turbulence generators.
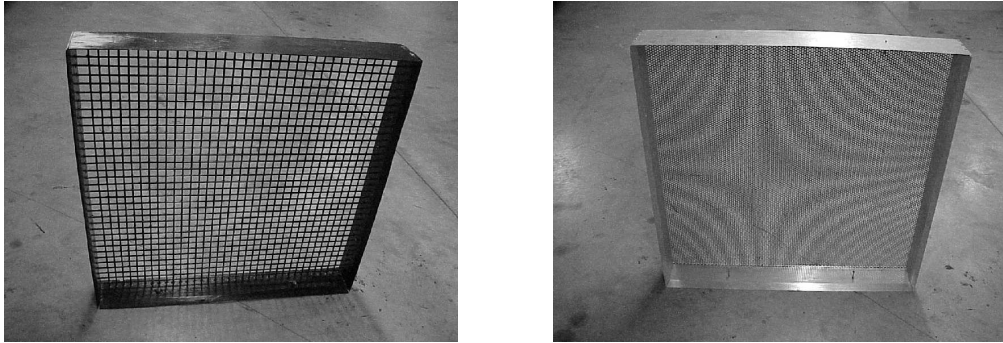
Figure 2.7. The turbulence generators (left: Grid 0, right: Grid 3).

The turbulence intensities of all three velocity components were measured at different distance downstream of the two grids using an "X" wire. The "X" wire is able to measure either (u, v) or (u, w) simultaneously. Figure 2.9 and Figure 2.8

show the turbulence intensity, u'/U_∞, and the local ratios v'/u' and w'/u' for Grid 3 and Grid 0, respectively. These ratios are intended to show the degree of isotropy, which would be perfect if both ratios were 1. In reality, having $v'/u' \approx w'/u'$ and $\geqslant 0.9$, is considered quite satisfactory as an indication of isotropic nature of the turbulence scales.
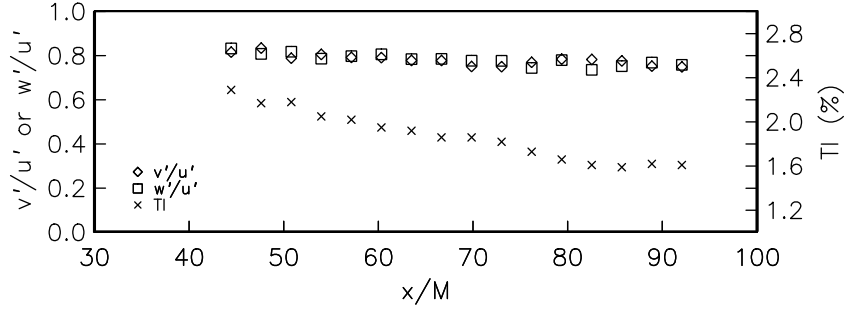
Figure 2.8. Turbulence intensity (TI) and isotropy (v'/u' and w'/u') as a function of streamwise distance for Grid 3.

With Grid 3, in Figure 2.8, the turbulence intensity varied from approximately 2.4% to 1.6%. The ratios of the fluctuating components was approximately 0.8 throughout the range of distances from the grid, with the energy evenly distributed among the three fluctuating velocity components. The condition that I chose to use for this grid occurred by placing it the furthest distance from the center blade. This gave a freestream turbulence intensity of $u'/U_\infty = 1.6\%$. This trubulence intensity was 20 times higher than the freestream turbulence intensity without the grid.

With Grid 0, shown in Figure 2.9, the turbulence intensity varied from approximately 5.1% to 2.85%. The ratios of the fluctuating components were somewhat better than with Grid 3, having values of approximately 0.9 throughout the range of distances from the grid. Again, the energy was evenly distributed among the three fluctuating velocity components. The condition that I chose to use for this grid occurred by placing it the furthest distance from the center blade. This gave

33
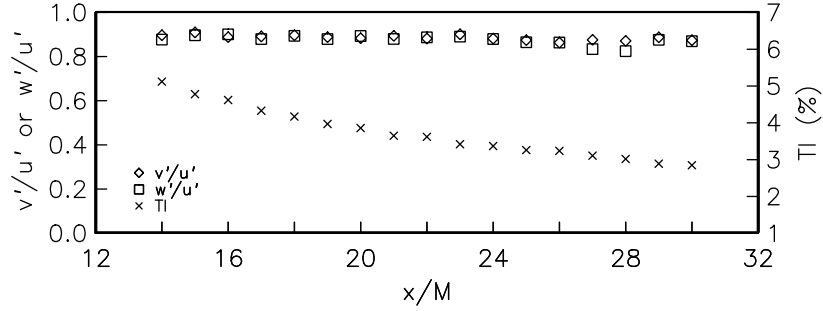
Figure 2.9. Turbulence intensity (TI) and isotropy (v'/u' and w'/u') as a function of streamwise distance for Grid 0.

a freestream turbulence intensity of $u'/U_\infty = 2.85\%$. This turbulence intensity was 36 times larger than the freestream turbulence intensity without the grid, and 1.78 times that of Grid 3.

2.4 Pressure Measurements

2.4.1 Pressure Taps

The center blade of the cascade is instrumented around both suction and pressure surfaces with 40 static pressure taps to allow measurements of the blade pressure distributions. The chordwise locations of the taps are listed in Table 2.1 and Table 2.2.

A majority of the taps are on the suction side of the blade, with a special concentration in the region of $0.5 \leqslant x/C_x \leqslant 1.0$, where the flow is expected to separate at low Reynolds numbers. The pressure taps are located at the half-span location of the blade and are distributed in the chordwise direction. A smaller number of taps were located at other spanwise positions and were only used early in the study to confirm the two-dimensionality of the blade pressure distribution. The surface pressure is transmitted through 0.050 in (1.27 mm) diameter tubulations that are molded inside the blade, and exit through the bottom end.

34

TABLE 2.1

THE LOCATIONS OF THE PRESSURE TAPS (SUCTION SURFACE)

Tap no.	1	2	3	4	5	6	7	8	9	10
$x/C_x(\%)$	1.0	5.0	10.0	15.0	20.0	25.0	30.0	35.0	40.0	45.0
$s/L_{ss}(\%)$	3.11	8.47	14.07	18.73	22.81	26.48	29.92	33.19	36.59	40.02
Tap no.	11	12	13	14	15	16	17	18	19	20
$x/C_x(\%)$	50.0	52.5	55.0	57.5	60.0	62.5	65.0	67.5	70.0	72.5
$s/L_{ss}(\%)$	43.64	45.69	47.89	49.74	52.13	54.63	56.68	59.40	62.26	65.27
Tap no.	21	22	23	24	25	26	27	28	29	30
$x/C_x(\%)$	75.0	77.5	80.0	82.5	85.0	87.5	90.0	92.5	95.0	97.5
$s/L_{ss}(\%)$	68.43	71.74	75.18	78.74	82.29	86.00	89.50	92.86	96.04	99.24

TABLE 2.2

THE LOCATIONS OF THE PRESSURE TAPS (PRESSURE SURFACE)

Tap no.	1'	2'	3'	4'	5'	6'	7'	8'	9'	10'
$x/C_x(\%)$	1.0	11.0	21.0	31.0	41.0	51.0	61.0	71.0	81.0	91.0

2.4.2 Scanivalve and Pressure Transducer

The tubulations connected to a JS4-48 scanivalve which selectively connected each port to a single differential pressure transducer. There are totally 48 ports on the scanivalve among which 41 were used (40 for the pressure ports on the blade and 1 for the total pressure coming from the freestream pitot tube). The scanivalve was controlled by a CTLR2/S2-S6 solenoid stepper driver.

A DP103 differential pressure transducer made by Validyne Corporation and a companion carrier demodulator (CD23) were used to convert the differential pressure into voltage. The diaphragm for DP103 is interchangeable. In this research work, a No. 22 diaphragm was used, which can measure pressure up to 2.22 inH$_2$O.

2.4.3 Pressure Measurements Method

Figure 2.10 shows a flow chart of pressure measurements. Pressure data acquisition were automated and executed using a C program running on a personal computer. The sampling frequency for pressure measurements was 1000 Hz. In order to filter out the effect of unsteadiness, the convergency of data was checked during acquisition. The scanivalve was stepped to the next pressure port only after the mean values converged to a pre-defined value ϵ. The pressure data were written to a file at the end of acquisition and the pressure coefficients were calculated from them.

2.5 Laser Doppler Velocimetry (LDV) Measurements

To document the flow field, boundary layer profiles around "PakB" blades were measured using both Laser Doppler Velocimetry (LDV) and hot-wire anemometry. An Aerometric fiber optic LDV system was operating in one-component back-scatter mode to measure the streamwise velocity u. Frequency shifting was used in order to
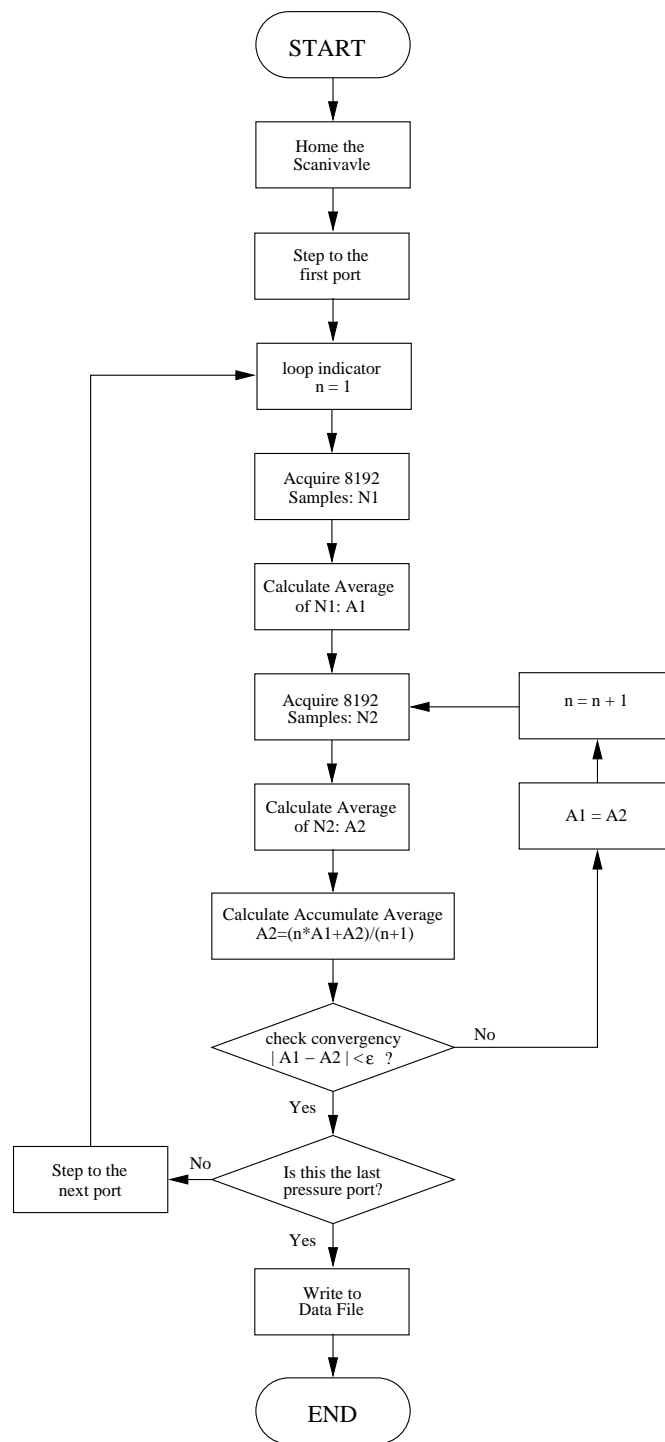
Figure 2.10. The flow chart of pressure measurements.

unambiguously resolve the flow direction. The transceiver of the LDV system was mounted on a computer controlled traverse table, as illustrated in Figure 2.11. The accuracy of the movement of the traverse table was 0.4 μm. The width and height of the measurement probe volume of the LDV system were 234.4 μm and 234.0 μm, respectively. Wind tunnel seeding was performed at the tunnel inlet with a TSI droplet generator (model 9307) using olive oil. The particle size is around 1 μm.
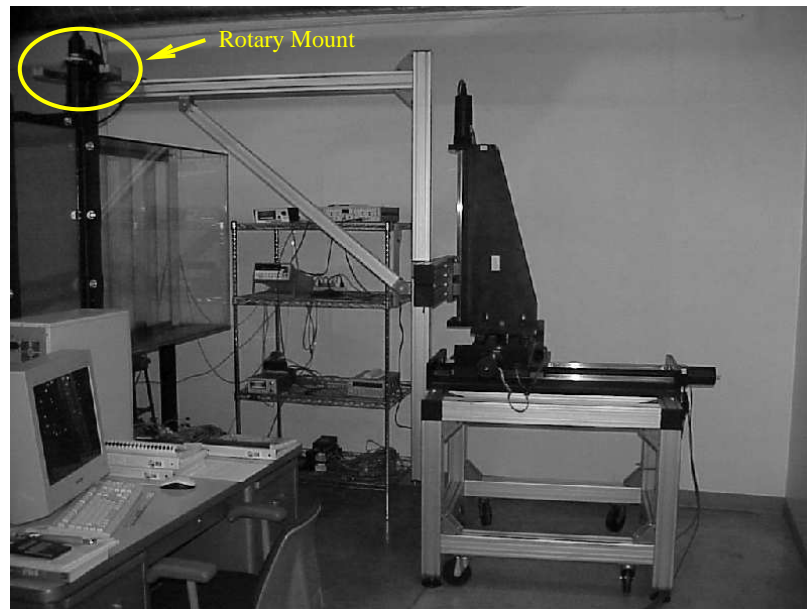
Figure 2.11. The transceiver of the LDV system is mounted on a computer controlled traverse table using a specially designed rotary mount shown at the top of the boom arm in the upper left of the photograph.

The top wall of the cascade section of the wind tunnel is made of Lexan to make the flow field accessible for the LDV measurements. However, I found that Lexan has such poor optical properties that it significantly disperses the energy of laser beams as they pass through it. This caused an extremely low data rate. To solve this problem, a rectangular window was cut into Lexan and covered with a piece of regular glass of the same size as the window (see Figure 2.12).
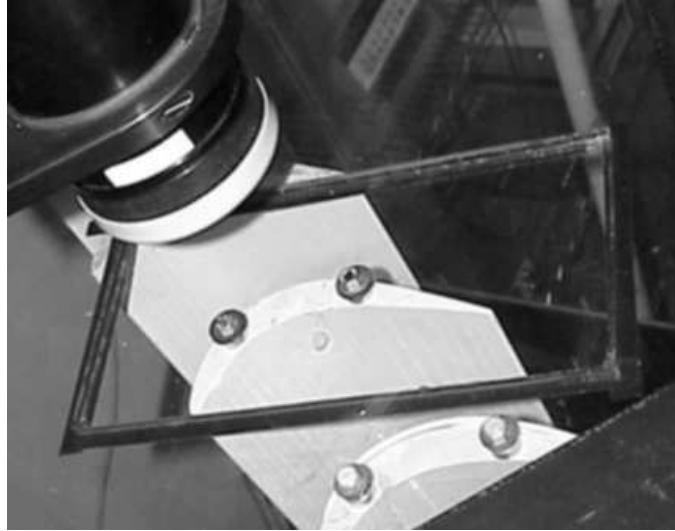
Figure 2.12. A rectangular window was cut into Lexan ceiling and replaced with a piece of $\frac{1}{8}$" thick regular glass to give better optical access for LDV system.

A specially designed rotary mount was used to mount the transceiver on the triangular traverse beam so that the transceiver could be rotated in order to align the probe volume parallel to the local blade surface. There were marks on the rotary mount. Combining these marks and a needle pointer attached to the transceiver indicated the rotation angle. Figure 2.13 shows a schematic of the rotary mount and Figure 2.14 is a photograph showing how the transceiver was mounted to the traverse beam through the rotary mount.

The boundary layer profiles were measured at seven different streamwise locations using LDV technique. For each streamwise location, the probe volume was adjusted parallel to the local blade surface using the rotary mount shown in Figure 2.13. The rotation angles of the transceiver with respect to the inlet flow are shown in Table 2.3.

The LDV measurements were conducted at seven different streamwise locations (see Table 2.4). The computer controlled traverse table moved the probe volume
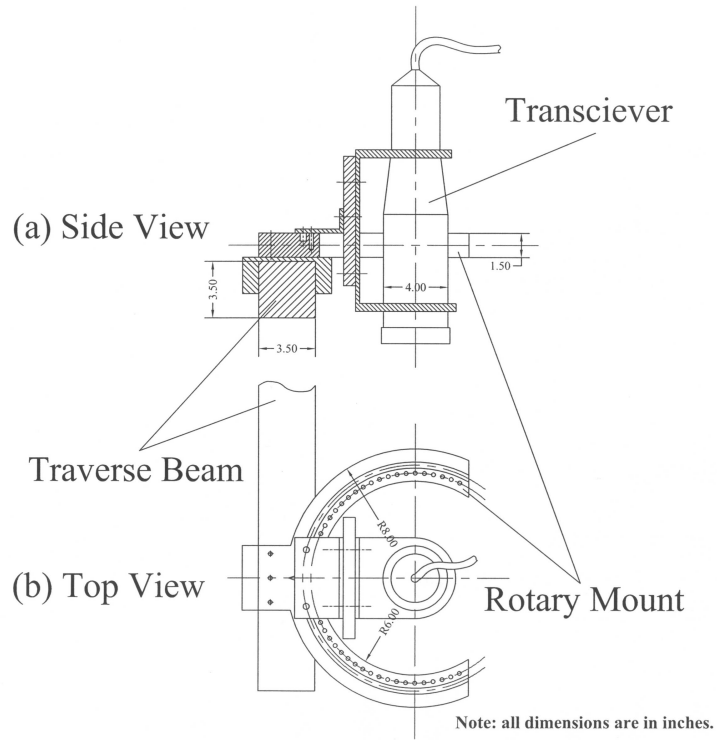
Figure 2.13. Schematic of the rotary mount for LDV measurements.
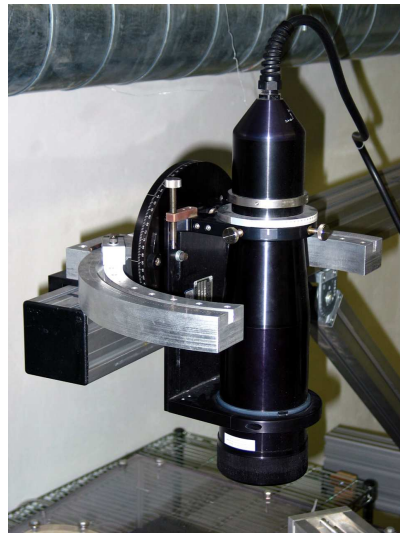
Figure 2.14. A specially designed rotary mount was used to mount the transceiver on the triangular traverse beam.

TABLE 2.3

THE ROTATION ANGLE OF TRANSCEIVER WITH RESPECT TO THE
INLET FLOW

Location No.	1	2	3	4	5	6	7
$x/C_x(\%)$	50.0	60.0	70.0	75.0	80.0	85.0	90.0
Rotation Angle ($^\circ$)	52.97	70.17	84.32	90.90	94.68	96.73	98.25

away from the "PakB" blade in a local wall normal direction. The boundary layer on
the suction side was found to be less than 1.5 mm thick before the separation point at
Reynolds number of $50,000$. Therefore a smaller spatial resolution of 0.05 mm was
used within 2 mm wall normal distance while a larger spatial resolution of 0.1 mm
was used outside this region. A complete traversing coordinates can be found in
Appendix B. For every spatial location, more than $10,000$ valid data bursts were
obtained and an ensemble average was taken to obtain the local streamwise velocity.

TABLE 2.4

THE STREAMWISE LOCATIONS FOR LDV MEASUREMENTS.

No.	1	2	3	4	5	6	7
$x/C_x(\%)$	50	60	70	75	80	85	90

2.6   Hot-Wire Measurements

In this research work, a single tungsten hot-wire of 0.00015 in (0.00381 mm)
diameter was used for the blade velocity profile and the power spectrum measure-
ments. The hot-wire probe was attached to a mini-traverse system, which was

mounted inside the test section downstream the "PakB" cascade. Figure 2.15 shows a schematic of the mini-traverse system. A MicroMo Inc. stepper motor was used to drive a linear rail which held the hot-wire probe. The linear rail was aligned perpendicular to the local blade surface. The accuracy of the mini-traverse system is 50 μm. Figure 2.16 shows a photograph of the mini-traverse system with mounted hot-wire probe.
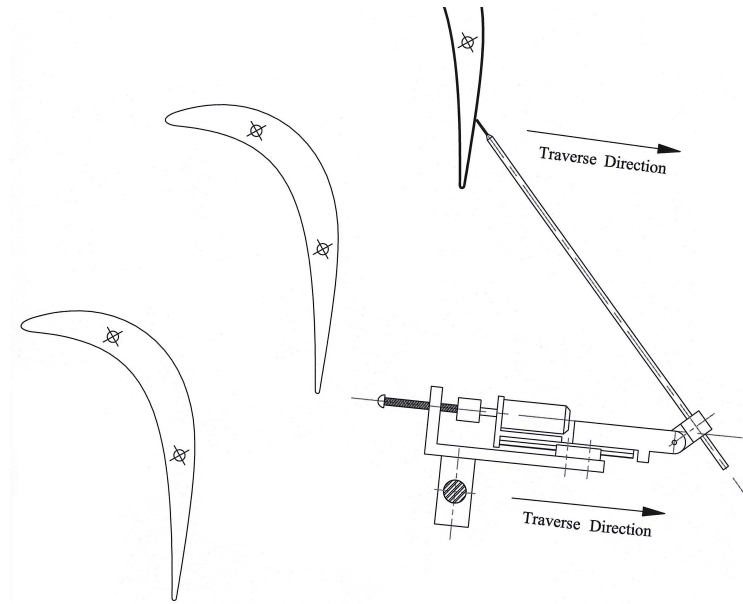
Figure 2.15. The schematics of the mini-traverse system for hot-wire measurements.

The output signal from the hot-wire anemometer was introduced into a low-pass filter which was set with a cutoff of 5000 Hz. The signal was then sent into a PC and acquired through a PowerDAQ A/D board. The sampling frequency was chosen to be 10000 Hz.

When plasma actuators were not operated, a TSI IFA-100 constant-temperature anemometer (CTA) was used to analyze the hot-wire signals. However, when plasma actuators were operated, special attention must be paid when choosing hot-wire anemometers. In normal anemometer designs, one support of the hot-wire is

Figure 2.16. The hot-wire probe was mounted on a mini-traverse system which was aligned perpendicular to the local blade surface.

grounded. If plasma actuators are allowed to charge the ungrounded support, ultimately sufficient voltage will be generated and burn out the wire. The solution to this problem was to allow both supports to float above instrument grounds. This would provide protection to the hot-wire by maintaining a small differential voltage across the wire that was set by the overheat control regardless of the plasma effects.

Figure 2.17 shows a diagram of a specially designed constant-current anemometer (CCA) that was used in this research work when plasma actuators were operated. A transformer of wiring-ratio of 1:31 was used to transfer the a.c. component of the hot-wire signal, thus separated the hot-wire ground and instrument ground. Refer to Matlis [?] for further information about this constant-current anemometer.

The hot-wire measurements were conducted at six different streamwise locations (see Table 2.5). For every streamwise location, the hot-wire probe was traversed outward from the blade surface to the local freestream to cover the whole range

overheat voltage control

opto–isolator (GE4N36)

2x1.5V

D–Cell

100 Ω

100 Ω

Hot–Wire

2M Ω

Transformer
1:31

1.8k Ω

1.8k Ω

21k Ω

21k Ω

CA3140

1

Floating Ground CCA

147k Ω

10k Ω

0.001µF

CA3140

1.5k Ω

1.5k Ω

0.001µF

CA3140

0.001µF

1.5k Ω

1.5k Ω

0.001µF

CA3140

0.001µF

ac output

Frequency Compensation

Fourth–Order Low–Pass Filter
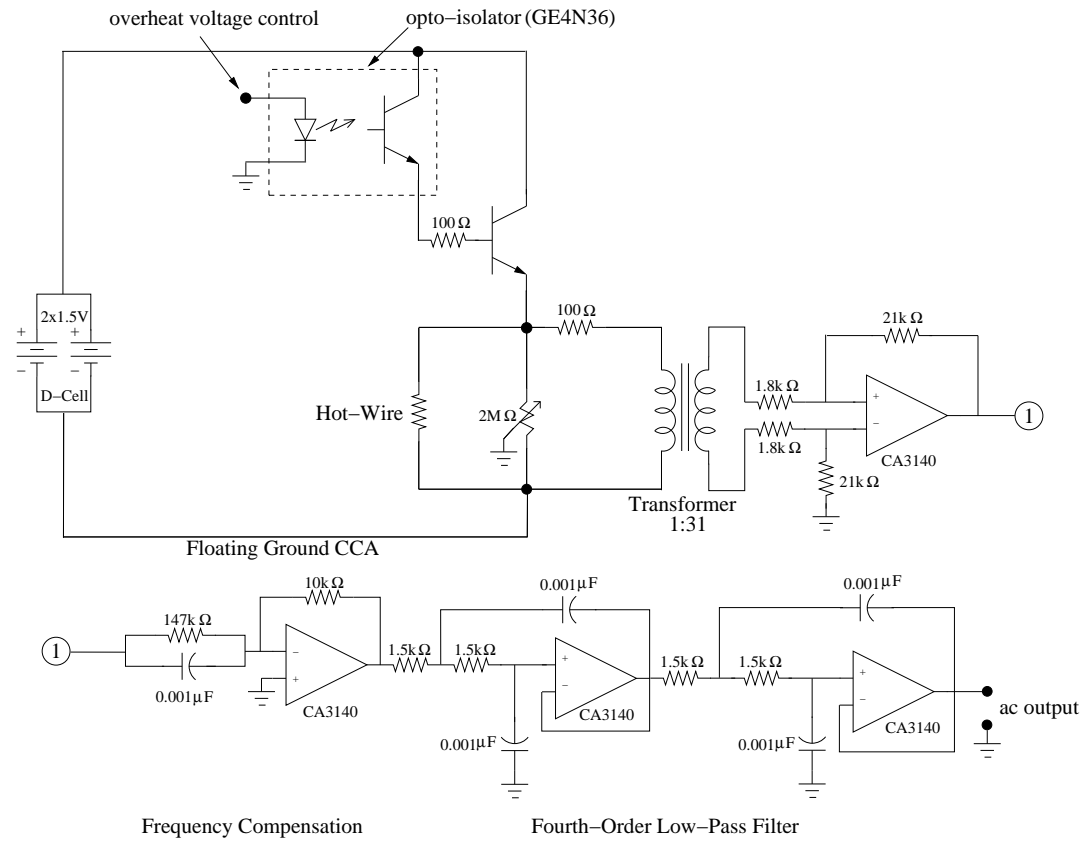
Figure 2.17. A constant-current anemometer was specially designed to analyze the hot-wire signal when plasma actuators were operated.

of the boundary layer. A total of 131072 samples were obtained for every spatial point. The mean velocity, rms velocity, and power spectrum were calculated from these samples.

TABLE 2.5

THE STREAMWISE LOCATIONS FOR HOT-WIRE MEASUREMENTS.

No.	1	2	3	4	5	6
$x/C_x(\%)$	60	70	75	80	85	90

2.7   Plasma Actuators

The approach for separation control on the "PakB" blades in this research work is based on the use of plasma actuators. A plasma actuator consists of two electrodes which are separated by a dielectric layer. A high voltage a.c. input is supplied to the electrodes. When the a.c. amplitude is large enough, the air ionizes in the region of the largest electric potential. This is generally at the edge of the electrode which is exposed to the air. The ionized air, in the presence of an electric field gradient, produces a body force on the ambient air. The body force per volume plasma is a vector given as [?]

$$\vec{f} = \rho\vec{E} = -\left(\frac{\epsilon_0}{\lambda_D^2}\right)\phi\vec{E}, \tag{2.1}$$

where $\vec{f}$ is the electrohydrodynamic (EHD) body force induced by the plasma, ρ is the net charge density of the plasma, ϵ_0 is the permittivity of the free space, λ_D is the Debye length, ϕ is the electric potential, and $\vec{E}$ is the electric field strength.

In this work, copper tapes were used to make actuator electrodes. The nominal thickness of copper tape is 0.025 mm (1 mil). For the dielectric layer, two different materials were used in this research: kapton and macor. Kapton is known for its

unique combination of physical, electrical, and mechanical properties. It has high dielectric strength (typical value: 200 kV/mm) and low dielectric constant (typical value: 3.0). However, it degrades during the usage of actuator and finally fails. Macor is machinable glass ceramic. Compared to kapton, macor has lower dielectric strength (typical value: 40 kV/mm) and higher dielectric constant (typical value: 6.0). Unlike kapton, macor is very robust and will never fail for my operating conditions. Figure 2.18 shows how these two different materials were used in a plasma actuator. The thickness of single layer of the kapton film is 0.125 mm (5 mil). The lower electrode, the kapton film, and the upper electrode are taped on the "PakB" blade in a "sandwich" structure. Since two layers of kapton film were used, the total thickness of the the actuator is about 0.3 mm. As to the macor, it is extremely difficult to make a very thin layer out of it to match the shape of "PakB" blade despite it is machinable. Thus a new method was used to make a macor-based actuator. A new "PakB" blade was molded with a recess in the middle part. The lower electrode and the macor were embedded in the blade. The upper surface of the macor was machined and carefully sanded to match the "PakB" shape so that the it is flush to the blade surface. The upper electrode was then glued to the macor. The maximum thickness of the macor is about 0.375 in (9.525 mm). Since the macor is much thicker than the kapton film, higher voltage is required to generate plasma on a macor-based actuator. Figure 2.19 shows photographs of both kapton-based and macor-based actuators when they are applied to "PakB" blades.

The body force vector can be tailored through the design of the electrode arrangement, which controls the spatial electric field. Post [21] demonstrated arrangements that could produce wall jets, spanwise vortices, and streamwise vortices, when placed on the wall in a boundary layer. The body force representation is also a convenient form to incorporate the effect of the actuators in Navier-Stokes simulations of the
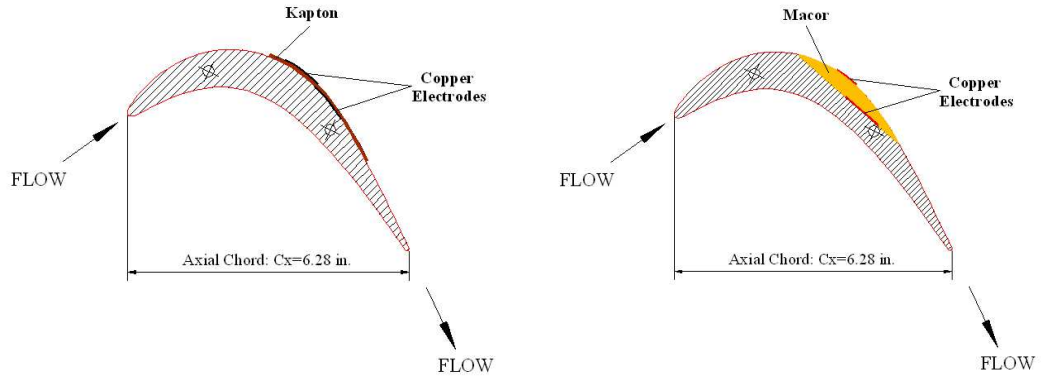
Figure 2.18. Two different materials were used as the dielectric layer when making plasma actuators (left: kapton, right: macor).
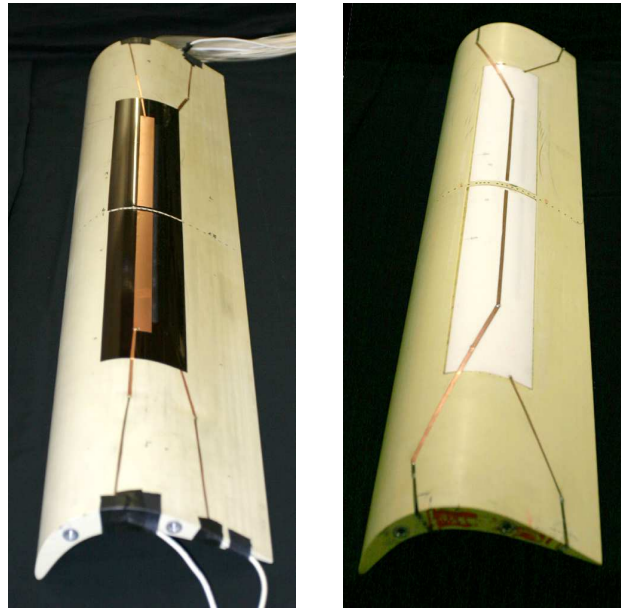
Figure 2.19. Pictures of plasma actuators when they are applied to "PakB" blades (left: kapton-based actuator, right: macor-based actuator).

47

flow field [19][20]. Such simulations are useful in designing and optimizing actuator arrangements.

2.7.1 Generation of Plasma

In this research work, the high a.c. voltage required to generate plasma was produced using specially designed circuits. Figure 2.20 shows a block diagram of the circuits. A Standford Research System function generator produces a high-frequency, low-amplitude triangular wave. The frequency is of order 5 kHz. The triangular wave then goes into a signal control circuit. This circuit consists of several sub-circuits used to control the amplitude, phase, and, in case of unsteady pulsing, the frequency and the duty cycle of the signal. The fine-tuned signal coming out the the control circuit is amplified twice through a two-stage amplifier before it is sent to the plasma actuators. The amplitude of the signal that reaches plasma actuators is of order 10 kV.

2.7.2 Unsteady Pulsing

Both steady and unsteady plasma actuators were examined in this research work. For steady actuation, a high a.c. voltage was continuously applied to the plasma actuators so that the plasma was always present on the surface of "PakB" blades during flow control. For unsteady actuation, a method is needed to switch on and off plasma at desired frequencies. This was achieved using a circuit based on a precision timer LM322N and a quad bilateral switch CD4066, as shown in Figure 2.21.

The input to LM322N (input1) is regular rectangular wave generated by a function generator. The frequency of this rectangular wave is set at the desired excitation frequency. The change of duty cycle can be achieved by adjusting the potentiometer R_t connected to LM322N. The output from LM322N (output1) is introduced into CD4066 as a control signal. Combining this control signal with a triangular wave

48
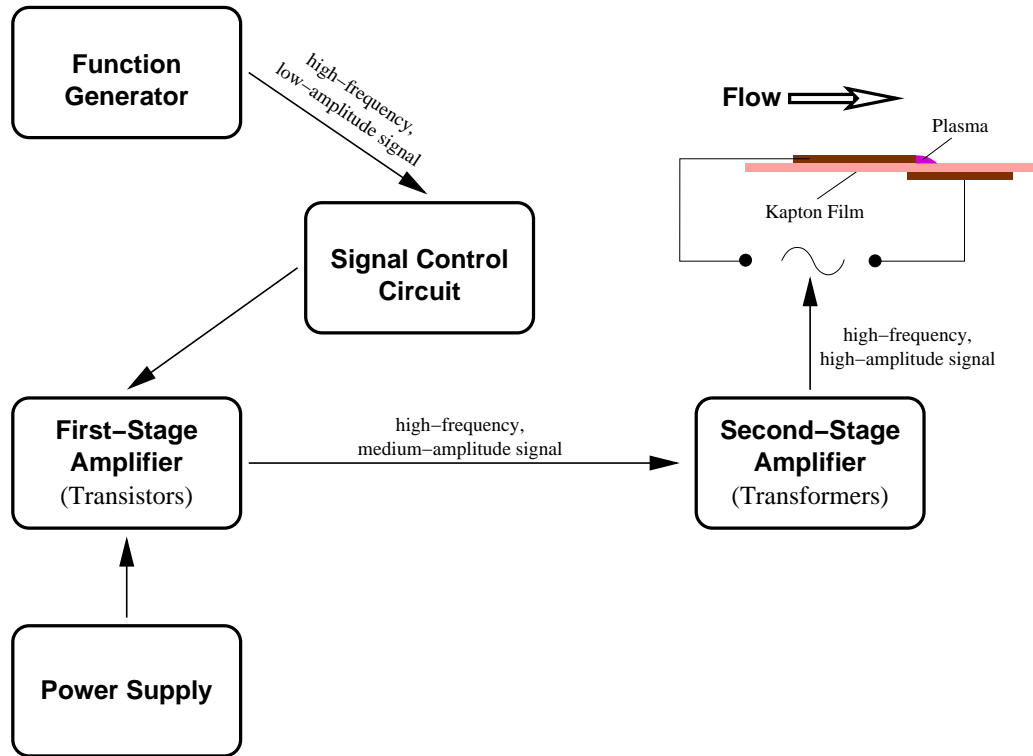
Figure 2.20. A specially-designed circuit was used to generate high a.c. voltage.
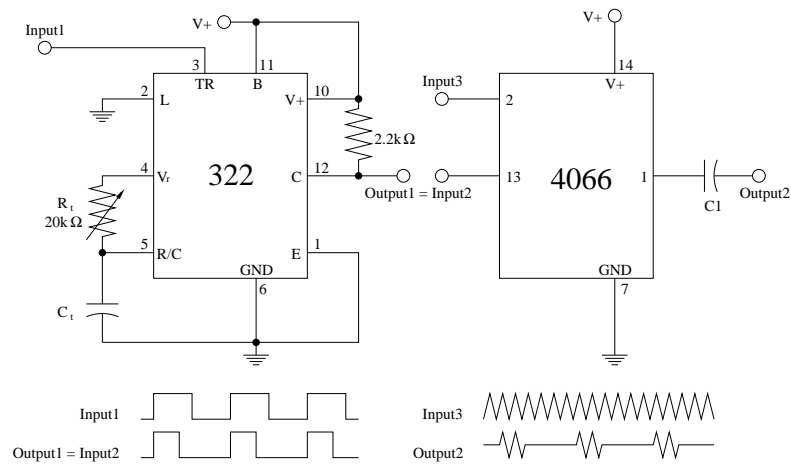
Figure 2.21. This circuit is based on LM322N and CD4066. It was used to control the duty cycle and the frequency of unsteady pulsing.

input (input3) from another function generator gives an unsteady pulse signal with desired frequency and duty cycle.

2.8   Wake Profile Measurements

Bulk flow instrumentation consists of a total-static pitot tube and a large Velmex 2-D traverse system. A 15-inch-long slot was cut into the top wall of the test section at one axial chord length downstream the trailing edge of the center blade. The slot is parallel to the trailing edge of the cascade and allows us to measure the wakes of two consecutive blades. The pitot tube was mounted on the Velmex traverse system, as shown in Figure 2.22. Figure 2.23 shows a photograph of the pitot tube measuring the wake profile behind the center blade.
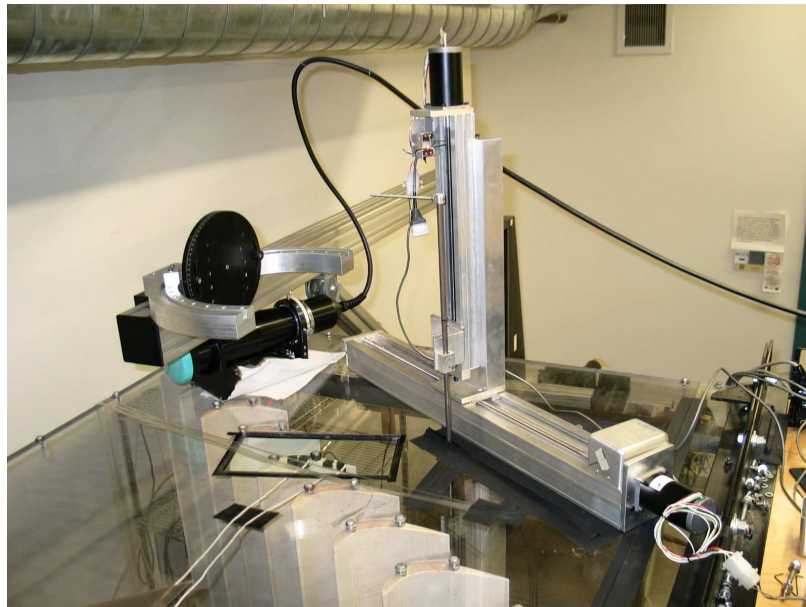
Figure 2.22. A traverse slot was cut into the top of the test section so that the traverse system can move the five-hole probe along the trailing edge of the cascade.

Figure 2.23. A commercially-made five-hole probe was used to measure the blade wake profiles.

2.9 Flow Visualization

Flow visualization was conducted by combining particle streams and a laser sheet. The particles generated by a TSI droplet generator were introduced into the wind tunnel at the tunnel inlet. The amount of the particles and the location of injection were carefully adjusted so that appropriate amount of particles flew through the cascade channels surrounding the center blade. The laser sheet was projected into the cascade from the trailing edge at the height of particle streams. In the case of unsteady actuator pulsing, in order to capture the vortex shedding from the plasma actuators, a laser chopper was inserted between the laser sheet projector and the laser generator. The chopper is a device with an orifice which can be controlled to open and close at desired frequencies. This way the shining frequency of the laser sheet can be controlled.

The recording of the flow video was done by using a Sony DCR-TRV740 digital

camcorder. The Sony camcorder was mounted on the triangular traverse beam where the transceiver for LDV measurements was mounted, as shown in Figure 2.24.
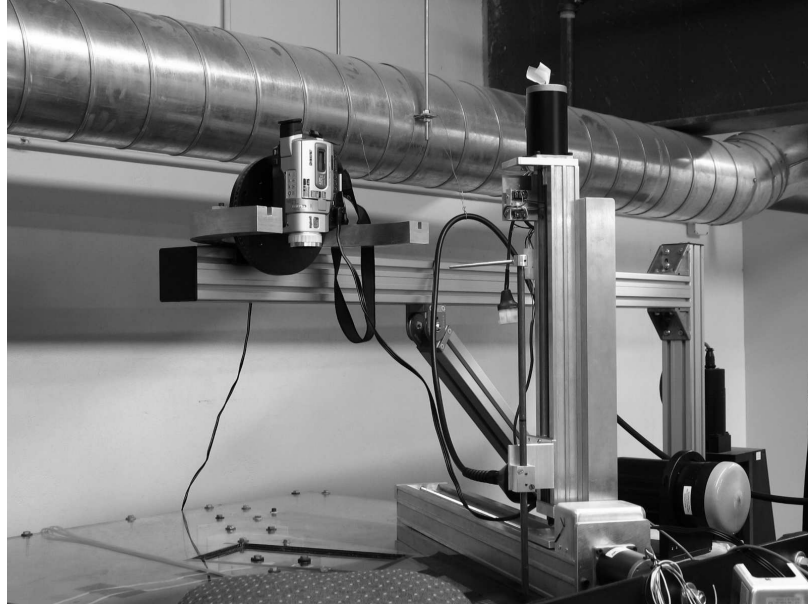
Figure 2.24. A Sony DCR-TRV740 digital camcorder was mounted on the LDV traverse beam and used to record the flow video.

2.10   Computer Acquisition System

Data acquisition and other control aspects of the experiment were automated and executed via a PC running RedHat Linux. The PC was equipped with a PowerDAQ PD2-MFS-8-500/14DG board. The board is a 14-bit board. The maximum range of the analog input to the board is ± 10 V. Thus the minimum voltage that it can resolve is 20 V/2^{14} = 1.22 mV.

2.11   Experimental Conditions

2.11.1   Reynolds Number

In the reviewed work, two different Reynolds numbers were used. The first one, Re_c, is based on the freestream (or inlet) velocity U_∞ and the axial chord length C_x

while the other one, Re_{ss}, is based on the exit velocity U_{exit} and the suction surface length L_{ss}. Since the flow velocity falls in the range of incompressible flow, the relationship between U_∞ and U_{exit} can be derived by one-dimensional incompressible continuity equation

$$\rho_1 U_\infty A_1 = \rho_2 U_{exit} A_2. \tag{2.2}$$

For the incompressible flow, $\rho_1 = \rho_2$. Thus the above equation becomes

$$\frac{U_{exit}}{U_\infty} = \frac{A_1}{A_2}. \tag{2.3}$$

The ratio between A_1 and A_2 is 1.638 in my experimental setup. In addition, for the "PakB" blade, the ratio between C_x and L_{ss} is 0.689 (see Figure 2.25). Therefore, the relationship between Re_c and Re_{ss} is
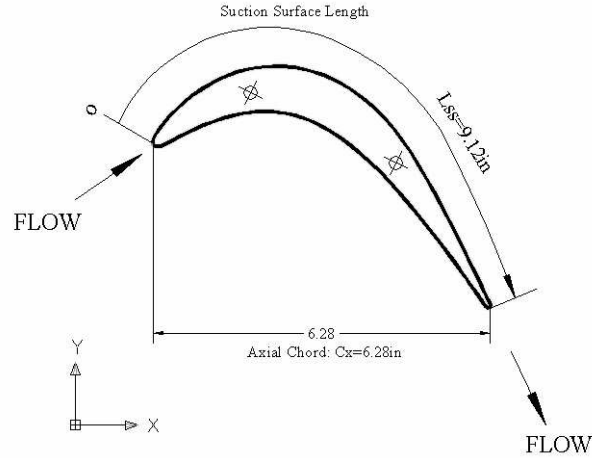
Figure 2.25. The axial chord length and the suction surface length.

$$\frac{Re_{ss}}{Re_c} = 2.377. \tag{2.4}$$

In this research work Re_c was used. Table 2.6 gives the Reynolds numbers that were examined in this work and the corresponding Reynolds numbers based on the exit velocity and the suction surface length.

TABLE 2.6

THE REYNOLDS NUMBERS EXAMINED IN THIS RESEARCH WORK

Re_c	10,000	25,000	50,000	75,000	100,000
Re_{ss}	23,770	59,425	118,850	178,275	237,700

2.11.2   Uncontrolled Cases – Baseline Flow

One of the objectives of this research work was to document the flow separation that occurs on the suction side of LPT blades at low Reynolds numbers. Similar research [2] showed that both the Reynolds number and the turbulence intensity are critical parameters for this work. In order to obtain a comprehensive understanding of the flow, significant amount of measurements were conducted for the baseline flow conditions. Table 2.7 shows a measurements matrix for the baseline flow conditions.

2.11.3   Steady Plasma Actuator Optimization

The approach of flow control in this research work was based on the use of plasma actuators. As mentioned earlier, the plasma actuators can generate wall jets, span-wise vortices, and streamwise vortices, depending on the orientation of electrodes. This is illustrated in Figure 2.26. The first objective with plasma actuators was to optimize their configurations. Table 2.8 shows the cases that have been done to optimize the plasma actuators.

2.11.4   Controlled Cases – Steady Plasma Actuators

The baseline flow measurements gave us a complete map of the flow field in the "PakB" cascade. Combining the pressure distributions and the boundary layer profiles clearly showed the flow separation region(s) on the suction side of "PakB"

TABLE 2.7

BASELINE FLOW EXPERIMENTAL CONDITIONS

Re	FSTI	Pressure	LDV	Hot-Wire
10,000	0.08%	√		
	1.60%	√		
	2.85%	√		
25,000	0.08%	√		
	1.60%	√		
	2.85%	√		
50,000	0.08%	√	√	√
	1.60%	√		
	2.85%	√	√	
75,000	0.08%	√	√	√
	1.60%	√		
	2.85%	√	√	
100,000	0.08%	√	√	√
	1.60%	√		
	2.85%	√	√	
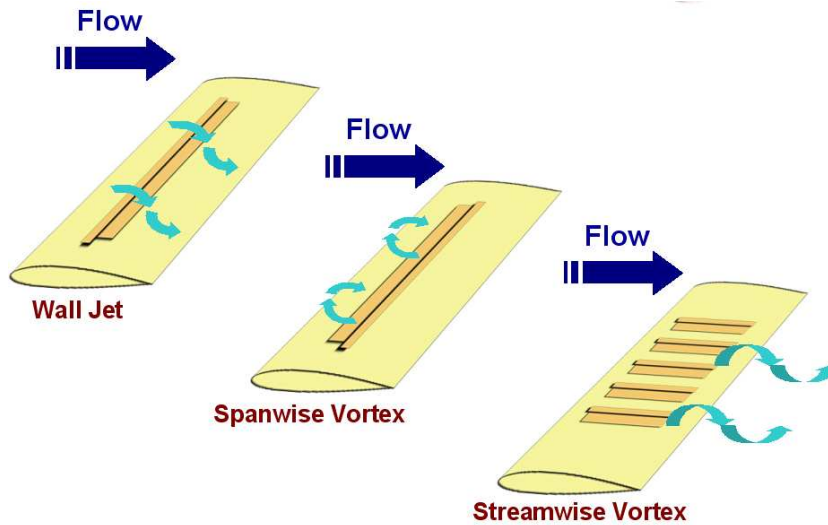
Figure 2.26. Plasma actuators can generate wall jets, spanwise vortices, and stream-wise vortices, depending on the orientation of the electrodes.

TABLE 2.8

OPTIMIZATION MATRIX FOR STEADY PLASMA ACTUATORS

Case No.	Single or Dual?	Location of First PA	Location of Second PA	Configuration
1	Single	60% Cx	N/A	Wall Jet
2	Single	60% Cx	N/A	Wall Jet
3	Single	67.5% Cx	N/A	Wall Jet
4	Single	67.5% Cx	N/A	Spanwise Vortex
5	Single	67.5% Cx	N/A	Wall Jet & Spanwise Vortex
6	Single	72.5% Cx	N/A	Wall Jet
7	Dual	67.5% Cx	75% Cx	Wall Jet
8	Dual	67.5% Cx	77.5% Cx	Wall Jet
9	Dual	67.5% Cx	85% Cx	Wall Jet

blades.

From the results of actuator optimizations, it was found that flow control is most efficient when it was applied just before the separation point. In this research work, the separation point was found to be close to 70% Cx. The separation point was also found not sensitive to Reynolds number and turbulence intensity. Thus the plasma actuators were placed at 67.5% Cx for most of the measurements. Table 2.9 shows a measurements matrix for steady plasma actuators. Note that the LDV measurements were conducted at seven different streamwise locations listed in Table 2.4.

2.11.5   Controlled Cases – Unsteady Plasma Actuators

In addition to steady plasma actuators, unsteady plasma actuators were also designed and applied to control the blade flow separation in this work. Different excitation frequencies and duty cycles were tested, as shown in Table 2.10.

TABLE 2.9

EXPERIMENTAL CONDITIONS WITH STEADY PLASMA ACTUATORS

Re	FSTI	Pressure	LDV	Hot-Wire
10,000	0.08%	√		
25,000	0.08%	√		
50,000	0.08%	√	√	
75,000	0.08%	√		
100,000	0.08%	√		

TABLE 2.10

EXPERIMENTAL CONDITIONS WITH UNSTEADY PLASMA ACTUATORS

Case No.	Excitation Frequencies (Hz)	Amplitude of Voltage (kV)	Duty Cycles	Dielectric Layer
1	1, 2, 5, 10, 20, 30, 40, 50, 60	8	10%, 20%, 30%, 37.4%, 50%	kapton
2	10, 20, 30, 40, 50, 60, 80, 100, 120, 160, 200	20, 24, 28	10%, 20%	macor

CHAPTER 3

BASELINE RESULTS – SEPARATION REGIONS ON "PAKB" BLADES

The objectives of the baseline measurements were to examine the effects of the Reynolds number and the freestream turbulence intensity on the flow over "PakB" blades. This was documented through the surface pressure distributions and the boundary layer profiles.

The pressure coefficient presented in this dissertation is defined as

$$C_p = \frac{p - p_\infty}{q} = \frac{p - p_\infty}{\frac{1}{2}\rho U_\infty^2},$$ (3.1)

where C_p is the pressure coefficient, p is the blade surface pressure, p_∞ is the freestream pressure upstream the cascade, q is the dynamic pressure, ρ is the air density, and U_∞ is the freestream velocity measured upstream the cascade.

3.1 The Effect of Reynolds Number

The pressure distributions on the blade for the Reynolds number range, $10,000 \leqslant Re_c \leqslant 100,000$, and the lowest freestream turbulence intensity of FSTI=0.08%, are shown in Figure 3.1. Also shown is the computed pressure distribution based on an Euler (inviscid) code [23]. The computations are equivalent to an infinite Reynolds number. Therefore they should indicate the distribution without flow separation. Comparing the measured distribution to the calculated distribution clearly indicates the region(s) of separation.
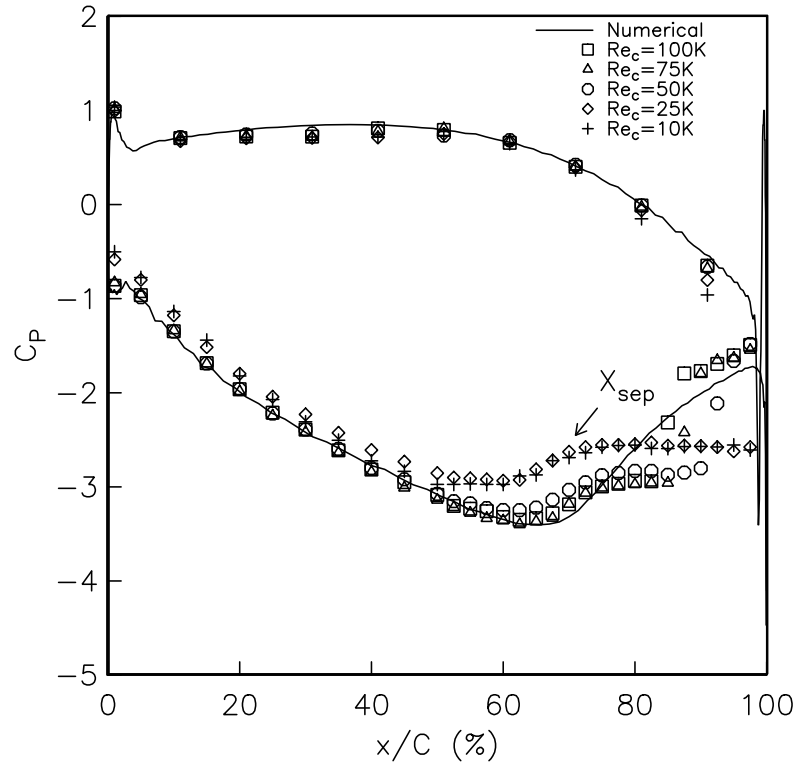
Figure 3.1. Blade pressure coefficient distributions for different Reynolds numbers, for the lowest freestream turbulence intensity (FSTI=0.08%), and comparison to Euler simulation (Romeo [23]).

Defining the location of separation requires some judgment. Schlichting [?] showed that the pressure distribution in a laminar separation bubble can be simplified as this: a nearly constant pressure from the separation point to the maximum height of the separation bubble. The pressure then increases linearly to reach the freestream pressure at the reattachment point, as is shown in Figure 3.2.
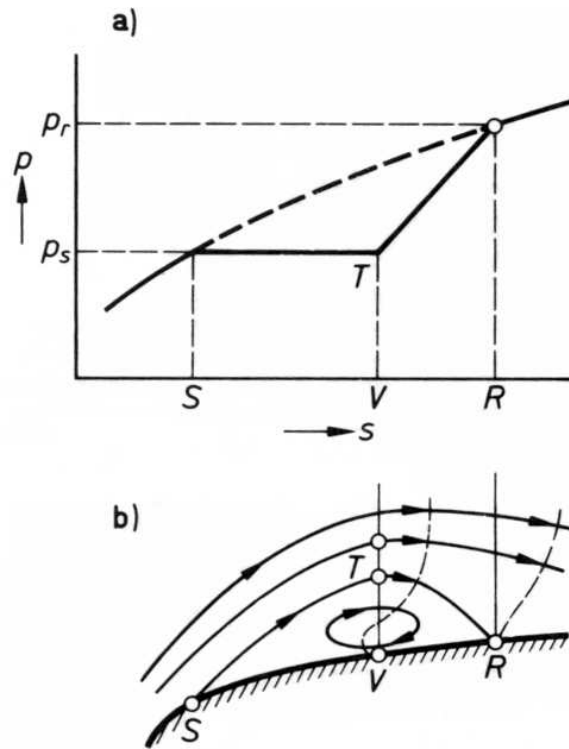
Figure 3.2. "Separation bubble in a laminar boundary layer. a) Pressure distribution in bubble along the wall (schematic). The pressure between S and V in the bubble remains constant at p_s; further downstream the pressure increases to p_r. b) Shape of bubble (schematic): S=point of separation; R=point of reattachment; V-T=height of bubble." (from Schlichting [?])

Consistent with Schlichting [?], the separation point is marked as the starting point of the nearly constant region of C_p, near the trailing edge of the suction side of the blade. For each of the Reynolds number cases shown in Figure 3.1, separation occurs at $x/C_x \approx 70\%$ as indicated.

The location of reattachment is easier to define. It is marked as the location where the C_p value jumps from the nearly constant values that are the indication of a separated region and begins to follow the inviscid distribution close to the trailing edge. At $Re_c = 100,000$, this occurs at $x/C_x \approx 87.5\%$. For Re_c below $25,000$ the flow never reattaches at this low turbulence condition.

The locations of the separation and reattachment for the low disturbance condition are summarized in Figure 3.3. The region between the two curves corresponds to a separation region that exists on the suction side of the blade. Note that the separation location is fairly insensitive to Re_c while the reattachment location varies significantly.
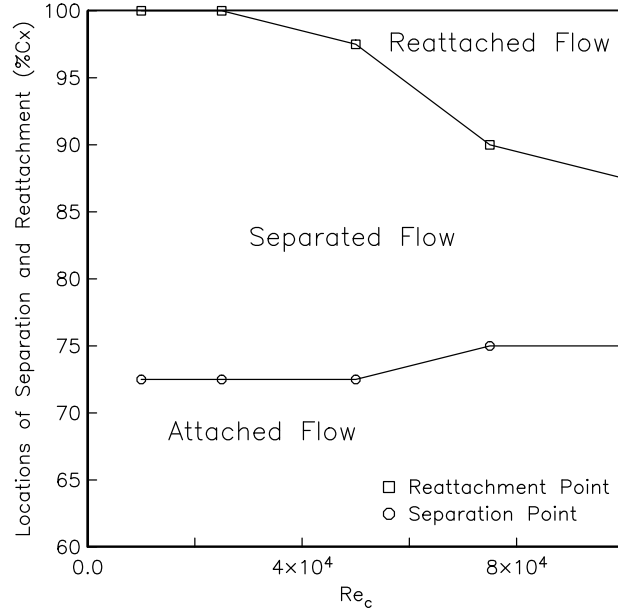
Figure 3.3. Separation and reattachment locations as a function of Reynolds number for the lowest turbulence intensity (FSTI=0.08%).

The locations of separation and reattachment summarized in Figure 3.3 are validated by the LDV measurements. The boundary layer profiles at seven different streamwise locations are shown in Figure 3.4 for $Re_c = 100,000$. The flow is attached

at both $x/C_x = 50\%$ and $x/C_x = 60\%$ at this Reynolds number. The measured boundary layer profiles match the Blasius solutions very well, which indicates the boundary layer is laminar at these two locations.

At $x/C_x = 70\%$, the boundary layer is still attached since $\frac{\partial u}{\partial y}|_{y=0} > 0$. At $x/C_x = 75\%$, the velocity of the flow remains nearly zero from 0 to 0.5 mm wall normal distance, which gives $\frac{\partial u}{\partial y}|_{y=0} = 0$ and is a clear sign that the boundary layer is separated. This indicates that the separation location is between $x/C_x = 70\%$ and $x/C_x = 75\%$. The predicated separation location from the pressure distributions is at $x/C_x = 75\%$, which falls in this range.

It also can be seen from Figure 3.4 that the height of the separation bubble increases from 0.8 mm at $x/C_x = 75\%$ to 1.6 mm at $x/C_x = 80\%$. After the flow passes $x/C_x = 80\%$, the boundary layer becomes turbulent and quickly reattaches to the blade surface at $x/C_x = 85\%$. The predicated reattachment location by the pressure distributions ($x/C_x = 87.5\%$) is correct considering that the physical resolution of the pressure ports is $2.5\%C_x$.

The boundary layer profiles for $Re_c = 75,000$ and $Re_c = 50,000$ are shown in Figure 3.5 and Figure 3.6, respectively. Like the case for $Re_c = 100,000$, the separation location are found to be between $x/C_x = 70\%$ and $x/C_x = 75\%$ for both Reynolds numbers. Again, the predicated separation locations by the pressure distributions are correct within the physical resolution of the pressure ports.

As to the reattachment location, the boundary layer profiles prove that the predication by the pressure distributions is correct and accurate for $Re_c = 75,000$. For $Re_c = 50,000$, the predicated reattachment location is $x/C_x = 97.5\%$. Although I don't have a boundary layer profile at this location, it can be said with the accuracy of one pressure port that the flow reattaches at $x/C_x = 97.5\%$ at $Re_c = 50,000$, given the fact that predication by the pressure distributions works well for both
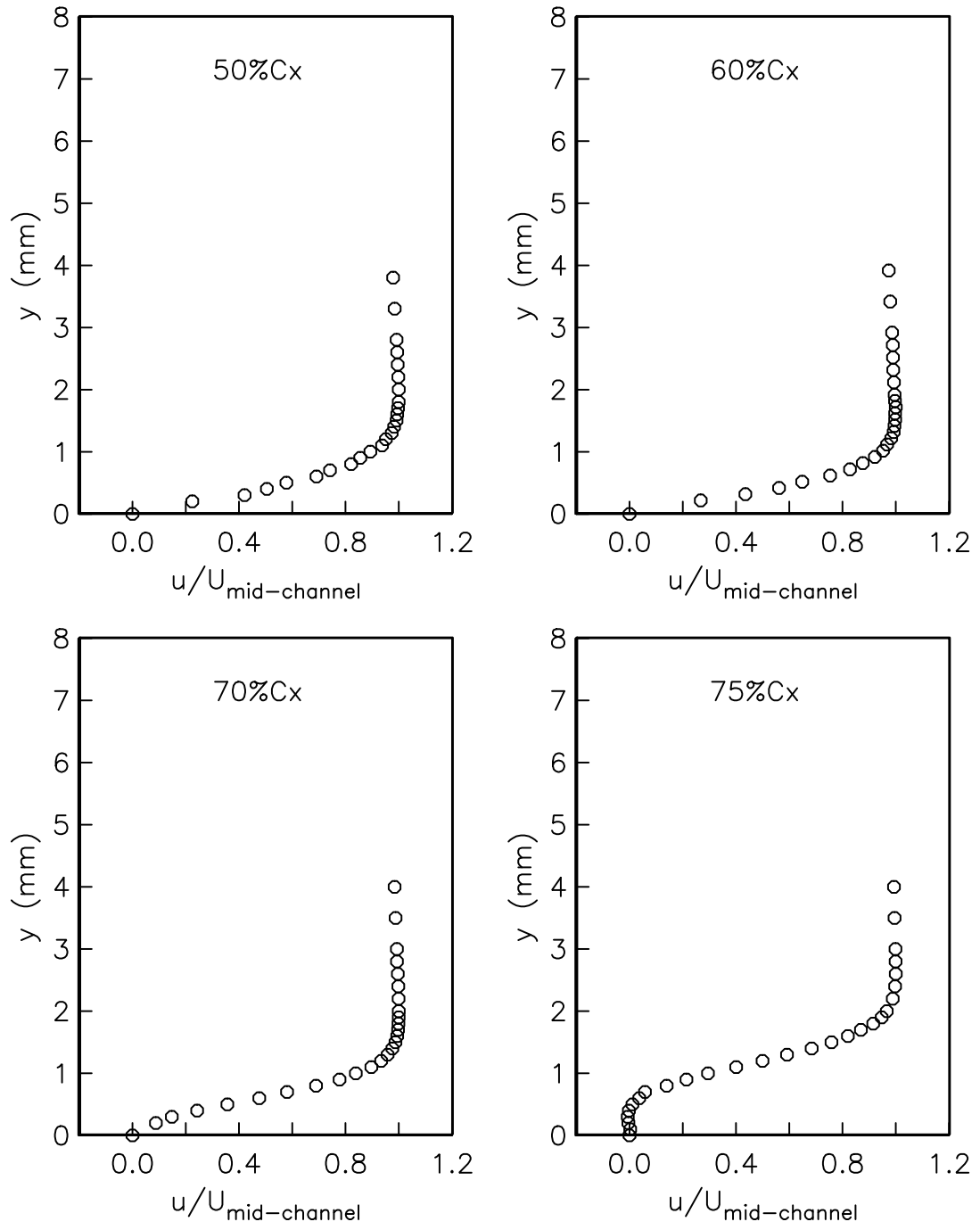
Figure 3.4. Boundary layer profiles for Re=100,000 and FSTI=0.08%.
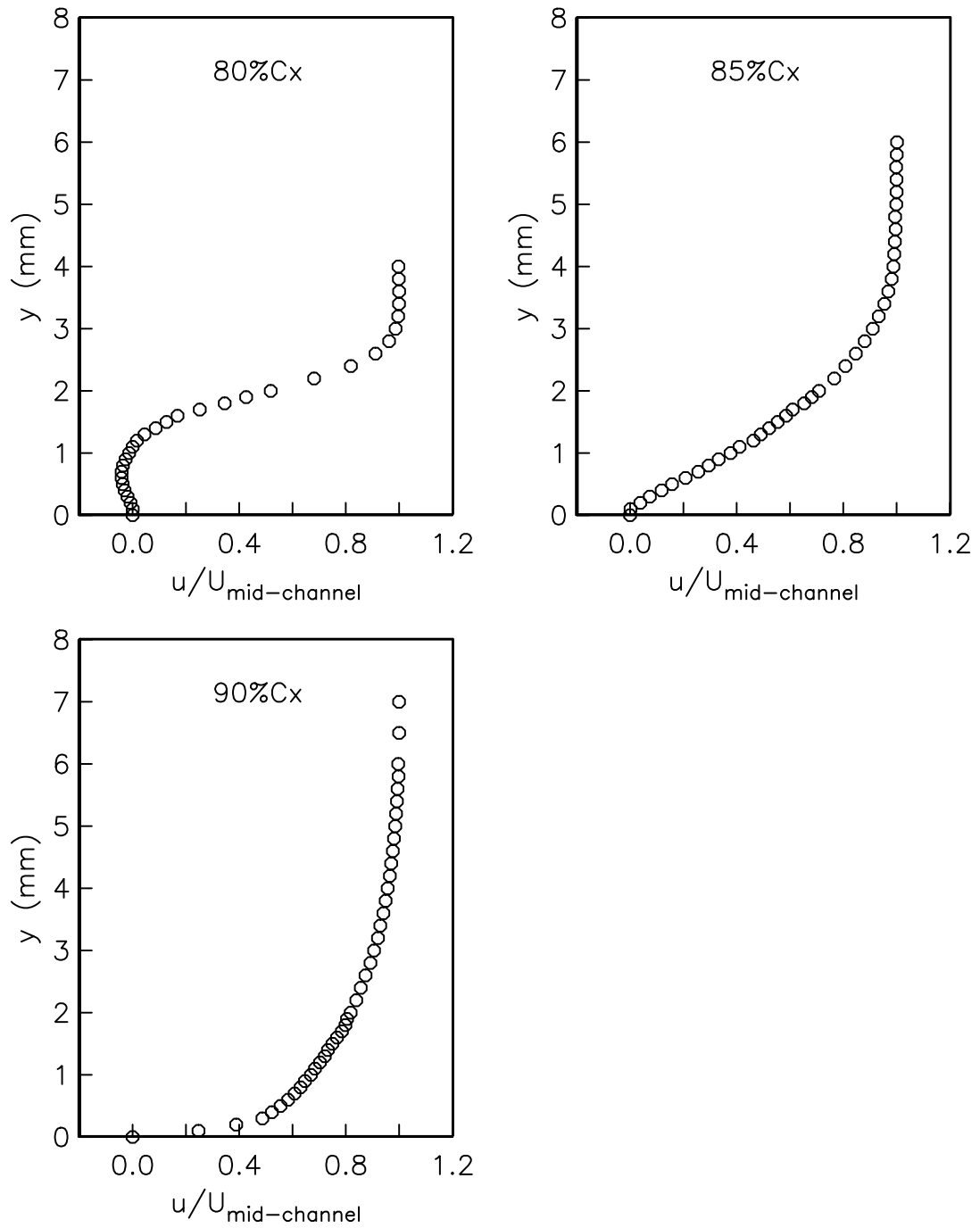
Figure 3.4 (continued). Boundary layer profiles for Re=100,000 and FSTI=0.08%.
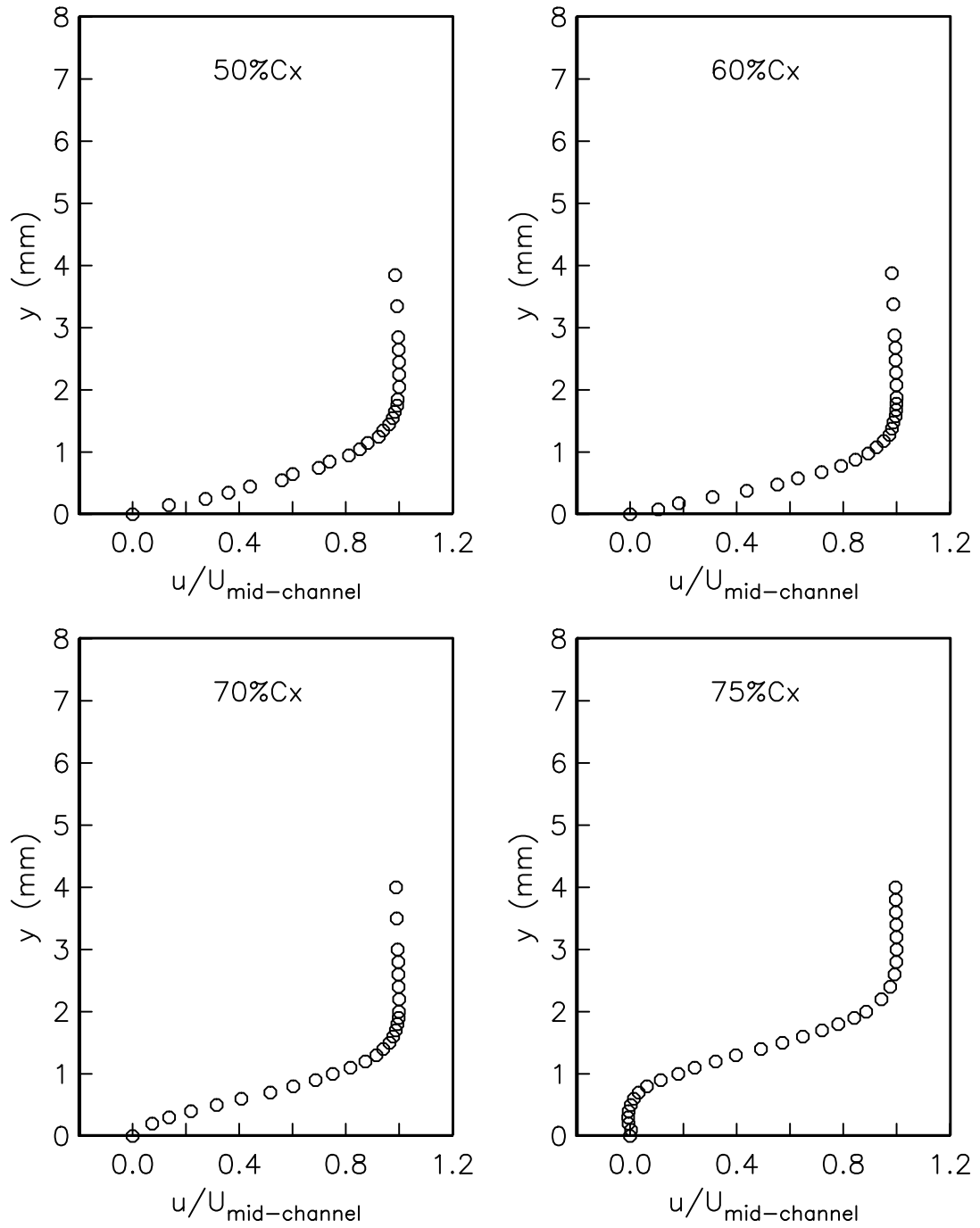
Figure 3.5. Boundary layer profiles for Re=75,000 and FSTI=0.08%.
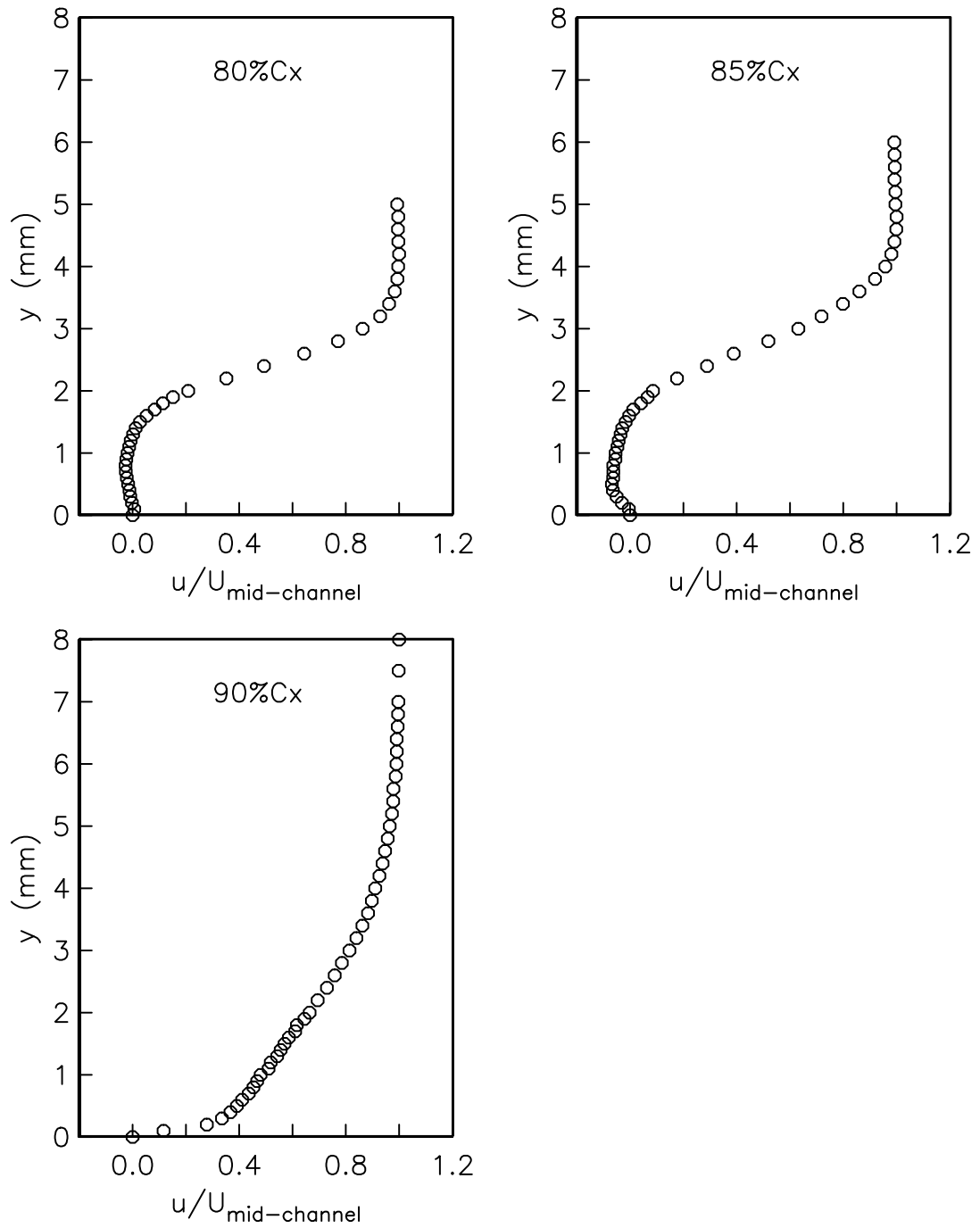
Figure 3.5 (continued). Boundary layer profiles for Re=75,000 and FSTI=0.08%.
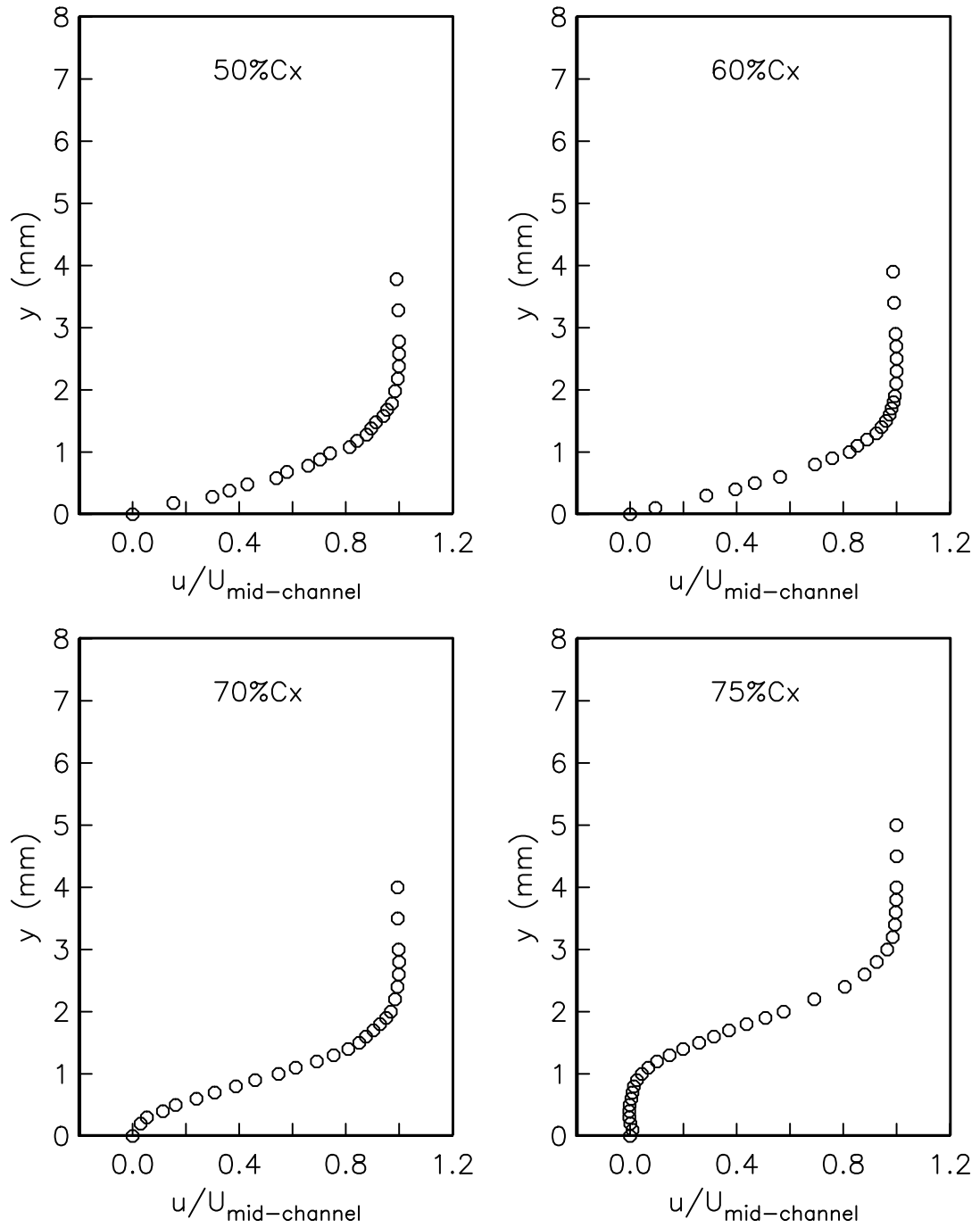
Figure 3.6. Boundary layer profiles for Re=50,000 and FSTI=0.08%.
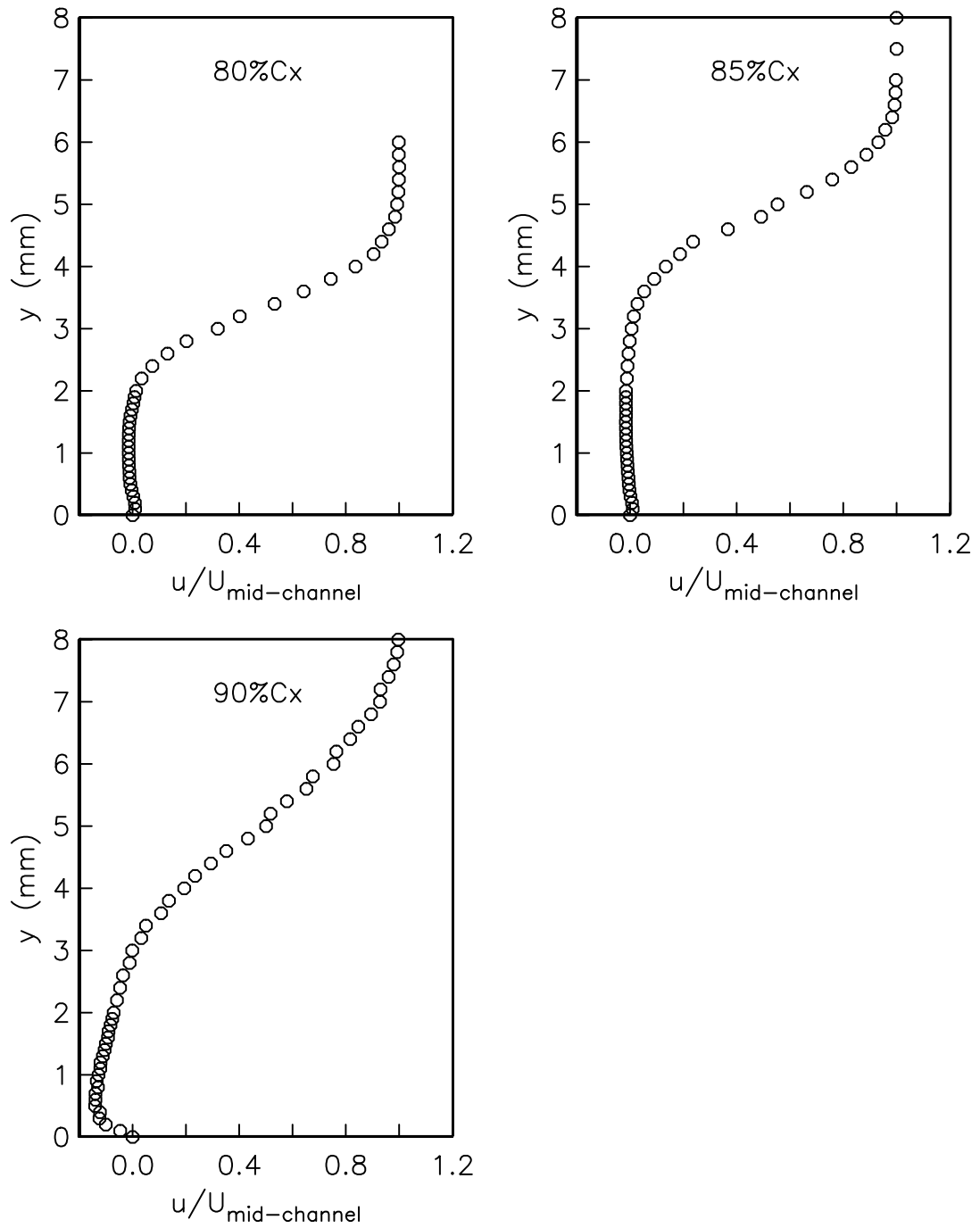
Figure 3.6 (continued). Boundary layer profiles for Re=50,000 and FSTI=0.08%.

$Re_c = 100,000$ and $Re_c = 75,000$.

The effect of the chord Reynolds number can be seen by a direct comparison of the boundary layer profiles between two Reynolds numbers. Figure 3.7 shows the boundary layer profiles for two Reynolds numbers ($Re_c = 50,000$ and $Re_c = 100,000$). At the same streamwise location, the boundary layer is thicker for the lower Reynolds number ($Re_c = 50,000$). At $x/C_x = 75\%$, the flow is separated for both Reynolds numbers but the height of the separation bubble for $Re_c = 50,000$ is larger than that for $Re_c = 100,000$. Higher Reynolds number results in an earlier reattachment of the flow. At $x/C_x = 85\%$, there is still a large separation region for $Re_c = 50,000$ while the flow is already attached for $Re_c = 100,000$.

A combination of these boundary layer profiles on "PakB" blades can clearly show the separation bubbles on the suction surface. Figure 3.8 shows the boundary layer profiles for three chord Reynolds numbers on a "PakB" blade. The separation bubbles are sketched using dashed lines. As the chord Reynolds number increases from $50,000$ to $100,000$, the separation bubble size decreases from 25% of axial chord to 12.5% of axial chord.
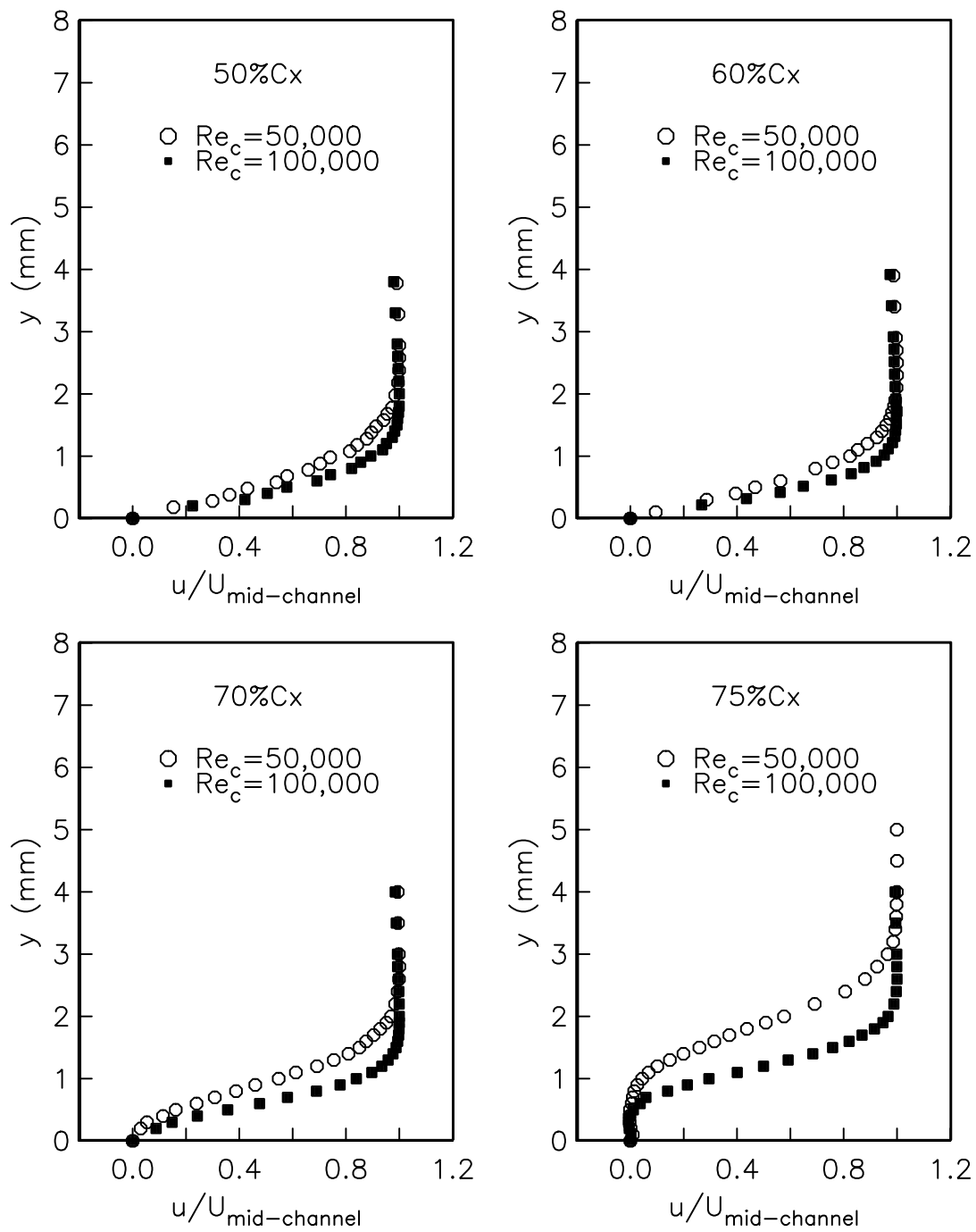
Figure 3.7. Boundary layer profiles for $Re_c = 50,000$ and $Re_c = 100,000$ for FSTI=0.08%.
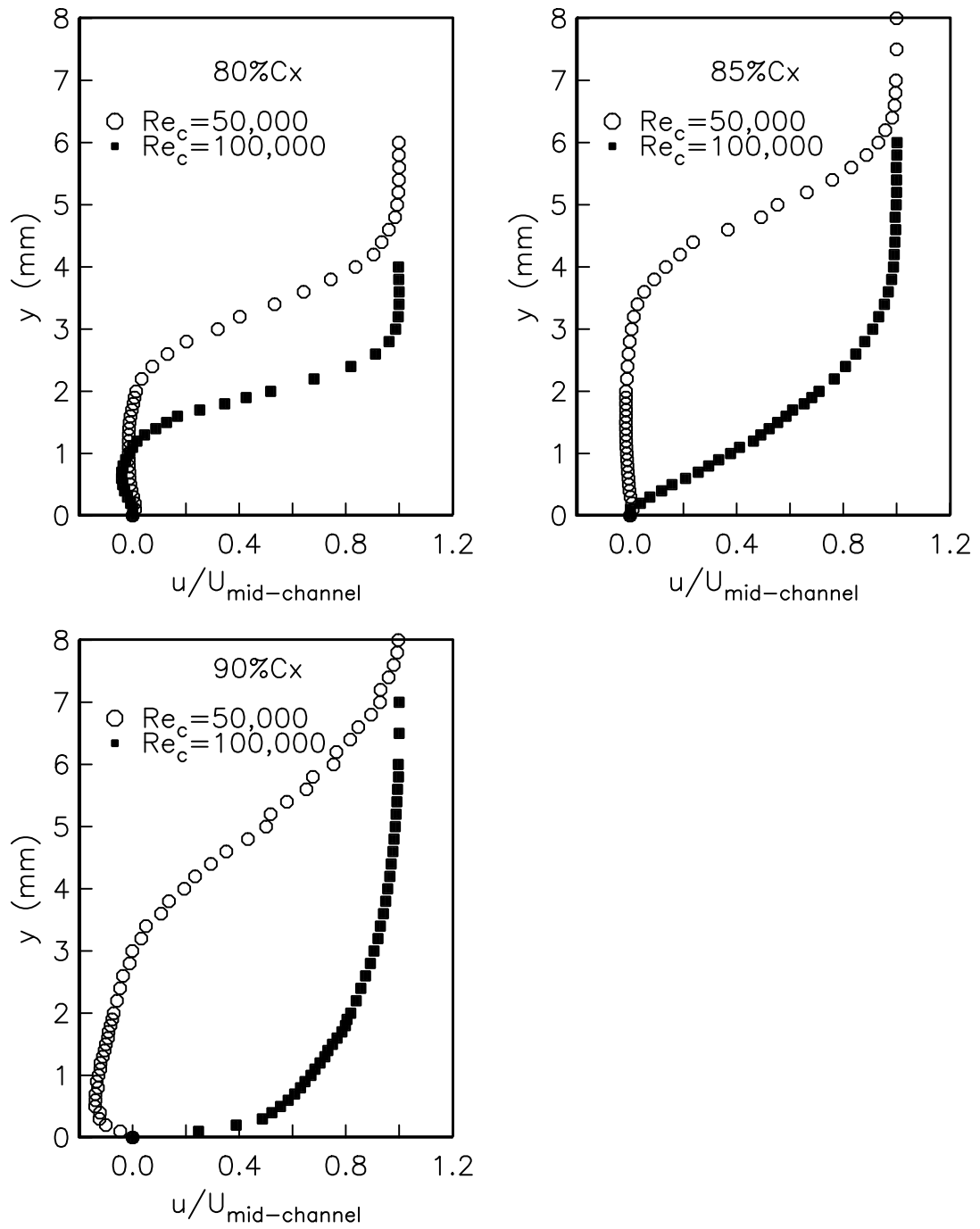
Figure 3.7 (continued). Boundary layer profiles for $Re_c = 50,000$ and $Re_c = 100,000$ for FSTI=0.08%.
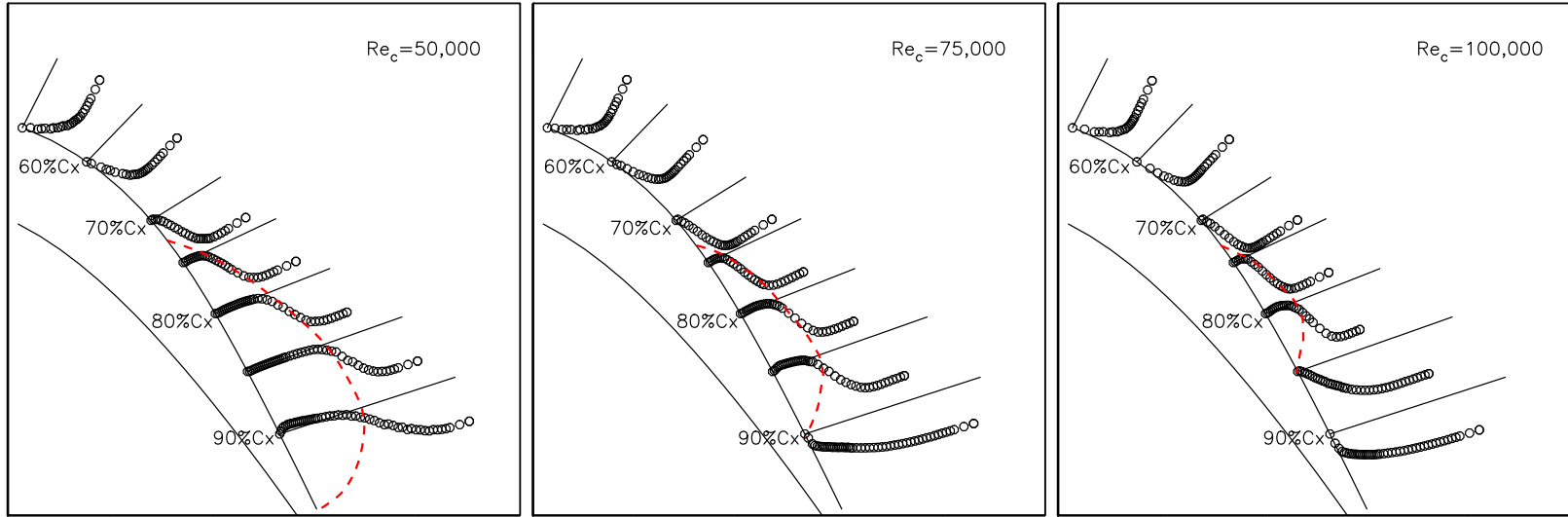
Figure 3.8. Boundary layer profiles on "PakB" blade for three different chord Reynolds numbers. The dashed lines sketch the separation bubbles. The size of the separation bubble decreases as chord Reynolds number increases.

3.2   The Effect of Freestream Turbulence Intensity

The freestream turbulence intensity was increased using the turbulence genera-
tors shown in Figure 2.7. When "Grid 3" was located 30 in. upstream the center
blade, it gave a freestream turbulence intensity of FSTI=1.6%, which was 20 times
higher than the freestream turbulence intensity without the grid. When "Grid 0"
was located 30 in. upstream the center blade, it gave a freestream turbulence in-
tensity of FSTI=2.85%, which was 36 times higher than the freestream turbulence
intensity without the grid, and 1.75 times that of "Grid 3".

The effect of the higher turbulence intensity of FSTI=1.6% on the pressure dis-
tribution is shown in Figure 3.9. These are for the full range of Reynolds numbers,
$10,000 \leqslant Re_c \leqslant 100,000$. Again the pressure distribution based on an Euler (in-
viscid) code [23] is also presented. The pressure distributions indicate a relative
insensitivity of the separation location to the higher freestream turbulence inten-
sity. The location is still approximately at $x/C_x = 70\%$. However, compared to the
low turbulence condition in Figure 3.1, and with the exception of $Re_c = 100,000$,
the location for reattachment has moved upstream with the higher freestream tur-
bulence intensity. This is most dramatic at $Re_c = 25,000$ which previously did not
reattach at the lower turbulence intensity. At this intermediate turbulence intensity,
the flow reattaches at the trailing edge of the blade at $Re_c = 25,000$.

The pressure distributions for the highest turbulence intensity of FSTI=2.85%
are shown in Figure 3.10. This higher turbulence intensity had a minimal effect on
the reattachment location compared to the previous case at FSTI=1.60%. However,
aside from this separation region, the distributions collapse much better onto the
Euler solution [23]. In particular, near the leading edge on the pressure side of
the blade, a much better agreement at the high turbulence intensity is observed.
Comparing this region on the blade to the other cases in Figures 3.1 and 3.9, I
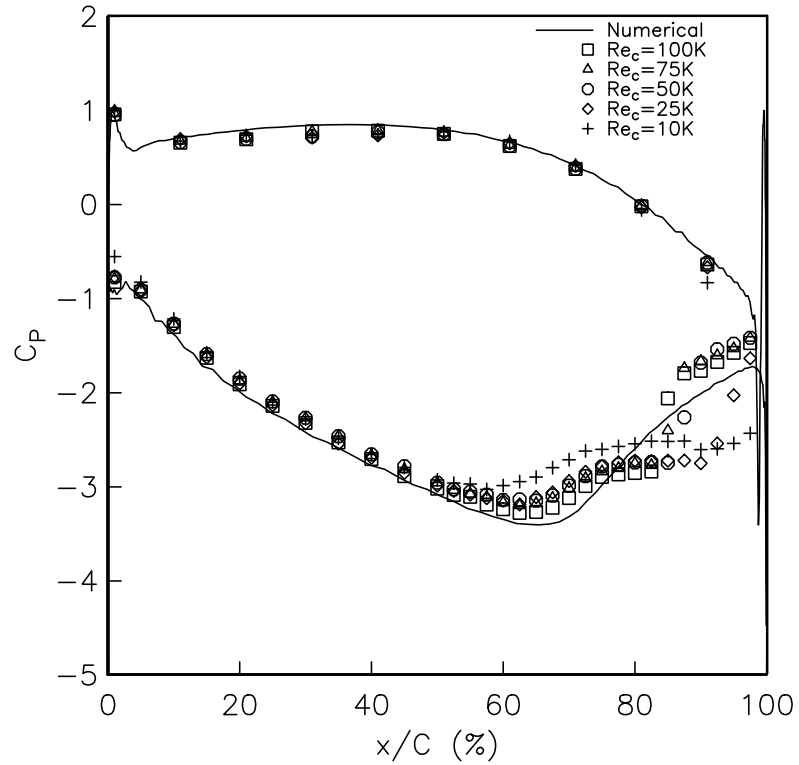
Figure 3.9. Blade pressure coefficient distributions for different Reynolds numbers, for the medium freestream turbulence intensity (FSTI=1.60%), and comparison to Euler simulation (Romeo [23]).

74

suspect that a small separation bubble exists just downstream the leading edge on the pressure side. The highest turbulence intensities in this case are enough to cause this to collapse.
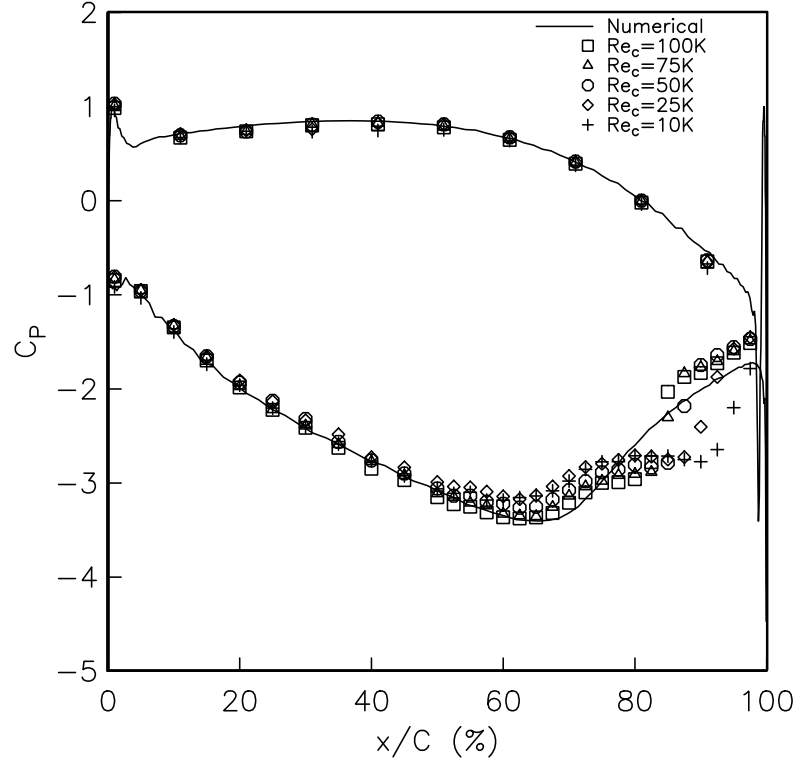
Figure 3.10. Blade pressure coefficient distributions for different Reynolds numbers, for the highest freestream turbulence level (FSTI=2.85%), and comparison to Euler simulation (Romeo [23]).

The effect of the turbulence intensity can be seen in the boundary layer profiles too. Figure 3.11 shows the measured boundary layer profiles for two different freestream turbulence intensities at $Re_c = 50,000$.

At $x/C_x = 50\%$ and $x/C_x = 60\%$, the flow is attached and the boundary layer profiles almost collapse to each other for two different freestream turbulence intensities. At $x/C_x = 70\%$, the flow is still attached since $\frac{\partial u}{\partial y}|_{y=0} > 0$ for both turbulence intensities. However, $\frac{\partial u}{\partial y}|_{y=0}$ at FSTI=0.08% is slightly smaller than $\frac{\partial u}{\partial y}|_{y=0}$ at
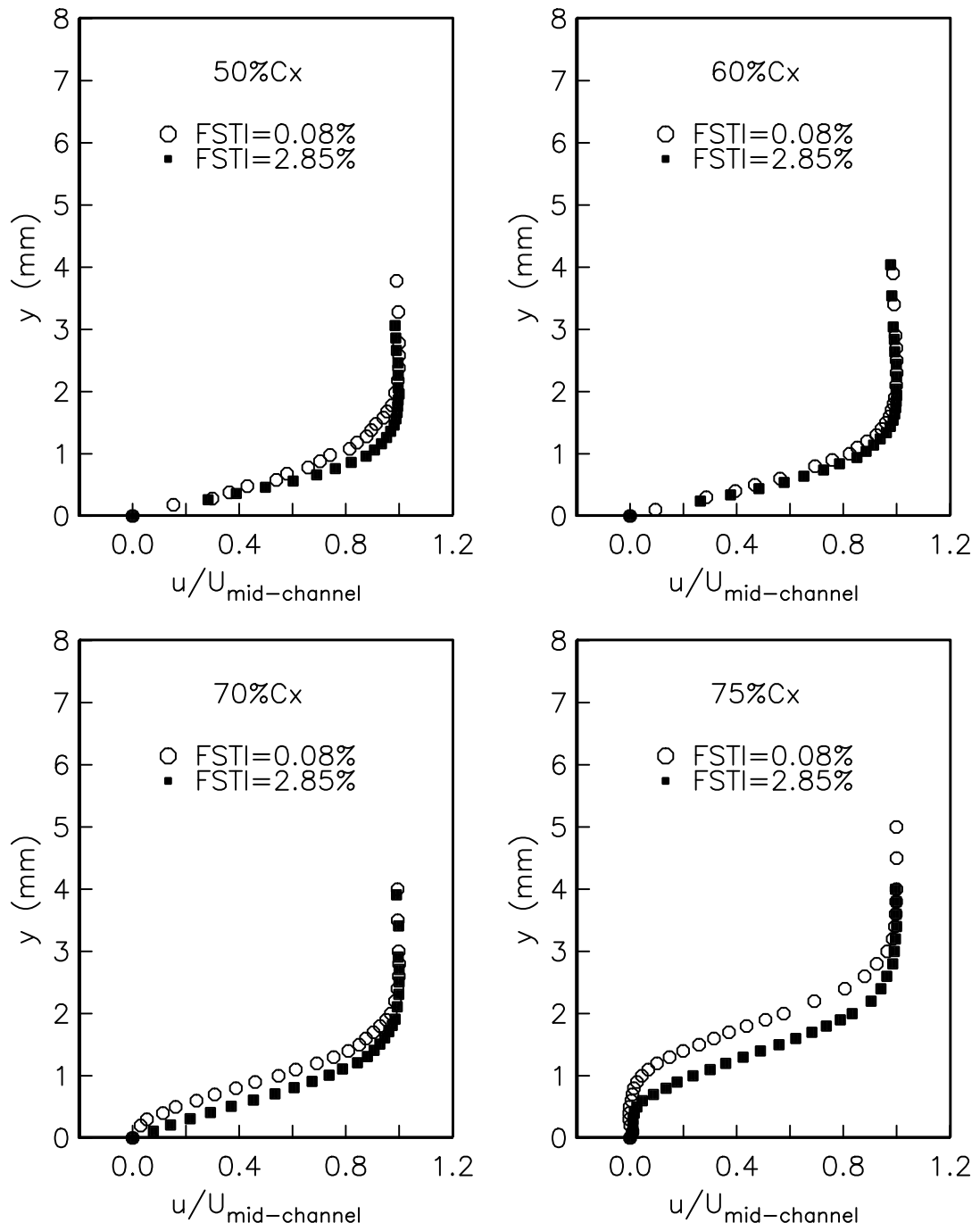
Figure 3.11. The comparison of the boundary layer profiles for two different freestream turbulence intensities at $Re_c = 50,000$.
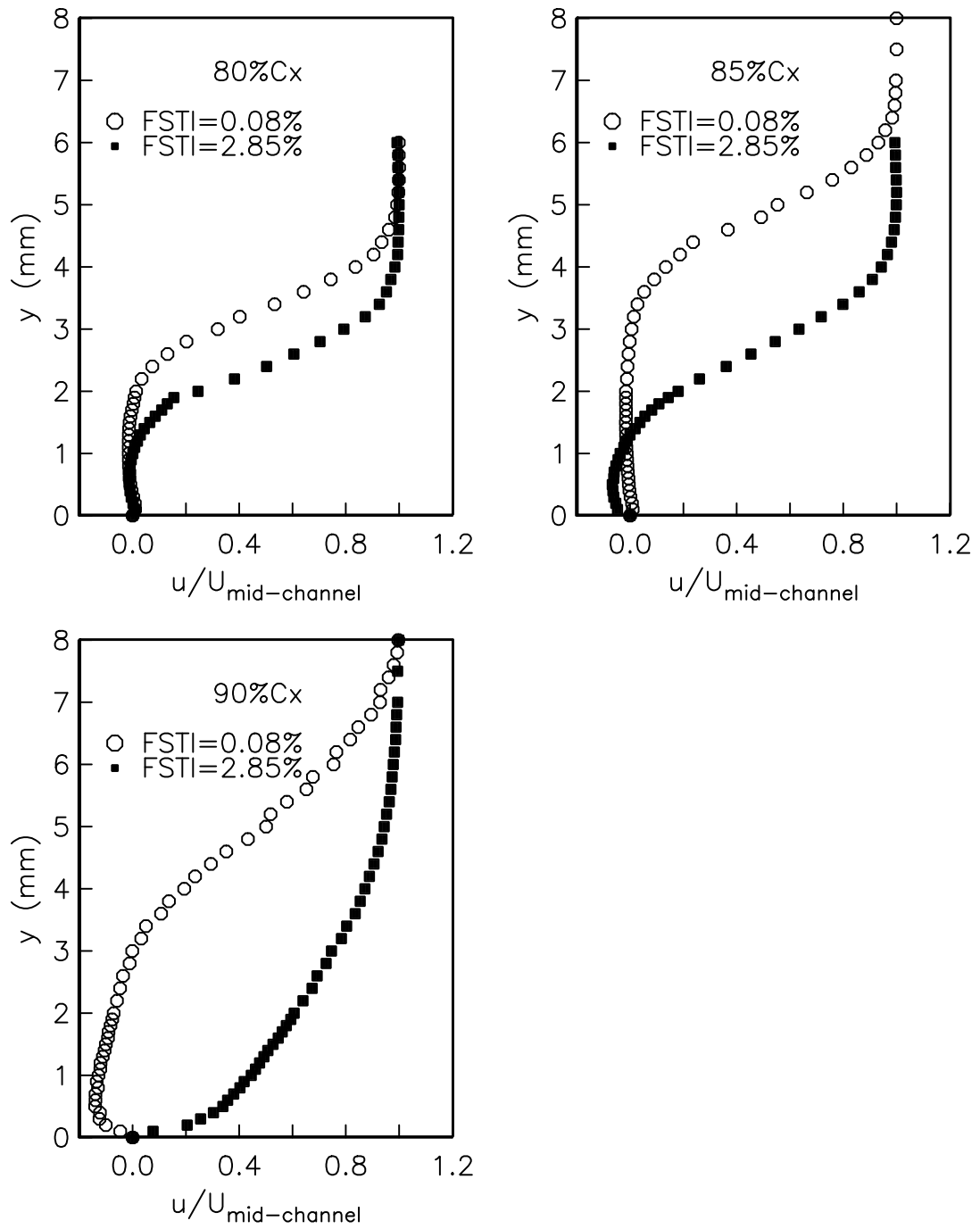
Figure 3.11 (continued). The comparison of the boundary layer profiles for two different freestream turbulence intensities at $Re_c = 50,000$.

FSTI=2.85%. This indicates that the flow is closer to be separated at the lower turbulence intensity.

The boundary layer profiles are significantly different for two freestream turbulence intensities after the flow separates somewhere before $x/C_x = 75\%$. The flow is separated at $x/C_x = 75\%$ for both turbulence intensities but the separation bubble for FSTI=0.08% is much larger that that for FSTI=2.85%. Higher freestream turbulence intensity also moves the reattachment point upstream at this Reynolds number. The flow reattaches at $x/C_x \approx 97.5\%$ for FSTI=0.08% while the flow reattaches at $x/C_x = 90\%$ for FSTI=2.85%.

A comparison of the boundary layer profiles for the lowest and the highest turbulence intensities at $Re_c = 100,000$ is shown in Figure 3.12. Again, the boundary layer profiles almost collapse to each other at $x/C_x = 50\%$ and $x/C_x = 60\%$ where the flow is attached. At this Reynolds number, the similar trend of the flow was observed. The flow is more inclined to separate for the lower freestream turbulent intensity. The separation bubble is larger for the lower freestream turbulence intensity. However, the reattachment location is not affected by the higher turbulence intensity very much at this Reynolds number.

Figure 3.13 shows the separation bubbles sketched by the boundary profiles on the suction surface of the "PakB" blade for two turbulence intensities at $Re_c = 50,000$. The comparison clearly shows the separation bubble is smaller for the higher freestream turbulence intensity.
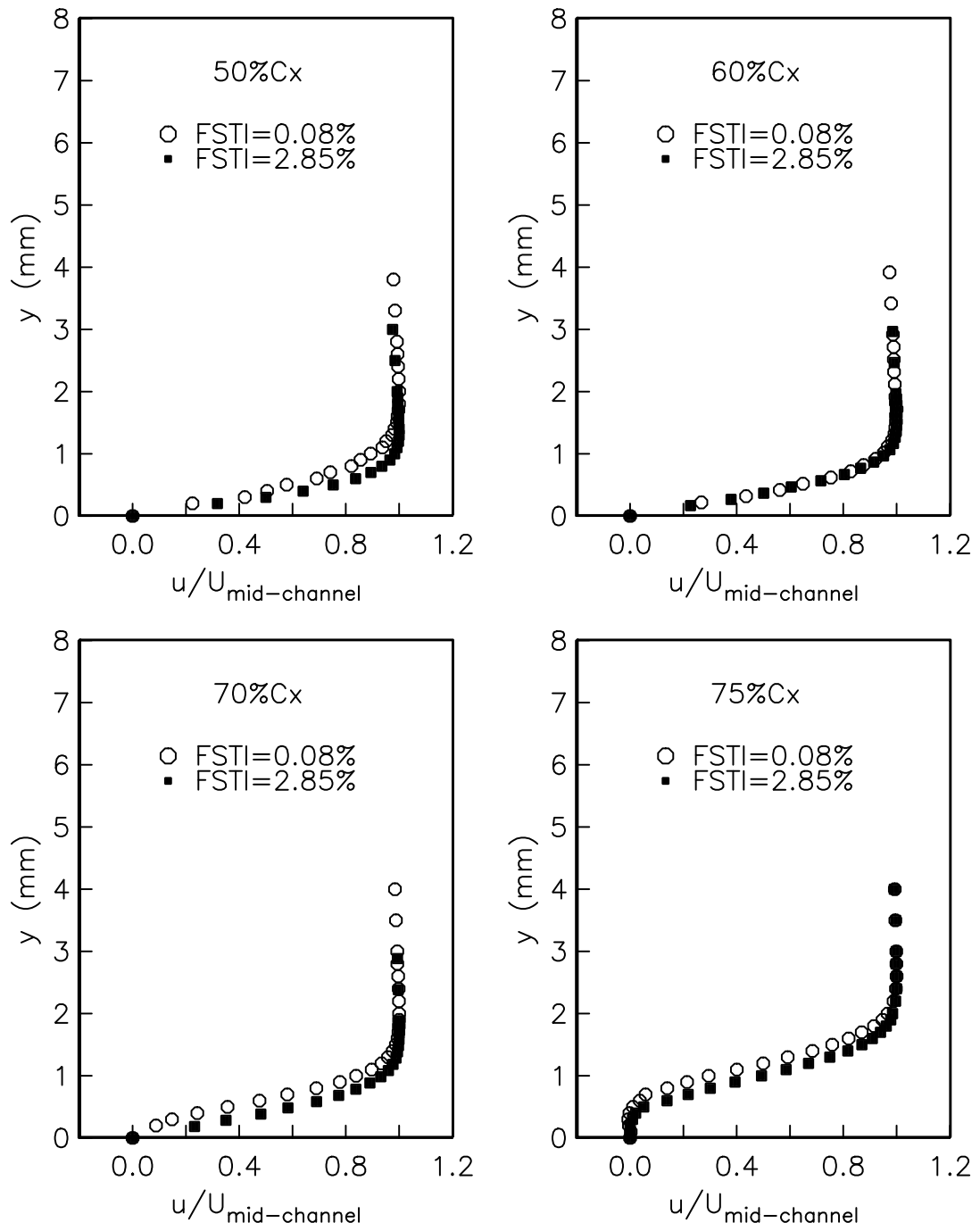
Figure 3.12.   The comparison of the boundary layer profiles for two different freestream turbulence intensities at $Re_c = 50,000$.
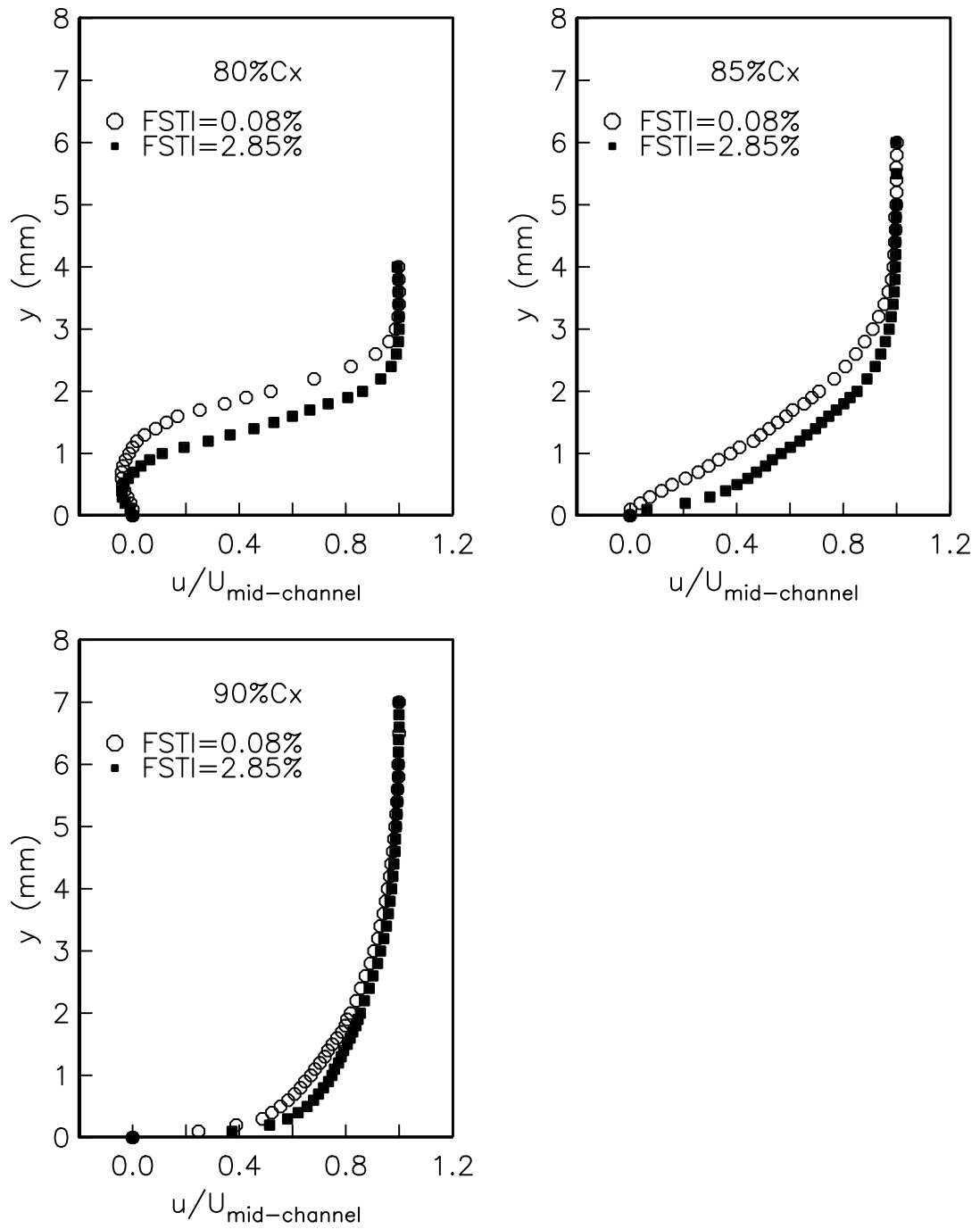
Figure 3.12 (continued). The comparison of the boundary layer profiles for two different freestream turbulence intensities at $Re_c = 50,000$.
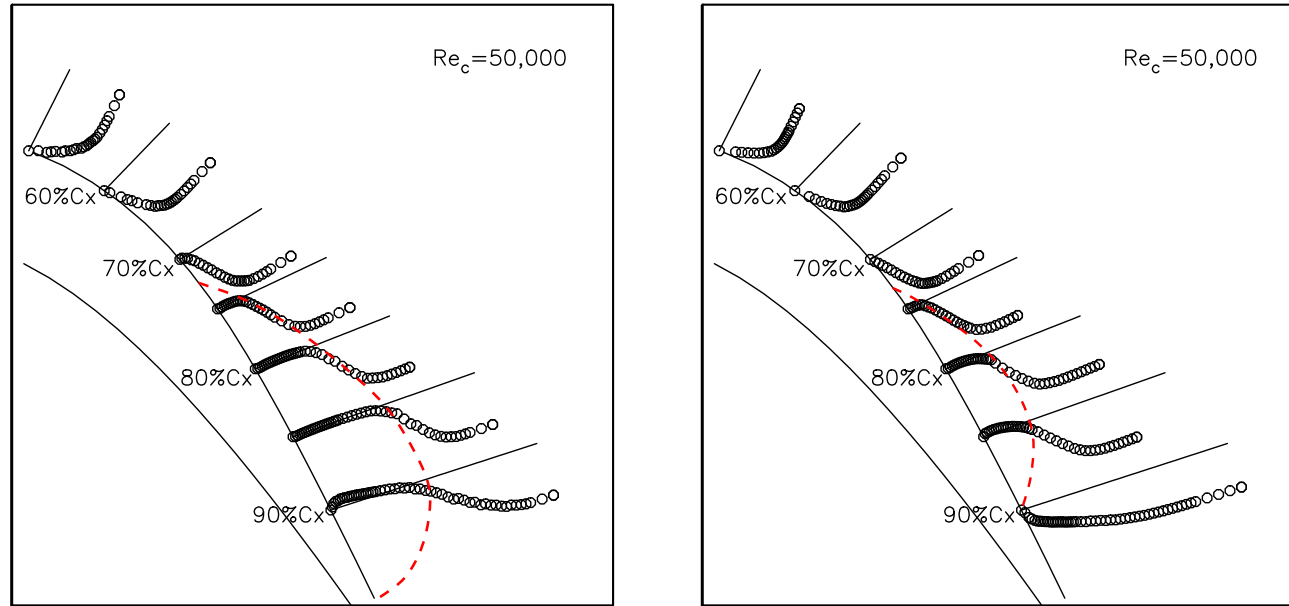
Figure 3.13. The boundary layer profiles on "PakB" blades for two different freestream turbulence intensities at $Re_c = 50,000$ (left: FSTI=0.08%, right: FSTI=2.85%). The separation bubble is smaller for the lower turbulence intensity.

3.3 Summary of Baseline Conditions

Based on the pressure distributions and the boundary layer profiles, the separation and reattachment locations on the suction side of the blade were compiled as in Figure 3.3, to include the effects of both the Reynolds number and the freestream turbulence intensity. This is shown as a 3-D plot in Figure 3.14. These results include the full range of Reynolds numbers from 10,000 to 100,000, for the three turbulence intensities, 0.08%, 1.60%, and 2.85%.
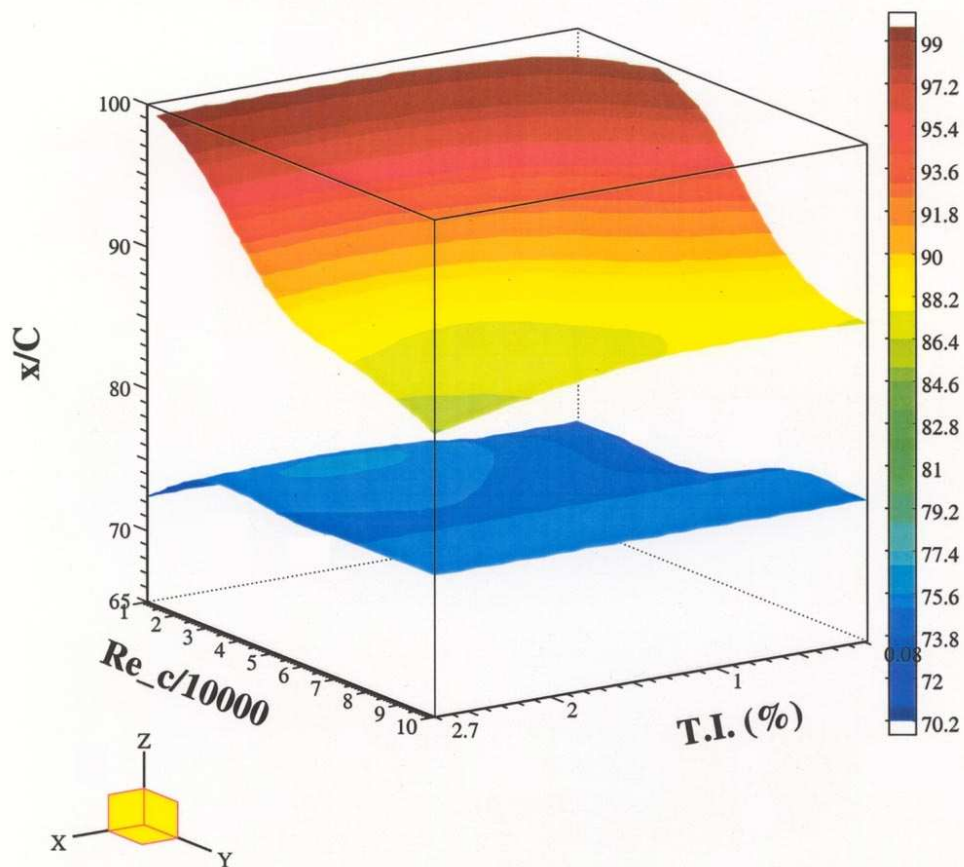
Figure 3.14. Combined effect of chord Reynolds number and freestream turbulence level on the separation (bottom surface) and reattachment (top surface) locations on the suction side of the "PakB" blade.

The lower surface in the plot corresponds to the separation locations. In general, these tend to be relatively insensitive to the freestream conditions, especially compared to the reattachment location, which corresponds to the upper surface. This is an important result. For most effective active flow control the actuator needs to be placed slightly upstream of the separation location. Since the separation location is relatively fixed for all the conditions, only a single actuator, at one location is required.

At the lowest turbulence intensity (0.08%), the flow does not reattach under two lowest Reynolds numbers. For the three higher Reynolds numbers, there are separation bubbles existing on the suction side of the "PakB" blade. As the Reynolds number increases, the size of the separation bubble decreases. Higher turbulence intensities result in smaller separation bubbles, and the effect seems to be more pronounced at lower Reynolds numbers. However even for the highest turbulence intensity and Reynolds number, a separation bubble still remained.

CHAPTER 4

SEPARATION CONTROL – VORTEX GENERATORS

4.1 Vortex Generators

Streamwise vortex generators were found to be effective for separation control on cascade blades. Therefore this approach was investigated in order to provide a basis for comparison to the plasma actuators.

The vortex generators consisted of brass shim material that was bent in a 90° angle. They were placed upstream of the separation line, at $x/C_x = 40\%$, along the span of the blade. The total height of the generators was approximately 50% greater than the local boundary layer thickness. Two spanwise spacings were investigated: 0.5 and 1.0 in (1.27 and 2.54 cm). These corresponded to from 12 to 24 boundary layer thicknesses, which was comparable to the dimple spacing used by Lake et al. [16]. A photograph of the vortex generators on the center blade is shown in Figure 4.1.

4.2 Separation Control Using Vortex Generators

The results were first documented in the blade pressure distributions for the Reynolds number ranging from $10,000$ to $100,000$ at the lowest freestream turbulence intensity (0.08%). These are shown for the two spacings in Figure 4.2 and 4.3.

The results for the 0.5 in (1.27 cm) spacing are shown in Figure 4.2. Focusing on the suction side, the "sawtooth" variation at $x/C_x = 40\%$ is due to the vortex
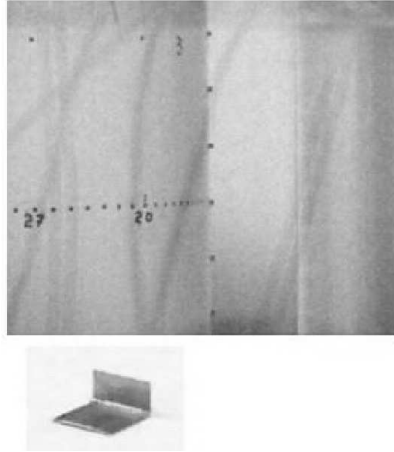
Figure 4.1. Photograph of vortex generator "tabs" on the center blade in cascade, and an individual vortex generator.
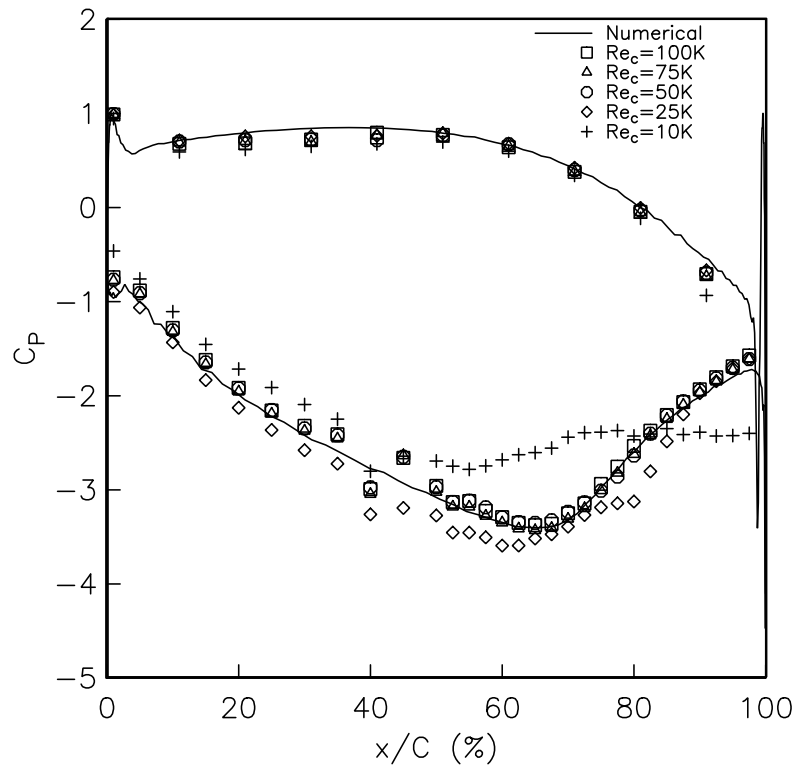
Figure 4.2. Blade pressure distributions with 0.5 in (1.27 cm) spacing of vortex generators for different Reynolds numbers at the lowest freestream turbulence intensity (0.08%).

generators which partially obstruct the pressure taps at that location. Comparing the results to those in Figure 3.1 (without vortex generators) indicates that for $Re_c \geqslant 50,000$, the vortex generators eliminated the flow separation. This is evident by the overlap of these C_p distributions with the Euler distribution. The vortex generators also substantially reduced the extent of the separation region at $Re_c = 25,000$, but did not eliminate it. It had a minimal effect at the lowest Reynolds number.
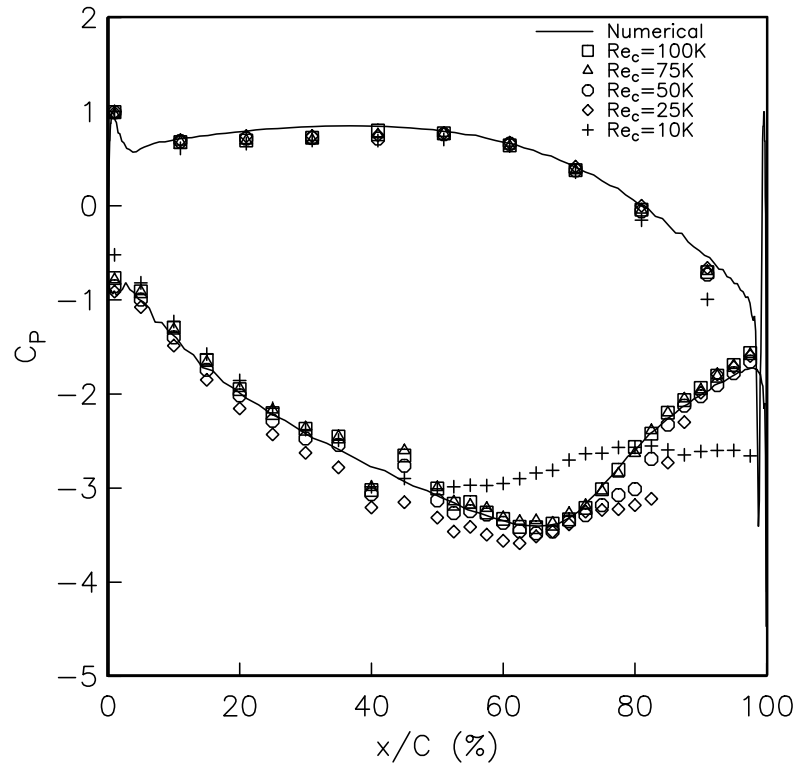
Figure 4.3. Blade pressure distributions with 1.0 in (2.54 cm) spacing of vortex generators for different Reynolds numbers at the lowest freestream turbulence intensity (0.08%).

The results for the larger (1.0 in or 2.54 cm) spacing are shown in Figure 4.3. It is apparent from these C_p distributions that the larger spacing was not as effective. In particular a separation zone is visible for $Re_c = 50,000$, where for the smaller

spacing, based on the C_p distribution, the flow was fully attached.

Vortex generators such as these tabs or bumps, produce a drag penalty when they are not needed. The potential of the plasma actuators is that they can be made flush to the surface, and only operated when necessary, to eliminate any parasitic drag when not in use.

CHAPTER 5

SEPARATION CONTROL – STEADY PLASMA ACTUATORS

5.1 Review of Plasma Actuators

A plasma actuator consists of two electrodes divided by a dielectric layer (see Section 2.7 for details). When the plasma actuator is applied to the "PakB" blades to control the flow separation, its configuration has to be carefully considered to get the optimum control effect. Figure 5.1 shows a photograph of a plasma actuator that would produce a steady two-dimensional wall jet to energize the flow.
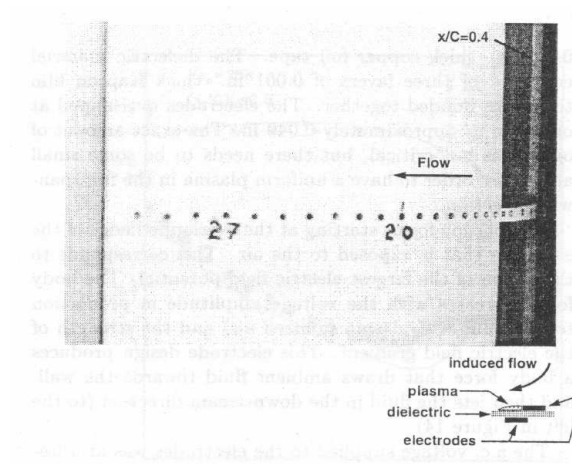
Figure 5.1. Photograph of a plasma actuator located at $x/C_x = 40\%$ on the "PakB" blade with pressure taps.

The actuator spanned most of the length of the center blade in the cascade. The electrodes and the dielectric layer can be seen in the schematic in Figure 5.1.

88

This sandwich arrangement of the actuator is bonded to the blade surface. The electrodes consisted of 0.625 in (1.588 cm) wide, 0.001 in (0.0254 mm) thick copper foil tape. The dielectric material consisted of two layers of 0.005 in (0.127 mm) thick kapton film that were bonded together. The electrodes overlapped at one edge by approximately 0.040 in (1.016 mm). The exact amount of overlap is not critical, but there needs to be some small amount in order to have a uniform plasma in the full spanwise direction.

The plasma forms starting at the overlapped edge of the electrode that is exposed to the air. This corresponds to the region of the largest electric field potential. The body force generated by the actuator can be calculated using Equation 2.1. The body force increases with the voltage amplitude in proportion to the volume of plasma (ionized air) and the strength of the electric field gradient. This electrode design produces a body force that draws ambient fluid toward the wall, and then jets the fluid in the downstream direction (to the left in Figure 5.1). The a.c. voltage supplied to the electrodes was at a frequency of 5000 Hz. This was selected primarily on electronic considerations. With regard to the flow, the effect can be considered to be steady, e.g., a steady wall jet.

5.2 Steady Plasma Actuators Optimization

To improve the effectiveness of the plasma actuators on separation control, some tests were conducted to optimize the configurations of the plasma actuators.

The method of optimization was to measure the blade pressure distributions when different configurations of the plasma actuators were applied to "PakB" blades. The measured pressure distributions were then compared to the Euler computational results to see how well they matched. The better the measured pressure distribution matched the Euler simulation, the more effective the plasma actuator was. The

optimization was implemented using kapton-based plasma actuators.

The major considerations in optimization included the number of the actuators, the location of the actuators, and the orientation of the electrodes. A complete optimization test matrix can be found in Table 2.8 in Chapter 2. For the sake of convenience, it is copied here as Table 5.1. All of the results to be presented were obtained at the lowest freestream turbulence intensity condition (FSTI=0.08%).

TABLE 5.1

OPTIMIZATION MATRIX FOR STEADY PLASMA ACTUATORS

Case No.	Single or Dual?	Location of First PA	Location of Second PA	Configuration
1	Single	40% Cx	N/A	Wall Jet
2	Single	60% Cx	N/A	Wall Jet
3	Single	67.5% Cx	N/A	Wall Jet
4	Single	67.5% Cx	N/A	Spanwise Vortex
5	Single	67.5% Cx	N/A	Wall Jet & Spanwise Vortex
6	Single	72.5% Cx	N/A	Wall Jet
7	Dual	67.5% Cx	75% Cx	Wall Jet
8	Dual	67.5% Cx	77.5% Cx	Wall Jet
9	Dual	67.5% Cx	85% Cx	Wall Jet

5.2.1 The Location of the Plasma Actuator

The first step is to examine the effect of the location of the plasma actuators on the separation control. The pressure distributions for one steady plasma actuators located at different streamwise locations (Case 1, 2, 3, and 6 in Table 5.1) are shown in Figure 5.2 at $Re_c = 50,000$. In order to compare the effect of the separation control, the Euler simulation results and the pressure distribution for the uncontrolled case are also plotted in this figure.

From Figure 5.2, it can be seen that no matter where the plasma actuator was
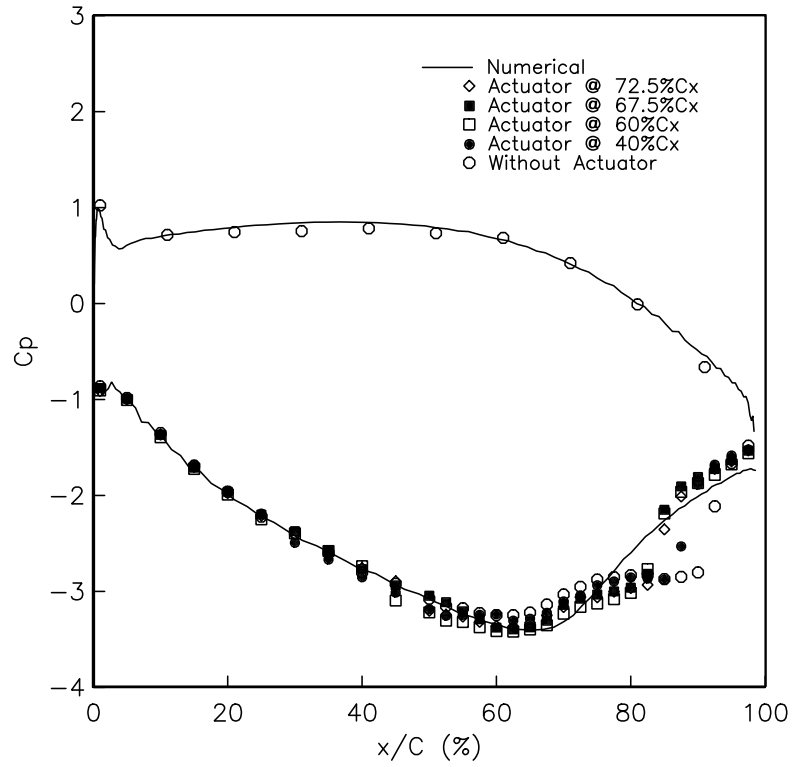
Figure 5.2. Pressure distributions on the "PakB" blade for single steady plasma actuator located at different streamwise locations at $Re_c = 50,000$. The actuator voltage amplitude was 8 kV for all the cases.

located, the size of the separation bubble was reduced when the actuator was operated. However, the separation location was very insensitive to the location of the plasma actuator and only the reattachment location was affected by the plasma actuator. For the uncontrolled case, the flow separates at $x/C_x = 72.5\%$ and reattaches at $x/C_x = 97.5\%$. When the actuator was located at $x/C_x = 40\%$, the flow separates at $x/C_x = 72.5\%$ and reattaches at $x/C_x = 90\%$. When the actuator was located at $x/C_x = 60\%$ and $x/C_x = 67.5\%$, the flow separates at $x/C_x = 72.5\%$ and reattaches at $x/C_x = 85\%$. There is not much difference between these two cases. When the actuator was located at $x/C_x = 72.5\%$, the flow separation still occurs at $x/C_x = 72.5\%$ but the reattachment location moved a little downstream to $x/C_x = 87.5\%$. Figure 5.3 shows the effect of the location of the plasma actuators on the locations of separation and reattachment.
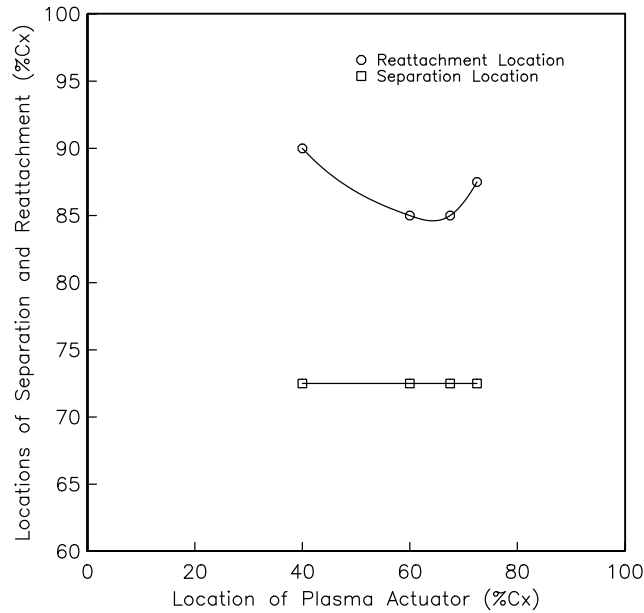
Figure 5.3. The locations of separation and reattachment as a function of the location of single steady plasma actuator. The Reynolds number was $50,000$ and the amplitude of the actuator voltage level was 8 kV.

Figure 5.3 indicates that the optimum location for the plasma actuator is $x/C_x \approx$ 65%. This is consistent with the results from other research that the separation control is the most effective when applied slightly before the separation location. In my case, the separation occurs at $x/C_x = 72.5\%$, thus the actuator worked the best when located around $x/C_x = 67.5\%$.

5.2.2 The Number of the Plasma Actuators

The second consideration of the optimization is to see if any benefit can be obtained by adding another plasma actuator to the "PakB" blade. Since a single plasma actuator was the most effective when located at $x/C_x = 67.5\%$, one of the two actuators was kept at this streamwise location in this test. The location of the other actuator was varied from $x/C_x = 75\%$ to $x/C_x = 85\%$, which are corresponding to Case No.7, No.8, and No.9 in Table 5.1.

The blade pressure distributions for these three cases are shown in Figure 5.4. To see how the second actuator works, the pressure distribution for a single plasma actuator located at $x/C_x = 67.5\%$ is plotted in this figure too. The pressure distributions for three dual actuator cases collapse to one another in Figure 5.4, which indicates the location of the second actuator has no effect on the pressure distribution. For all dual actuator cases, the location of separation is located at $x/C_x = 72.5\%$ and the location of reattachment was improved from $x/C_x = 97.5\%$ (uncontrolled case) to $x/C_x = 87.5\%$. However, comparing to the results of a single plasma actuator, I found that no benefit was obtained from the second plasma actuator.

5.2.3 The Orientation of the Electrodes

A plasma actuator can generate wall jets, spanwise vortices, and streamwise vortices, depending on the orientation of the electrodes, as illustrated in Figure 2.26. In this research work, actuator configurations generating wall jets and spanwise
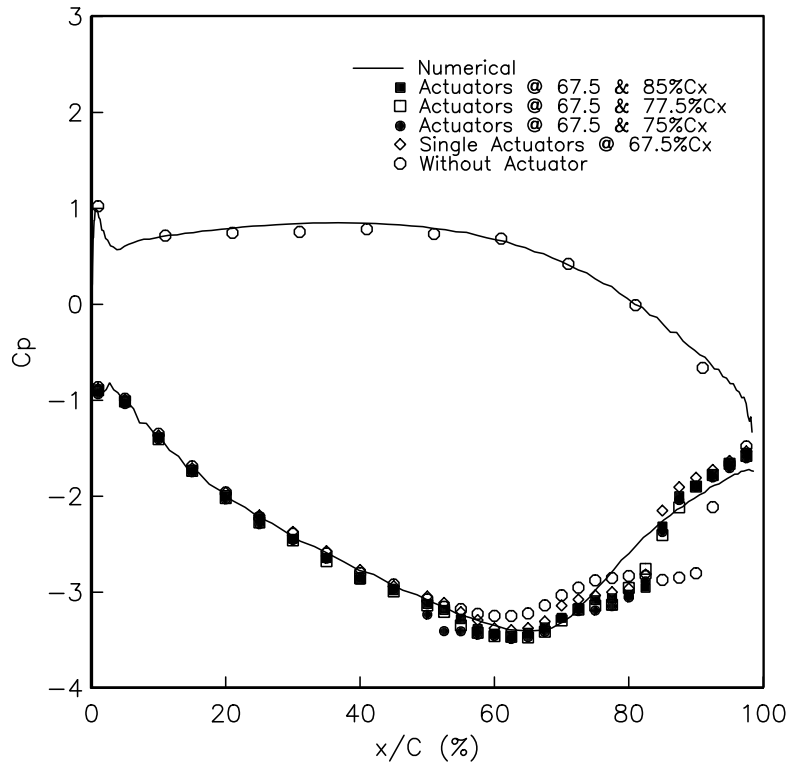
Figure 5.4. Pressure distributions on the "PakB" blade for dual steady plasma actuators ($Re_c = 50,000$). The first actuator was kept at $x/C_x = 67.5\%$ and the location of the second actuator was varied from $x/C_x = 75\%$ to 85%. The actuator amplitude was 8 kV for both actuators.

vortices were tested. The configuration generating streamwise vortices was not tested because of the difficulty in making good streamwise actuator arrays. Single plasma actuator was used and located at $x/C_x = 67.5\%$ for all the tests. These tests are corresponding to Case No.3, No.4, and No.5 in Table 5.1.

Figure 5.5 shows the blade pressure distributions for a wall jet actuator, a spanwise vortex actuator, and a combination of a wall jet and a spanwise vortex actuators at $Re_c = 50,000$. Regarding the location of reattachment, all three configurations worked almost the same. The reattachment location of the flow was improved from $x/C_x = 97.5\%$ (uncontrolled case) to $x/C_x = 87.5\%$. This indicates that the mechanism of the steady plasma actuator is tripping. The mechanism of the plasma actuator will be discussed in more detail later.
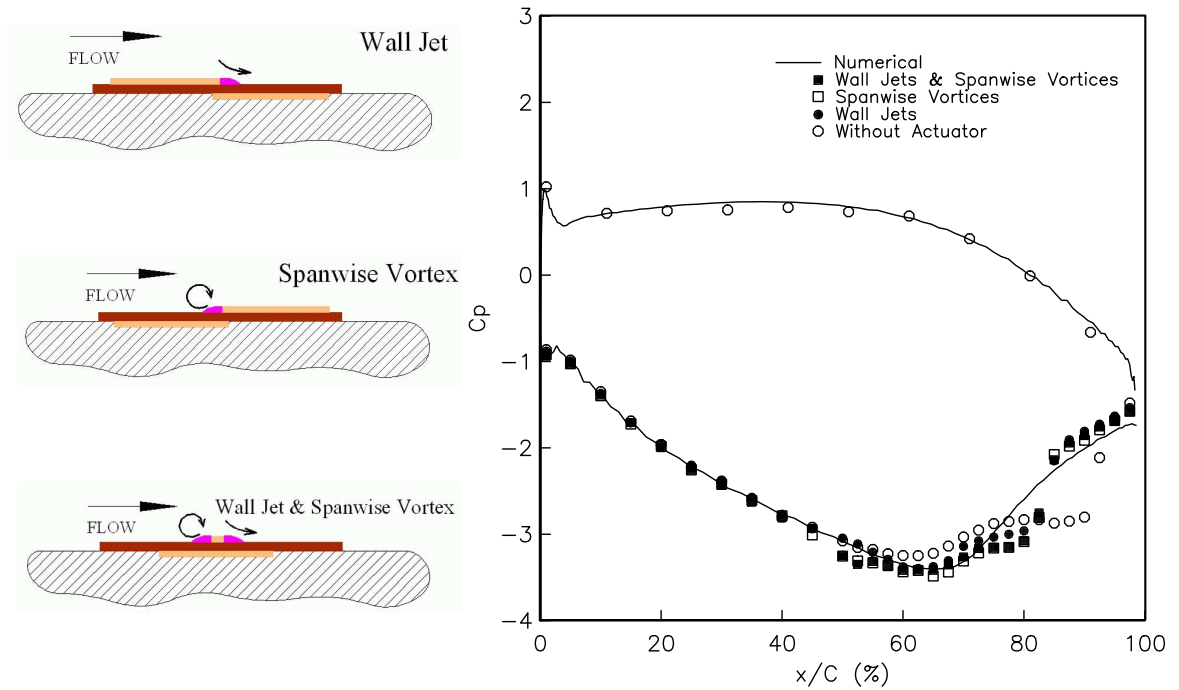
Figure 5.5. Pressure distributions on the "PakB" blade for single steady plasma actuator located at $x/C_x = 67.5\%$ with different electrode orientations ($Re_c = 50,000$). The actuator amplitude was 8 kV for all the cases.

95

5.3 The Effect of the Actuator Voltage Level

Based on the optimization results, a single steady plasma actuator was chosen to be located at $x/C_x = 67.5\%$ and to generate steady two-dimensional wall jets. The a.c. voltage level needed to locally ionize the air, and control reattachment was investigated as part of this effort. This is mainly a function of the actuator design (electrode arrangement and dielectric properties).

Figure 5.6 documents the blade pressure coefficient distributions on the suction side for different actuator levels with the actuator at $x/C_x = 67.5\%$. This position is slightly upstream the separation location which occurs at $x/C_x = 72.5\%$.
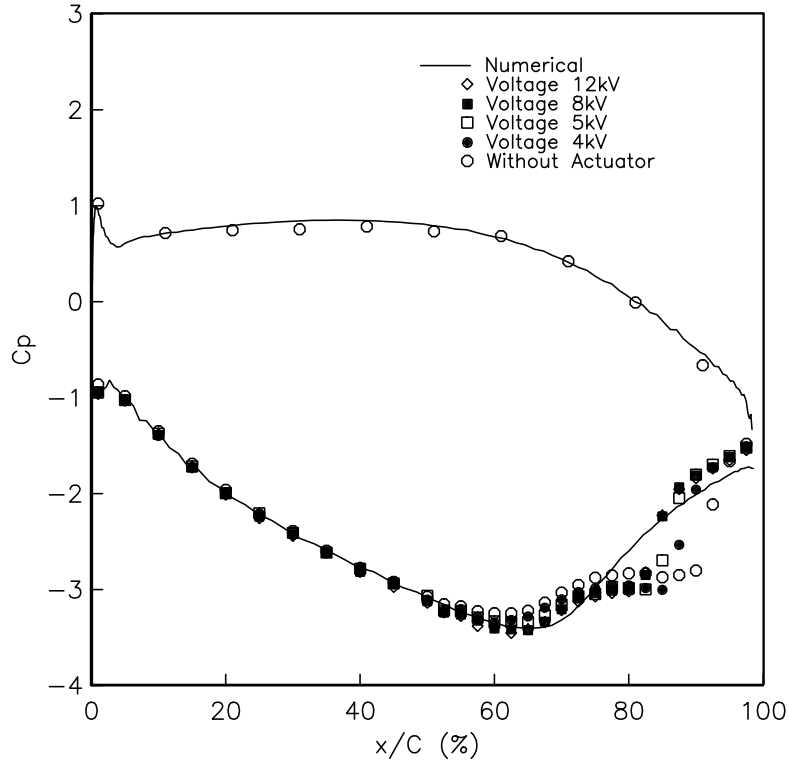
Figure 5.6. Blade pressure distributions with a single steady plasma actuator at $67.5\%C_x$, for different actuation levels at $Re_c = 50,000$.

In Figure 5.6, the open circles indicate the C_p distribution without the actuator.

For this Re_c, the flow reattaches at $x/C_x \approx 97.5\%$. Increasing the actuator level moves the point of reattachment upstream. At the largest amplitude, the point of reattachment is $x/C_x \approx 85\%$.

From the pressure distributions shown in Figure 5.6, I noticed that there is a threshold voltage level for the actuator to take effect. When the actuator level was less than this threshold value, the actuator had no effect on the flow. As the actuator level was increased to be greater than this threshold value, the actuator started to improve the location of reattachment, thus decrease the size of the separation bubble. However, there is saturation in the effect of the actuator levels. When the actuator level is greater than 8 kV, the location of reattachment could not be further improved.

This phenomenon was also observed when the actuator was located at $x/C_x = 40\%$. Figure 5.7 documents the blade pressure distributions on the suction side for different actuator levels with the actuator at $x/C_x = 40\%$. This position is well upstream the separation location, thus the actuator was not as effective as when located at $x/C_x = 67.5\%$. However, the threshold value in the actuator level still exists in this case. There is also saturation in the effect of the actuator levels. These results are summarized in Figure 5.8. This shows the reattachment location as a function of the actuator amplitude for the two x/C_x actuator locations at $Re_c = 50,000$.

The effectiveness of the plasma actuator was also investigated at lower $Re_c = 25,000$. As was shown in Figure 3.1, the flow never reattaches at this Reynolds number in the low disturbance condition. Therefore there are significant gains that can come from separation control. The C_p distributions for different actuation levels, with the actuator at $x/C_x = 67.5\%$, are shown in Figure 5.9. At this Reynolds number, flow reattachment is observed, with a systematic reduction in the length
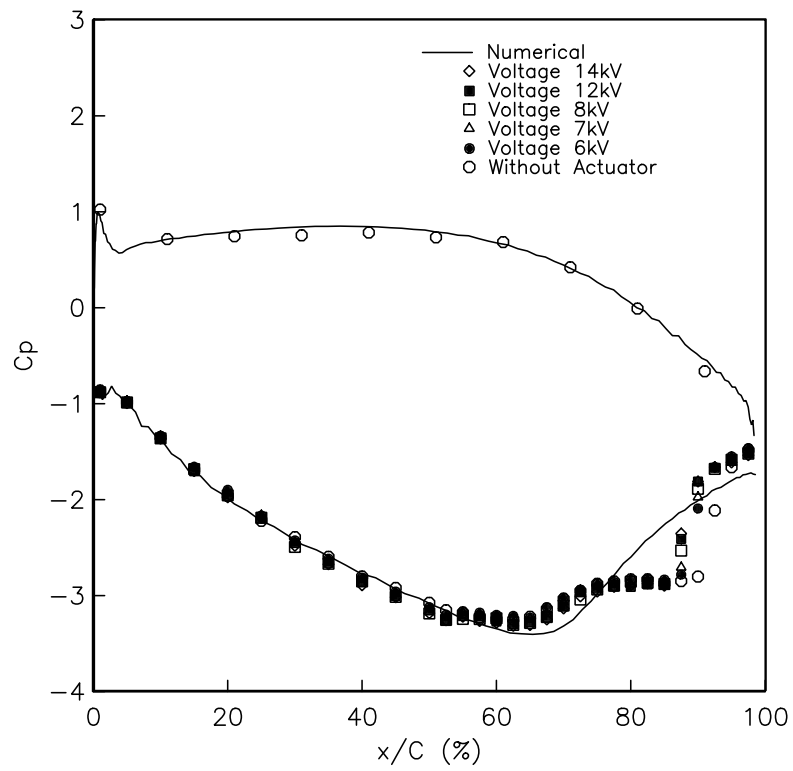
Figure 5.7. Blade pressure coefficient distribution with a single steady plasma actuator at $40\%C_x$, for different actuation levels at $Re_c = 50,000$.
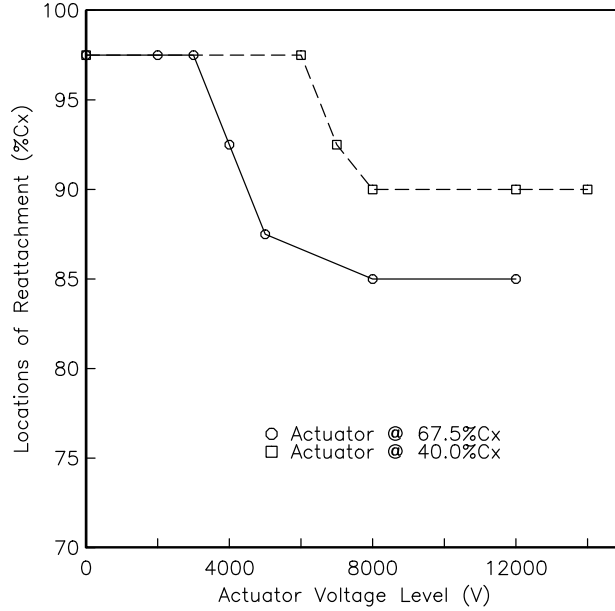
Figure 5.8. Effect of steady plasma actuator amplitude on reattachment location for two actuator positions ($Re_c = 50,000$).

of the separation region with increasing actuator amplitude.

5.4   Boundary Layer Profiles

The boundary layer profiles were also measured using LDV to examine the effect of the plasma actuators. The boundary layer profiles for $Re_c = 50,000$ for both uncontrolled and controlled case are shown in Figure 5.10.

At $x/C_x = 50\%$, the boundary layer profiles for both uncontrolled and controlled case do not collapse to each other. This discrepancy was caused by the presence of the leading edge of the kapton film, which was virtually a tiny step on the blade surface. Its effect was also seen in the pressure distributions. The flow remains attached at both $x/C_x = 60\%$ and 70% and the measured boundary layer profiles collapse to each other at these two streamwise locations.

The flow is separated at $x/C_x = 75\%$ for both uncontrolled and controlled cases.
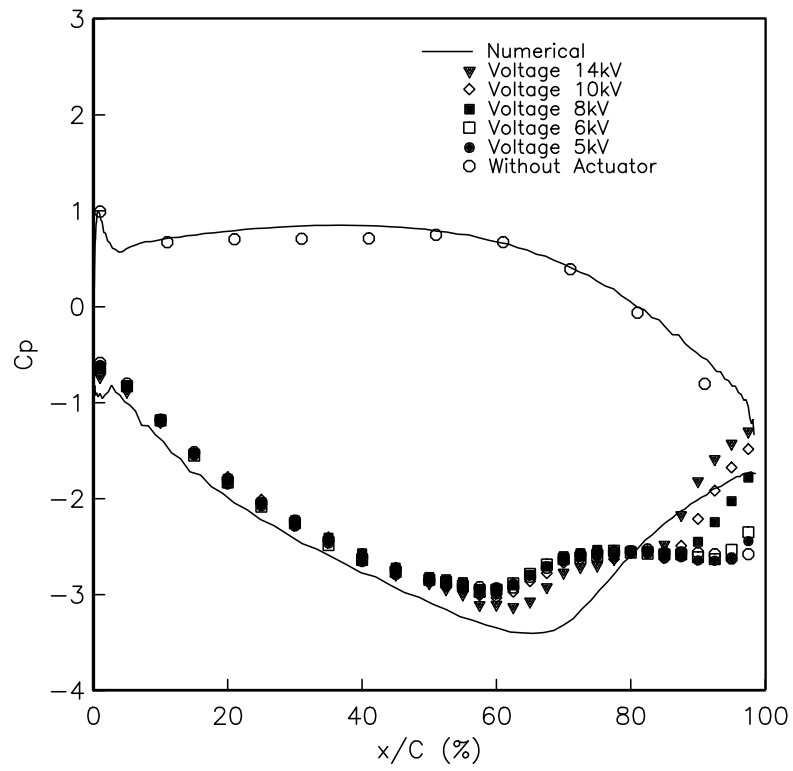
Figure 5.9. Blade pressure coefficient distributions with a single steady plasma actuator at $x/C_x = 67.5\%$, for different actuation levels at $Re_c = 25,000$.
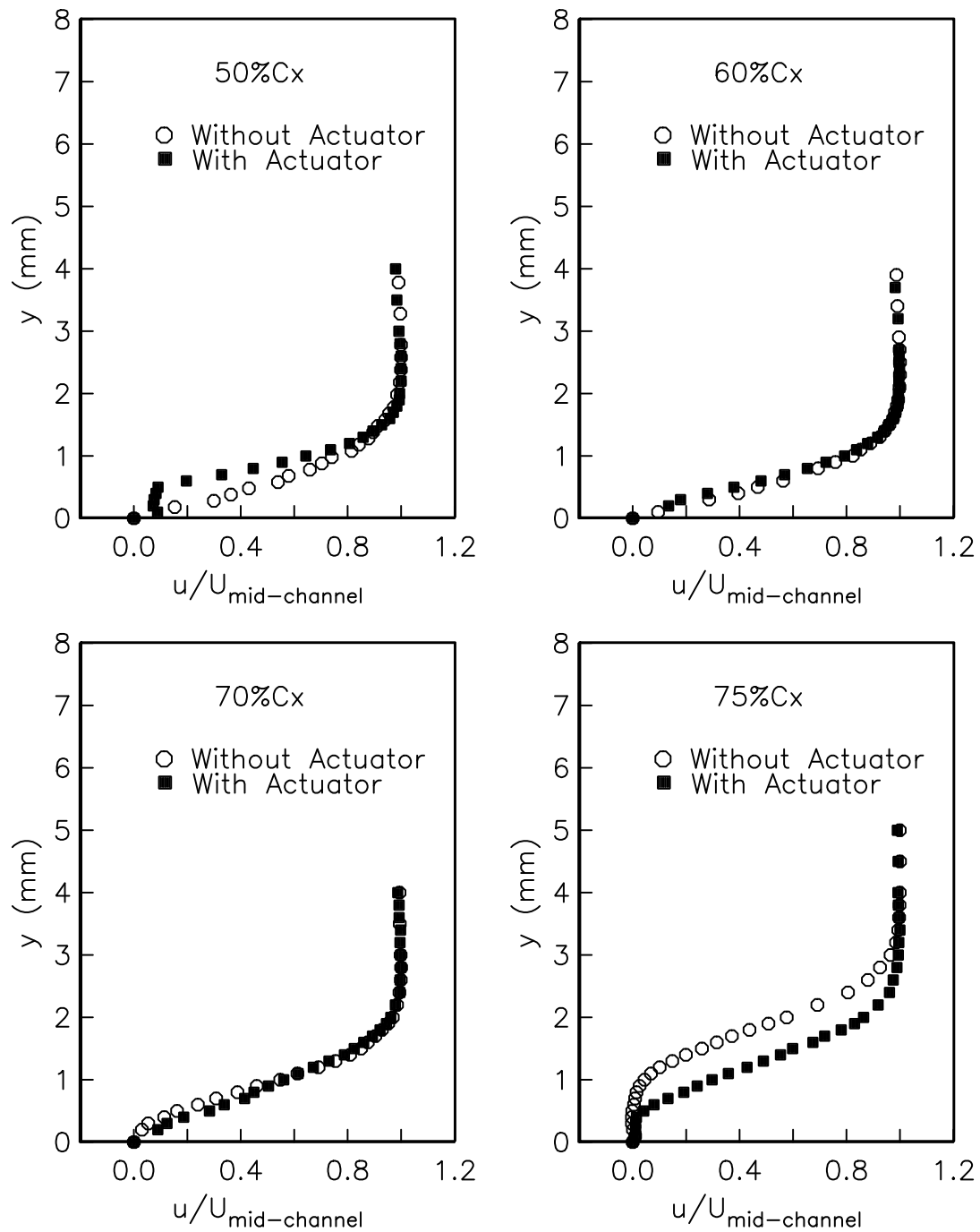
Figure 5.10. The comparison of the boundary layer profiles for uncontrolled and controlled case at $Re_c = 50,000$. For the controlled case, a single steady plasma actuator was located at $x/C_x = 67.5\%$ and operated at 8 kV.
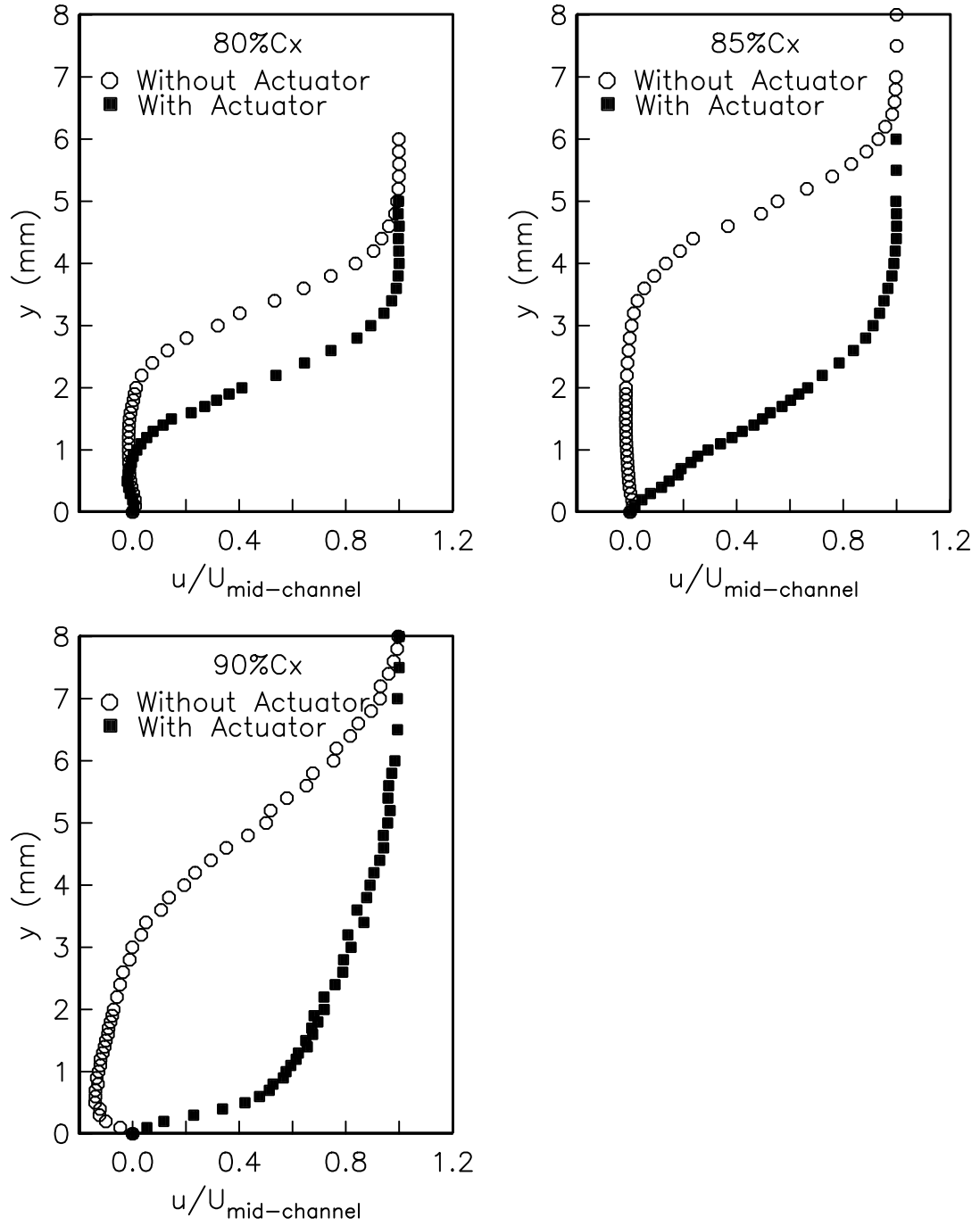
Figure 5.10 (continued). The comparison of the boundary layer profiles for uncontrolled and controlled case at $Re_c = 50,000$. For the controlled case, a single steady plasma actuator was located at $x/C_x = 67.5\%$ and operated at 8 kV.

But the height of the separation bubble for the controlled case is much smaller than that for the uncontrolled case. As the air flows more downstream, it sees a dramatically larger separation region for the uncontrolled case than the controlled case. The flow is already reattached at $x/C_x = 85\%$ for the controlled case while the flow is still separated at $x/C_x = 90\%$ for the uncontrolled case.

The measured boundary layer profiles are plotted on the suction side of the "PakB" blade, which is shown in Figure 5.11. The effect of the plasma actuator can be clearly seen from the size of separation bubbles.
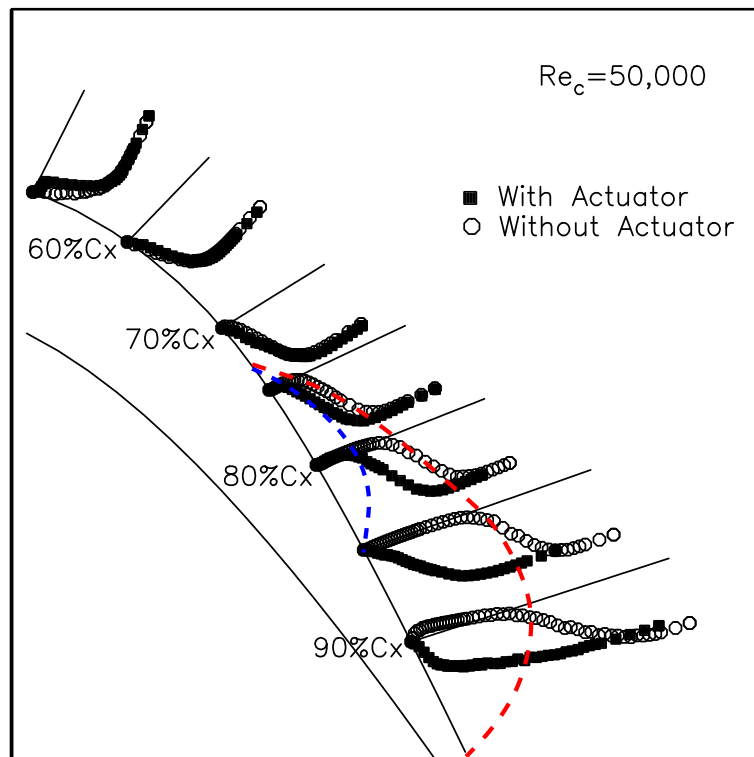
Figure 5.11. The boundary layer profiles on "PakB" blade for uncontrolled and controlled case at $Re_c = 50,000$. For the controlled case, a single steady plasma actuator was located at $x/C_x = 67.5\%$ and operated at 8 kV. The separation bubbles are sketched using dashed lines. The larger separation bubble for the uncontrolled case is reduced to the smaller one when the plasma actuator is operated.

5.5 Flow Visualization

Flow visualizations were performed to give direct observations of separation control using plasma actuators. Figure 5.12 shows two frames taken from the flow videos for $Re_c = 25,000$. The picture on the left shows the flow for the uncontrolled case. The flow separation is clearly seen in this photo. The particle streams could not follow the blade surface and detaches from it at $x/C_x \approx 70\%$. The flow does not reattach to the blade surface at this Reynolds number. Therefore what is seen here is an open separation region on the suction surface instead of a separation bubble which occurs at higher Reynolds numbers. The picture on the right shows the flow for the controlled case. A single steady plasma actuator was located at $x/C_x = 67.5\%$ and operated at 8 kV for the controlled case. The bright spot in the picture is the plasma generated by the actuator. The particle streams in this picture follow the blade surface very well. The flow is reattached before it leaves the trailing edge of the blade. Although the pressure measurements indicated there is still a small separation bubble on the blade, it is barely seen in the picture.
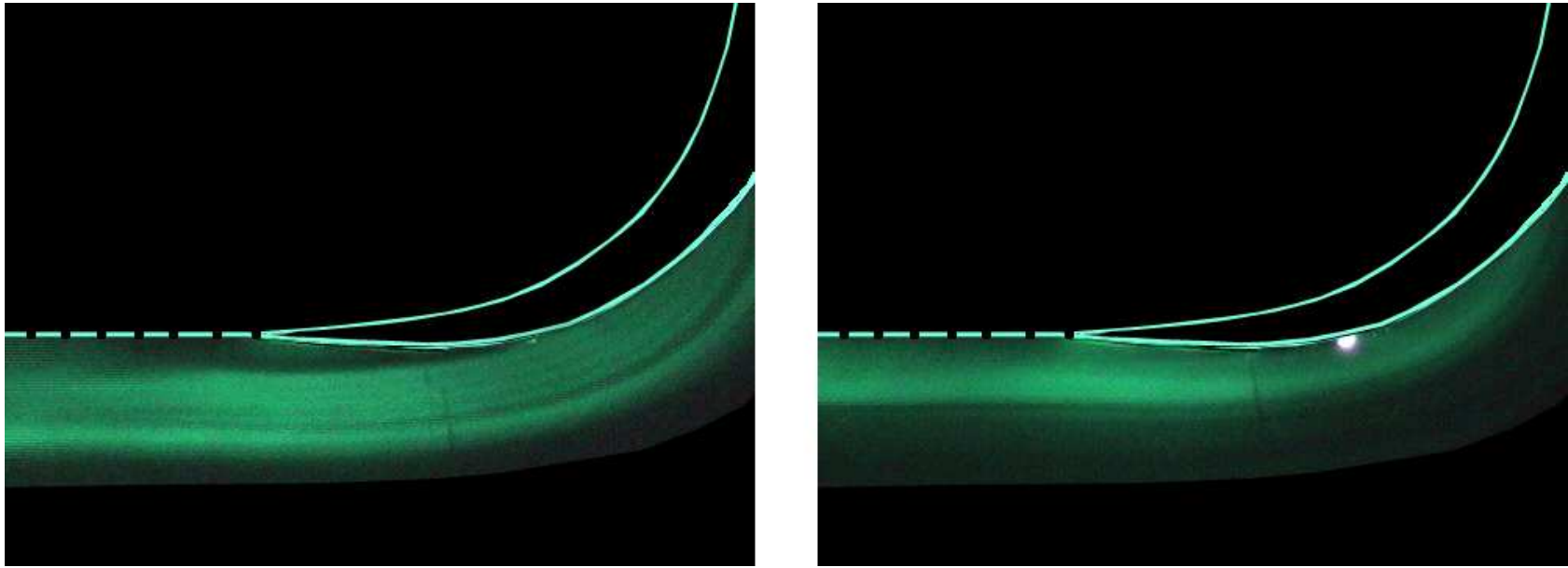
Figure 5.12. The flow field around the "PakB" blade was visualized by combining particle streams and shining laser sheet ($Re_c = 25,000$). The left picture shows the flow for the uncontrolled case. The right picture shows the flow when a steady plasma actuator was operated. The actuator was located at $x/C_x = 67.5\%$ and operated at 8 kV.

5.6 Comparison between Steady Plasma Actuators and Vortex Generators

At this point it is relevant to compare the effect of separation control between the vortex generator tabs and the plasma actuators. This is done by cross-plotting the C_p distributions on the suction side of the blade in the region of separation. Here I consider the two tab spacings ($z/\delta = 12$ and 24), and only the best of the plasma actuator conditions ($x/C_x = 67.5\%$ and actuator amplitude of 8 kV).

The comparison is presented in Figure 5.13 and 5.14 for $Re_c = 25,000$ and 50,000, respectively. Included in these plots are the base condition (without actuation), and the numerical inviscid distribution.
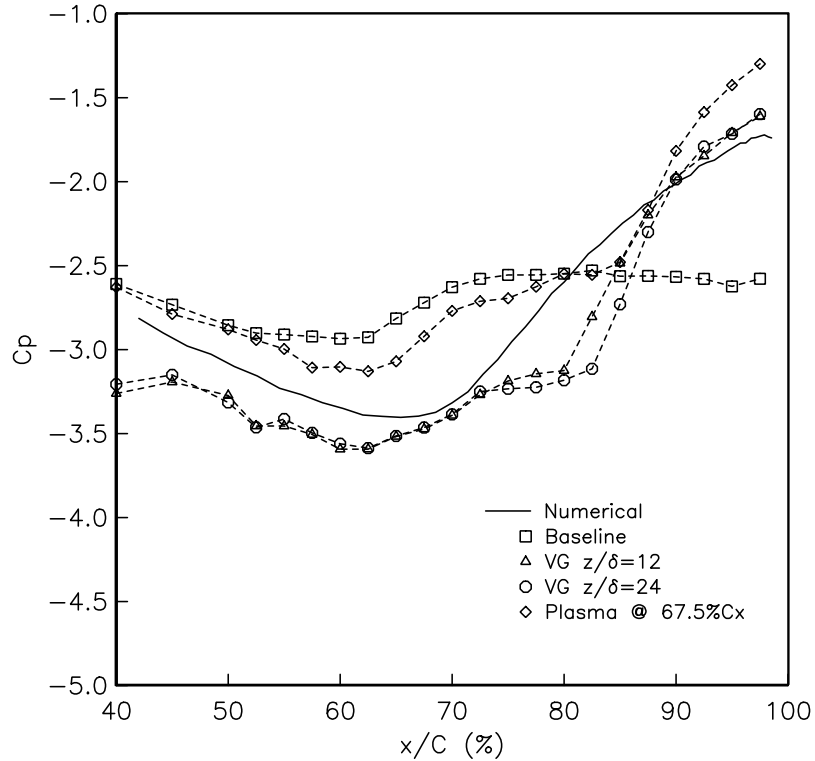
Figure 5.13. Comparison of pressure coefficient distributions in the separation region for vortex generator tabs at two spacings, and a single steady plasma actuator at $x/C_x = 67.5\%$ ($Re_c = 25,000$). The actuator amplitude was 8 kV for the steady plasma actuator.
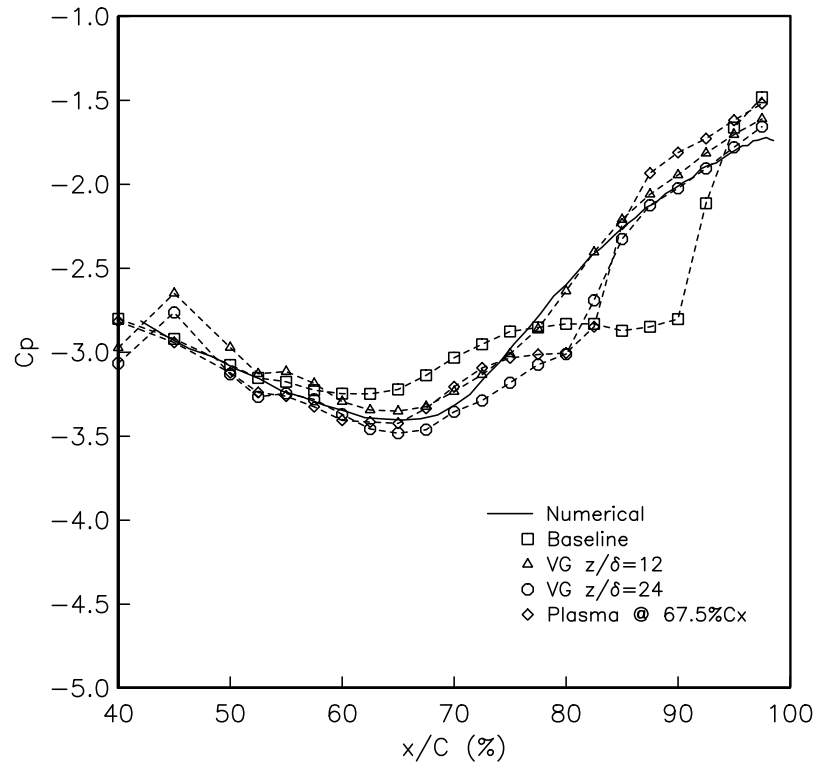
Figure 5.14. Comparison of pressure coefficient distributions in the separation region for vortex generator tabs at two spacings, and a single steady plasma actuator at $x/C_x = 67.5\%$ ($Re_c = 50,000$). The actuator amplitude was 8 kV for the steady plasma actuator.

Focusing on $Re_c = 25,000$ in Figure 5.13, I first note that the C_p distributions for the vortex tabs agree better with the inviscid distribution. This suggests that the boundary layer downstream of the tabs may have higher turbulence levels and is more thoroughly mixed, possibly similar to the effect of roughness. Regardless of this, the location of separation appears to be nearly the same in all the cases. Of the two vortex generator cases, the more closely spaced tabs perform slightly better. The plasma actuator performs as well as the best vortex generator.

At $Re_c = 50,000$, upstream of the flow separation, all of the cases agree reasonably well with the inviscid distribution. Here again, of the two vortex generator configurations, the more closely spaced ($z/\delta = 12$) performed better. The plasma actuator compared best with the performance of the larger-spaced vortex generator, which still significantly reduced the reattachment length. However, vortex generators produce parasitic drag at higher Reynolds number conditions where separation control is not needed.

CHAPTER 6

SEPARATION CONTROL – UNSTEADY PLASMA ACTUATORS

6.1   Unsteady Plasma Actuators

Another objective of this research work is to investigate the control effect of unsteady plasma actuators. Seifert et al. [?, ?, ?] performed experiments on a variety of airfoils over a wide range of Reynolds numbers. Their results indicate that periodic excitation can be used to effectively delay boundary layer separation and reattach separated flows.

In my experiment, the unsteady pulsing is achieved using a specially designed circuit as discussed in Chapter 2 (see Section 2.7.2). The most important parameters of unsteady excitation include the excitation frequency and the plasma duty cycle. Figure 6.1 shows a typical control signal that was sent to a plasma actuator during the unsteady excitation.

In Figure 6.1, $T\_control$ is the time duration of one cycle of the control signal. Only part of the control signal consists of high frequency, high amplitude triangular wave, which will generate plasma along the edge of the exposed electrode of a plasma actuator. The duration of the high frequency, high amplitude triangular wave is denoted as T_signal. The excitation frequency $f_{excitation}$ and the plasma duty cycle β are defined in Equation 6.1 and Equation 6.2, respectively.

$$f_{excitation} = \frac{1}{T\_control}. \tag{6.1}$$

$$\beta = \frac{T\_signal}{T\_control} \times 100\%. \tag{6.2}$$
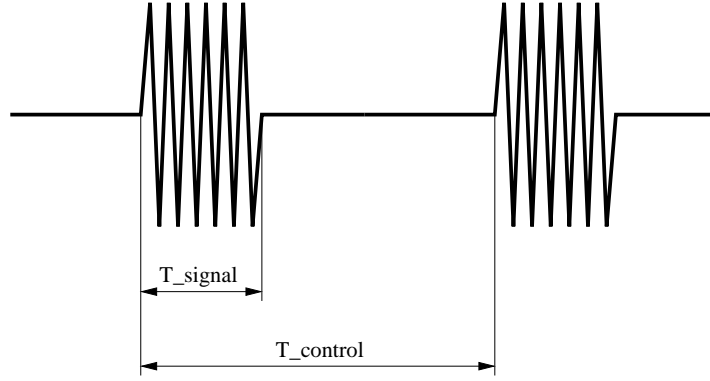
Figure 6.1. The control signal sent to the plasma actuator during unsteady excitation. $T\_control$ is the time duration of one cycle of the control signal. T_signal is the time duration of the high frequency, high amplitude triangular wave.

6.2 Effect of Excitation Frequency

One of the objectives of this research work was to understand how plasma actuators interact with the flow around the "PakB" blades. The excitation frequency was one of the concerns when unsteady plasma actuators were used to control the flow separation. It was argued in other research work that the unsteady pulsing is the most effective when the Strouhal number is equal to unity [2]. The Strouhal number is defined as

$$S_t = \frac{f L_{sep}}{U_{mid-channel}}, \tag{6.3}$$

where S_t is the Strouhal number, f is the excitation frequency, L_{sep} is the length of the separation region, and $U_{mid-channel}$ is the local freestream velocity in the blade passage.

In this research work, $U_{mid-channel} \approx 9.4$ m/s for $Re_c = 50,000$. According to the blade pressure distribution, the separation region at $Re_c = 50,000$ is from $x/C_x = 72.5\%$ to 97.5%. The corresponding length of separation region on the suction surface is $L_{sep} = 3.25$ in (8.255 cm). The excitation frequency is 114 Hz in

order to make the Strouhal number unity.

Figure 6.2 shows the blade pressure distributions at $Re_c = 50,000$ for different excitation frequencies of the unsteady plasma actuator. The unsteady plasma actuator used for this test was a macor-based actuator. It was located at $x/C_x = 67.5\%$ and the actuator amplitude was 24 kV. The duty cycle of the plasma was 10% for all the cases and the excitation frequency ranged from 10 Hz to 160 Hz. It can be seen that the size of the separation region was reduced significantly when the unsteady plasma actuator was operated. As the excitation frequency increases, the blade pressure distribution for the unsteady plasma actuator collapses more toward the Euler numerical results. The plateau in the blade pressure distribution, which represents the region of separation, almost disappears at high excitation frequencies.

The effect of the excitation frequency can be demonstrated by plotting the pressure deficit at $x/C_x = 85\%$ against the excitation frequency, as shown in Figure 6.3. Note that the excitation frequencies have been converted into the Strouhal numbers in Figure 6.3. Also plotted in this figure is a spline-fit curve through the pressure deficit points.

The pressure deficit is defined as the difference between the experimental results and the numerical result at the selected streamwise location. It indicates how effective the unsteady plasma actuator is. As shown in Figure 6.3, the pressure deficit decreases as the Strouhal number increases, which indicates that the higher excitation frequency works better. However, the pressure deficit curve starts to become flat as the Strouhal number passes 0.9, which corresponds to an excitation frequency of 102 Hz. The pressure deficit curve has a tendency to increase when the Strouhal number is greater than 1.05. This gives a minimum point at the unity Strouhal number. This means the unsteady plasma was the most effective at separation control when the Strouhal number is unity, as mentioned earlier. The corresponding
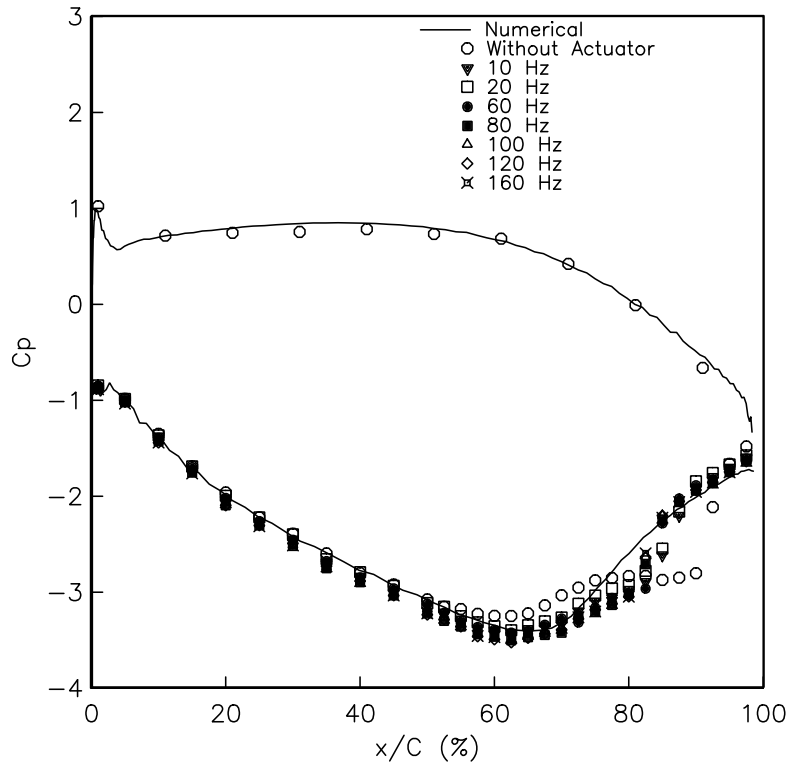
Figure 6.2. Blade pressure distributions at $Re_c = 50,000$ for different excitation frequencies of unsteady plasma actuator. The unsteady plasma actuator was a macor-based actuator. It was located at $x/C_x = 67.5\%$. The actuator amplitude was 24 kV and the plasma duty cycle was 10% for all the cases.
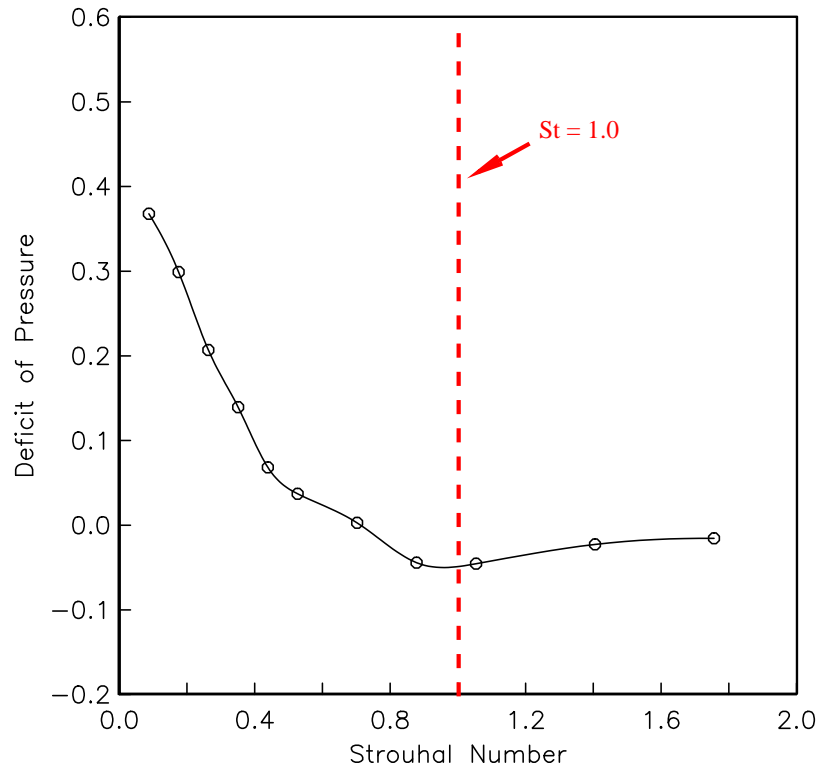
Figure 6.3. Pressure deficit between the experimental results and the numerical result for different excitation frequencies at $x/C_x = 85\%$ for $Re_c = 50,000$. The unsteady plasma actuator was a macor-based actuator. It was located at $x/C_x = 67.5\%$. The actuator amplitude was 24 kV and the plasma duty cycle was 10% for all the cases.

excitation frequency is 114 Hz for $Re_c = 50,000$.

The power spectra of the flow, which will be discussed in detail in the next chapter, show that there is an energy peak around 300 Hz at $x/C_x = 80\%$ and 85%. This frequency is believed to be related to the shear layer instability. I also tested the unsteady plasma actuators with this frequency. The blade pressure distribution for 300 Hz is almost identical to that for 200 Hz, which indicates that the excitation frequency of 114 Hz remains the optimum excitation frequency for $Re_c = 50,000$ and that the mechanism of unsteady plasma actuators is not exciting the separated shear layer instability.

6.3 Effect of Plasma Duty Cycle

Another important parameter during the unsteady pulsing is the plasma duty cycle. The plasma duty cycle is the proportion of the time during which the plasma is generated. In the last section, I discussed the effect of the excitation frequency. The plasma duty cycle was 10% for all the cases. It was found that the unsteady plasma actuators were the most effective when the excitation frequency is between 100 Hz and 120 Hz for $Re_c = 50,000$. Bons et al. [?] studied the effect of the duty cycle when using the pulsed jets to control the turbine blade separation. They found that the unsteady jets were still effective even when a small duty cycle as low as 1% was used.

Figure 6.4 shows the blade pressure distributions at $Re_c = 50,000$ when different plasma duty cycles were used during the unsteady pulsing. The unsteady actuator used for this test was a kapton-based actuator. It was located at $x/C_x = 67.5\%$. The excitation frequency of the unsteady actuator was 40 Hz and the actuator amplitude was 8 kV for all the cases. Although 40 Hz is not the optimum excitation frequency, it produced approximately 80% of the improvement reached by the optimum. It can
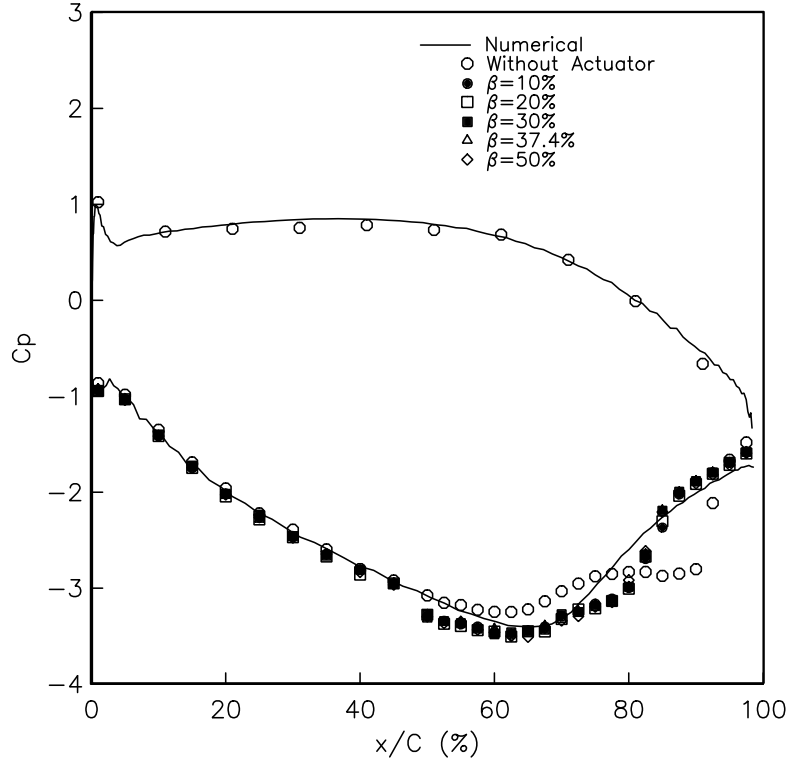
Figure 6.4. Blade pressure distributions at $Re_c = 50,000$ for different plasma duty cycles of unsteady plasma actuator. The unsteady plasma actuator was a kapton-based actuator. It was located at $x/C_x = 67.5\%$. The excitation frequency was 40 Hz and the actuator amplitude was 8 kV for all the cases.

be seen that the blade pressure distributions for five different plasma duty cycles collapse to one another. This indicates that the lowest duty cycle (10% in this research work) is as effective as the highest duty cycle (50% in this research work). This represents a four time reduction in required energy.

6.4   Boundary Layer Profiles

The boundary layer profiles were measured using a hot-wire probe with a specially designed constant-current anemometer (CCA) to examine the effect of the unsteady plasma actuators. The boundary layer profiles for $Re_c = 50,000$ for both uncontrolled and controlled case are shown in Figure 6.5. For the controlled case, a

macor-based plasma actuator was located at $x/C_x = 67.5\%$ and operated at 100 Hz. The actuator amplitude was 24 kV and the plasma duty cycle was 10%.

When measuring the boundary layer profiles, a velocity increase was observed when the hot-wire probe moved very close to the blade surface. This increase was due to the increased heat radiation from the hot-wire to the blade surface and did not reflect the real flow. From the boundary layer profiles, it can be seen that the flow was separated at $x/C_x = 80\%$ for both uncontrolled and controlled cases. But the height of the separation bubble for the controlled case was much smaller than that for the uncontrolled case. As the air flew downstream, the flow reattached to the blade at $x/C_x = 85\%$ for the controlled case while the flow was still separated at $x/C_x = 90\%$ for the uncontrolled case. Therefore the size of the separation bubble was decreased.

6.5   Wake Profiles and Total Pressure Loss Coefficient

The effectiveness of plasma actuators can also be demonstrated by measuring the total pressure loss coefficient across the "PakB" cascade. The total pressure loss coefficient is calculated from the wake profiles and it is defined as

$$\eta = \int \frac{p_{0_{ds}} - p_{0_{us}}}{\frac{1}{2}\rho U_\infty^2} dy, \tag{6.4}$$

where η is the total pressure loss coefficient, $p_{0_{us}}$ is the total pressure upstream the cascade, $p_{0_{ds}}$ is the total pressure downstream the cascade, ρ is the air density, and U_∞ is the freestream velocity measured upstream the cascade.

The wake profiles of the cascade were measured using a total-static pitot probe. Figure 6.6 shows the wake profiles of two consecutive blades for both uncontrolled and controlled cases for $Re_c = 50,000$ measured $50\%C_x$ downstream the center blade. For the controlled case, an unsteady plasma actuator was located at $x/C_x = 67.5\%$ and operated at 40 Hz. The actuator amplitude was 8 kV and the plasma

116
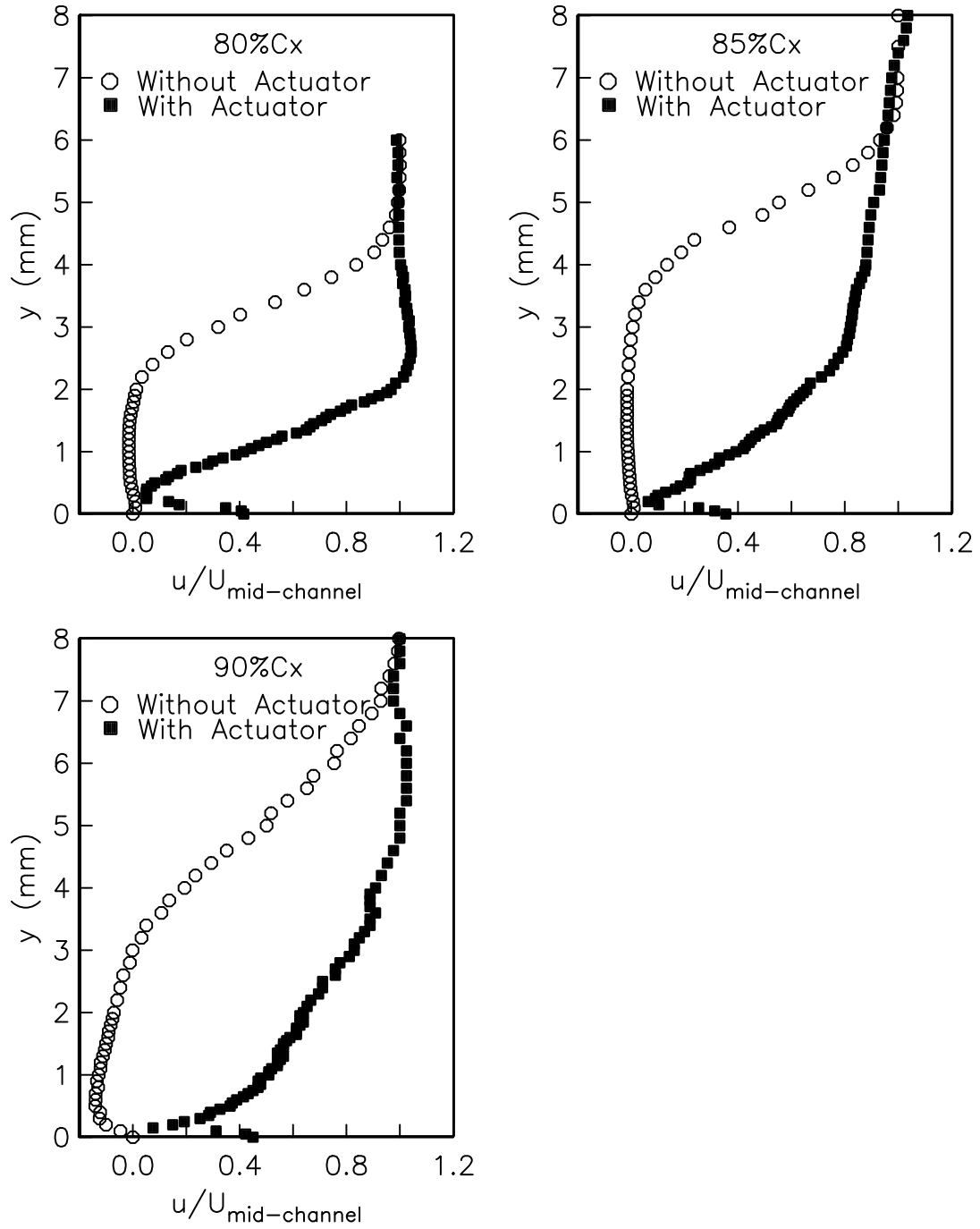
Figure 6.5. The comparison of the boundary layer profiles for uncontrolled and controlled case at $Re_c = 50,000$. For the controlled case, an unsteady plasma actuator was located at $x/C_x = 67.5\%$ and operated at 100 Hz. The actuator amplitude was 24 kV and the plasma duty cycle was 10%.

duty cycle was 10%. The right trough in the figure represents the wake of the center blade and the left trough represents the wake of the blade next to the center blade. The center blade is the one to which separation control was applied using plasma actuators. It can be seen that the wake of the center blade for the controlled case is slightly better than that for the uncontrolled case, which results in only a small improvement in the total pressure loss coefficient.
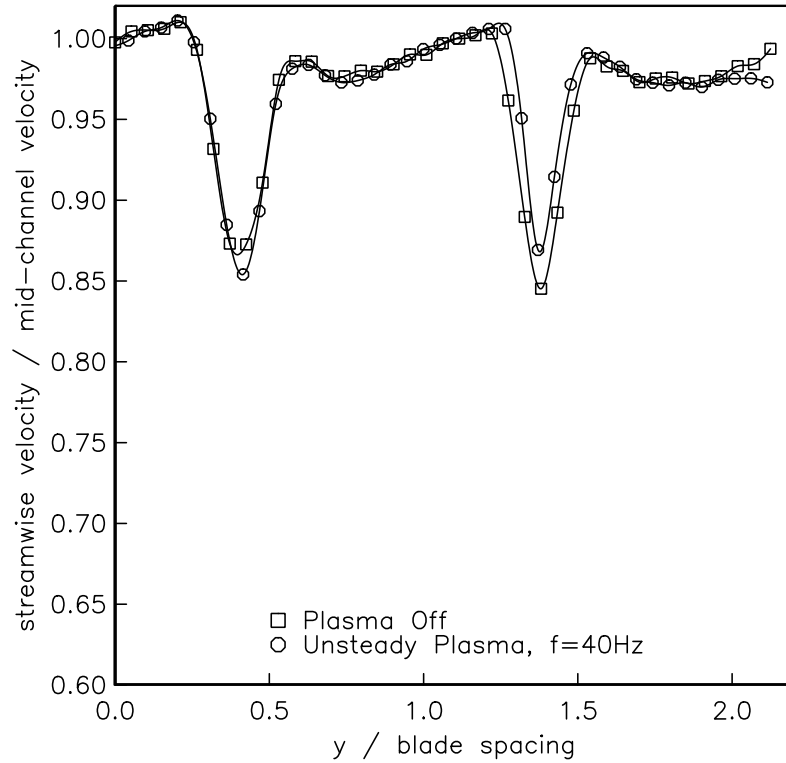
Figure 6.6. The wake profiles of "PakB" cascade for both uncontrolled and controlled cases for $Re_c = 50,000$ measured $50\%C_x$ downstream the center blade. For the controlled case, an unsteady plasma actuator was located at $x/C_x = 67.5\%$ and operated at 40 Hz. The actuator amplitude was 8 kV and the plasma duty cycle was 10%.

The wake profile is closely related to the direction of the flow in the cascade. At $Re_c = 50,000$, the flow separates and reattaches to the blade surface resulting in a long separation bubble on the suction surface for the uncontrolled case. The flow

leaves the blade in the direction tangential to the blade surface. For the controlled case, unsteady actuation significantly decreases the size of the separation bubble, which can be seen in the blade pressure distribution. However, the flow still leaves the blade in the direction tangential to the blade surface. Thus there is almost no difference in the flow direction between the uncontrolled and controlled cases. The control effect of the plasma actuator only shows in a slightly narrower wake profile.

This led us to measure the wake profiles for $Re_c = 25,000$ since the flow does not reattach for the uncontrolled case at this Reynolds number. Figure 6.7 shows the wake profiles of two consecutive blades for both uncontrolled and controlled cases for $Re_c = 25,000$ measured $50\% C_x$ downstream the center blade. For the controlled case, the excitation frequency of the unsteady plasma actuator was 20 Hz and the plasma duty cycle was 10%. Again, the right trough represents the wake of the center blade and the left trough represents the wake of the blade next to the center blade. As expected, the wake of the center blade for the controlled cases is significantly narrower than that for the uncontrolled case. Even the wake of the other blade becomes narrower than that for the uncontrolled case. This is encouraging. In a similar work conducted by Bons [2], pulsing vortex generator jets (VGJs) were used to control the separation on "PakB" blades. The VGJs narrowed the wake of the controlled blade but broadened the wake of the next blade.

The measured wake profiles can be integrated using Equation 6.4 to calculate the total pressure loss coefficient. This is shown in Figure 6.8. Due to the large wake improvement at $Re_c = 25,000$, the total pressure loss coefficient drops from 0.28 to 0.16 (a 43% improvement). At $Re_c = 50,000$, the pressure loss coefficient is not improved very much. It only drops from 0.11 to 0.09. The small improvement at $Re_c = 50,000$ is due to the slight improvement in the wake profiles. As mentioned earlier, this is because there was almost no difference in the flow direction between
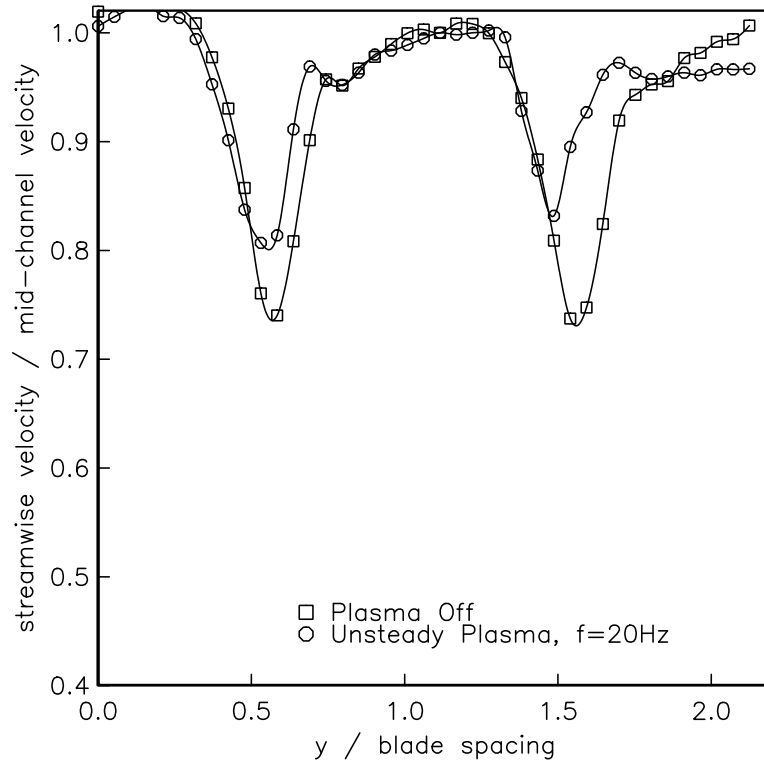
Figure 6.7. The wake profiles of "PakB" cascade for both uncontrolled and controlled cases for $Re_c = 25,000$ measured $50\%C_x$ downstream the center blade. For the controlled case, an unsteady plasma actuator was located at $x/C_x = 67.5\%$ and operated at 20 Hz. The actuator amplitude was 8 kV and the plasma duty cycle was 10%.

the uncontrolled case and the controlled case.
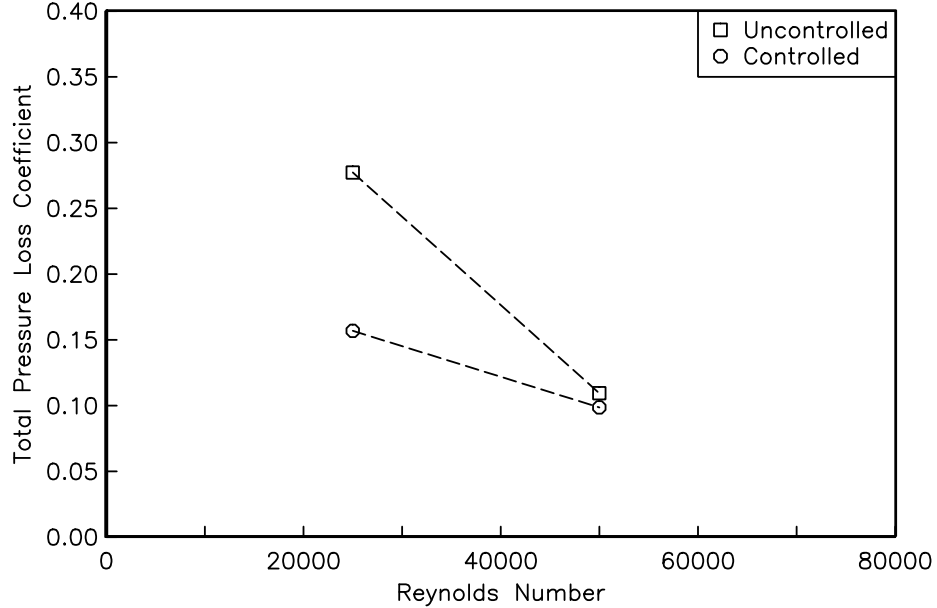
Figure 6.8. Total pressure loss coefficient calculated from the measured wake profiles for both uncontrolled and controlled cases. For controlled cases, an unsteady plasma actuator was located at $x/C_x = 67.5\%$. The excitation frequency was 40 Hz for $Re_c = 50,000$ and 20 Hz for $Re_c = 25,000$. The actuator amplitude was 8 kV and the plasma duty cycle was 10% for both Reynolds numbers.

6.6   Flow Visualization

The difference shown in the last section between two Reynolds numbers ($Re_c = 25,000$ and $Re_c = 50,000$) can be visually explained by examining flow visualization videos. Figure 6.9 shows two pictures taken from the flow video for $Re_c = 25,000$. The left picture shows the flow for the uncontrolled case and the right picture shows the flow when an unsteady plasma actuator was operated. The excitation frequency of the unsteady actuator was 20 Hz and the plasma duty cycle was 10%. For the uncontrolled case, the flow separation is clearly seen on the suction surface. The flow experiences a steep turn in the passage of the cascade. At this Reynolds number,

the energy contained in the flow was not enough to help the flow turn 95 degrees. Thus the flow separates from the surface at $x/C_x \approx 70\%$. No reattachement was observed at this Reynolds number, which results in an open separation region on the aft portion of the suction surface. For the controlled case, the unsteady plasma generates spanwise vortices, which bring the high momentum fluids down to the low momentum fluids and mixed them together. The flow separation was eliminated by this mixing mechanism. The particle streams follow the blade surface very well and leave the blade in the tangential direction.

Figure 6.10 shows two pictures taken from the flow video for $Re_c = 50,000$. Again, the left picture shows the flow field for the uncontrolled case and the right picture shows the flow field when an unsteady plasma actuator was operated. The actuator was located at $x/C_x = 67.5\%$ and operated at 40 Hz. The actuator amplitude was 8 kV and the plasma duty cycle was 10% in this case. There is no noticeable difference between these two cases. For the uncontrolled case, there is supposed to be a separation bubble on the suction side. However, it is not seen in the picture. For the controlled case, the flow followed the blade surface well and left the surface in a tangential direction. Figure 6.11 combines the measured total pressure loss coefficient and the pictures of the flow field together and provides a good connection between the total pressure loss and the corresponding flow status.
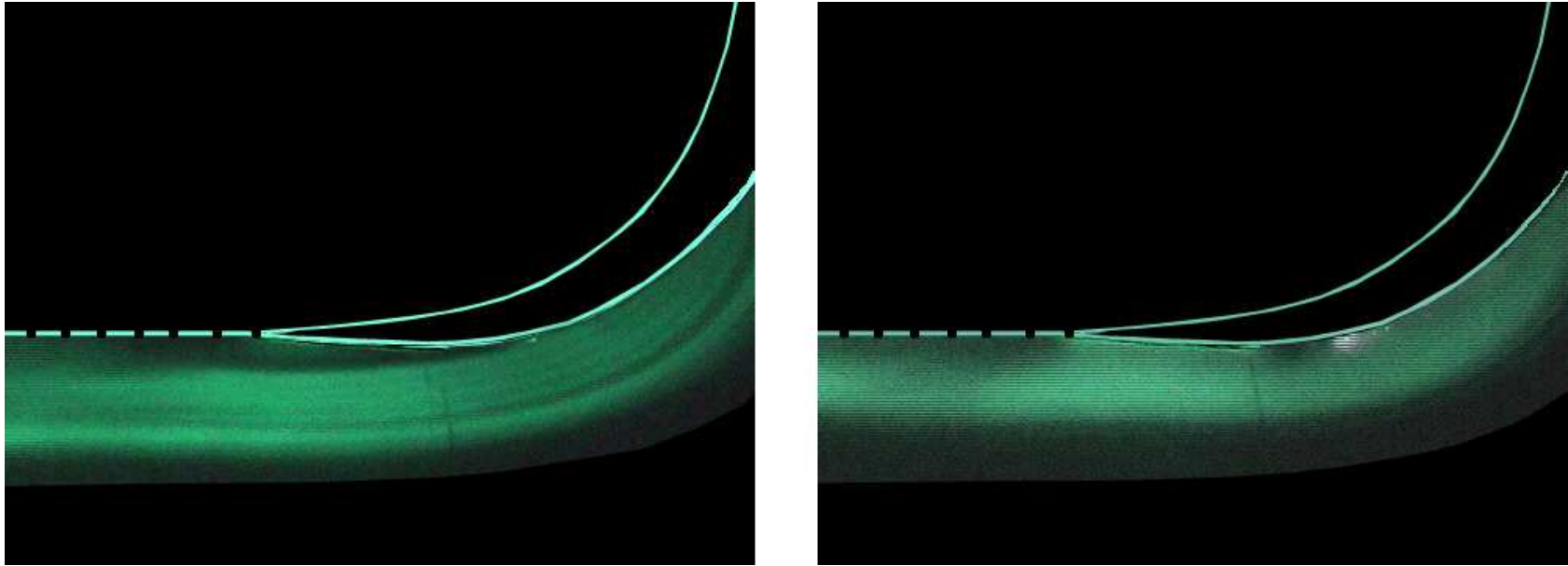
Figure 6.9. The flow field around the "PakB" blade was visualized by combining particle streams and shining laser sheet for $Re_c = 25,000$. The left picture shows the flow for the uncontrolled case and the right picture shows the flow when an unsteady plasma actuator was operated. The actuator was located at $x/C_x = 67.5\%$ and operated at 20 Hz. The actuator amplitude was 8 kV and the plasma duty cycle was 10%.
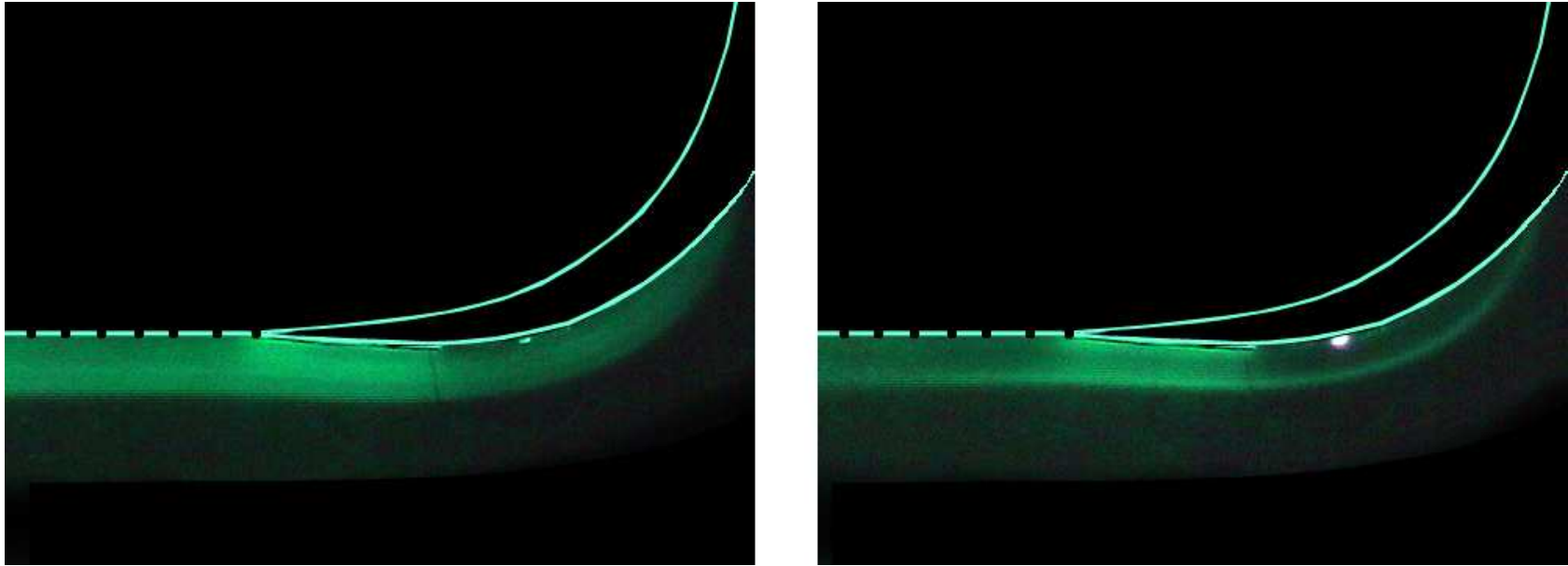
Figure 6.10. The flow field around the "PakB" blade was visualized by combining particle streams and shining laser sheet for $Re_c = 50,000$. The left picture shows the flow for the uncontrolled case and the right picture shows the flow when an unsteady plasma actuator was operated. The actuator was located at $x/C_x = 67.5\%$ and operated at 40 Hz. The actuator amplitude was 8 kV and the plasma duty cycle was 10%.
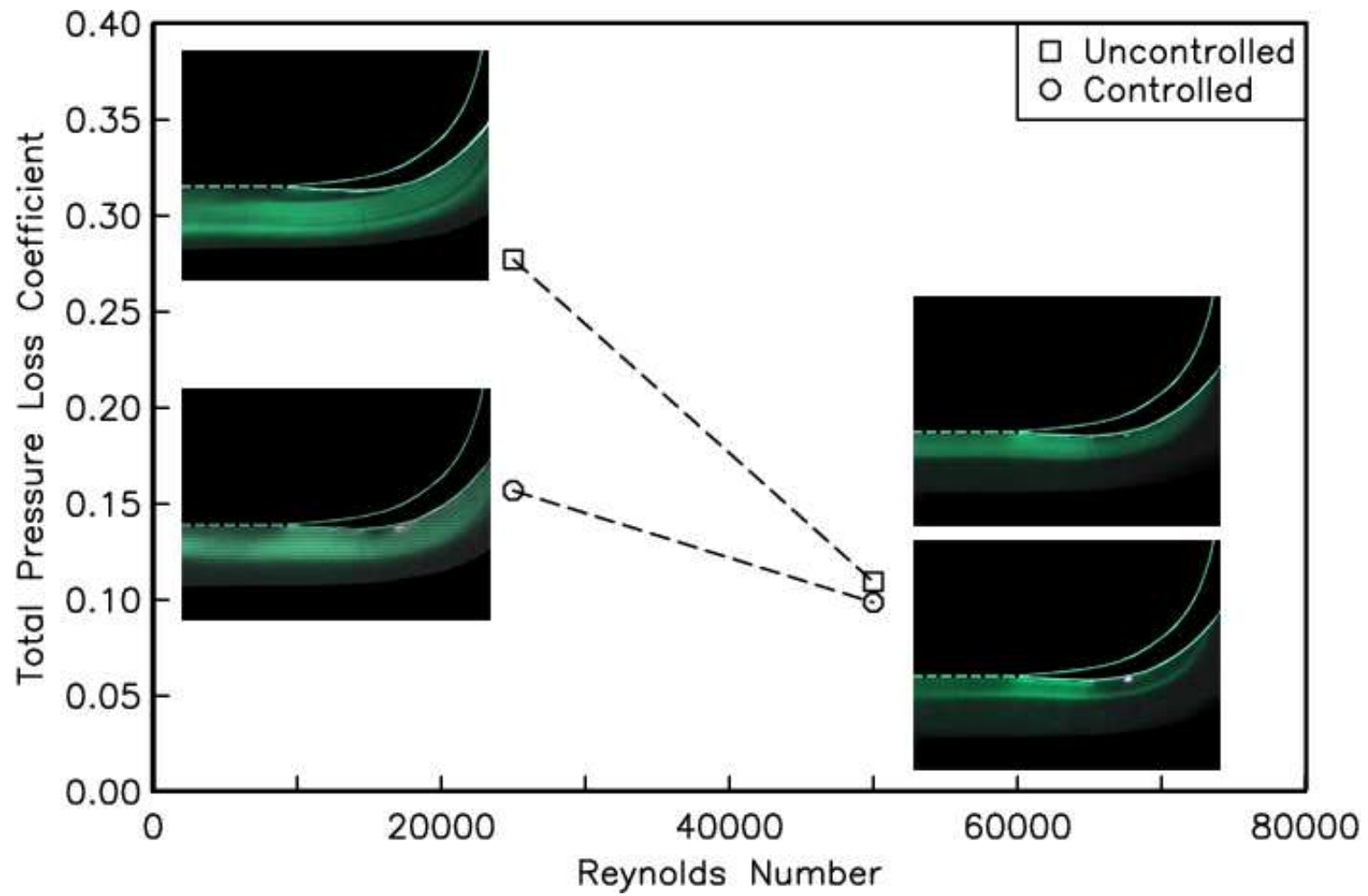
Figure 6.11. The measured total pressure loss coefficient and the corresponding flow status are combined together.

6.7   Comparison between Steady and Unsteady Actuators

At this time, it is necessary to compare the effectiveness of steady and unsteady plasma actuators. This was done by plotting the best control results obtained from steady and unsteady actuators together and comparing them side by side. Figure 6.12 shows the blade pressure distributions at $Re_c = 50,000$ for the most effective configurations of a steady plasma actuator and an unsteady plasma actuator, respectively. For the steady actuation, the plasma actuator was located at $x/C_x = 67.5\%$. The actuator amplitude was 8 kV. For the unsteady actuation, the plasma actuator was located at the same streamwise location. The excitation frequency was 100 Hz and the plasma duty cycle was 10%.

Both steady and unsteady plasma actuators showed good effectiveness at separation control. According to the blade pressure distributions, the steady actuator improved the location of reattachment point from $x/C_x = 97.5\%$ to $x/C_x = 85\%$ while the unsteady actuator improved it to $x/C_x = 87.5\%$. One may draw a conclusion that the steady actuator is more effective than the unsteady actuator. This is not true. If we observe the blade pressure distributions carefully, we can find that the blade pressure distribution for the unsteady actuator matches the Euler simulation better than the pressure distribution for the steady actuator does. Also, there is still a small plateau in the pressure distribution for the steady actuator while there is no such plateau in the pressure distribution for the unsteady actuator. Since the plateau represents the region of separation on the suction side of the blade, this indicates that there still exists a small separation bubble on the blade when the steady actuator was operated. The unsteady actuator, on the other hand, eliminated the separation completely. Therefore the unsteady plasma actuator is more effective than the steady plasma actuator.

The different effectiveness between the steady and unsteady plasma actuators
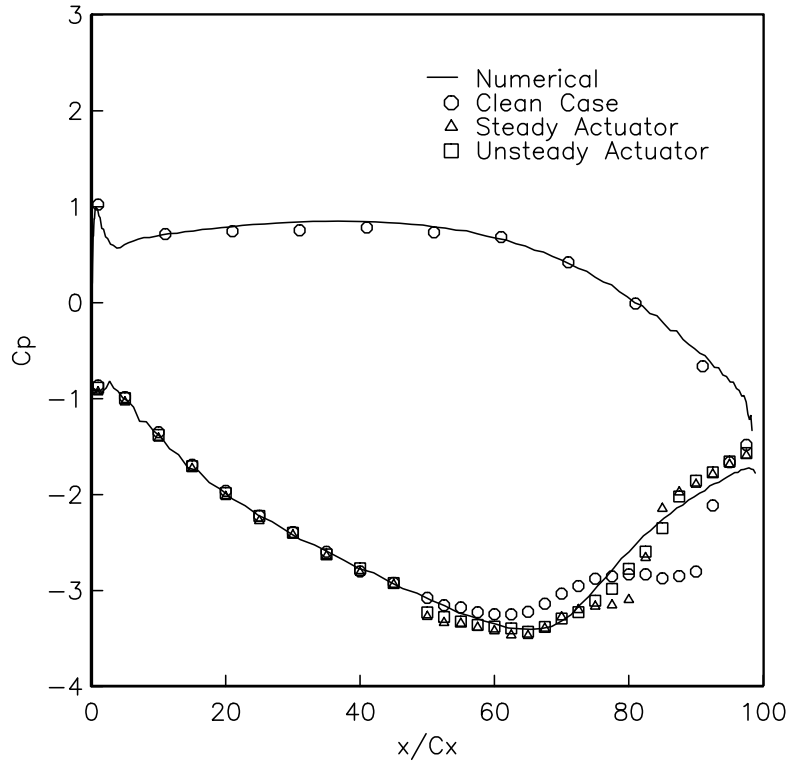
Figure 6.12. Comparison of the blade pressure distributions between the most effective steady actuator and unsteady actuators for $Re_c = 50,000$. The steady actuator was a kapton-based actuator and located at $x/C_x = 67.5\%$. The amplitude for the steady actuator was 8 kV. The unsteady actuator was a macor-based actuator and located at $x/C_x = 67.5\%$. The excitation frequency was 100 Hz, which corresponded to $S_t = 0.9$. The actuator amplitude was 24 kV and the plasma duty cycle was 10%.

originates from different mechanisms. The steady actuator acted as a trip to the flow when it was operated. The unsteady actuator generated spanwise vortices when it was operated. Thus the mechanism of the unsteady actuator was the generation of the spanwise vortices which enhanced mixing. As was shown in this chapter, the vortex generation had an optimum frequency. The mechanism of the steady and unsteady actuators is discussed in more details in the next chapter.

CHAPTER 7

MECHANISM OF STEADY AND UNSTEADY PLASMA ACTUATORS

The active separation control using plasma actuators has been proved to be successful in this research work. Encouraging results have been obtained by operating both steady and unsteady plasma actuators on "PakB" blades. It is also critical to understand the mechanism of both steady and unsteady plasma actuators. Better understanding can lead to improvement of the plasma actuator configurations and thus more effective separation control.

7.1   Flow Visualization

Flow visualization is a direct way to examine how plasma actuators worked. Figure 7.1 shows seven consecutive frames taken out of the flow videos for uncontrolled flow and controlled flow at $Re_c = 25,000$, respectively. The seven frames in the left column represent the flow field when no plasma was operated. The seven frames in the right column represent the flow field when a steady plasma actuator was operated. The bright spot in these frames is the plasma. Our attention is focused on the suction side passage. Thus the rest part of the pictures is intentionally blackened out except for the suction side passage. The pictures were enhanced in Adobe Photoshop to increase the contrast and the sharpness. The outline of the blades is also highlighted manually in Adobe Photoshop.

As discussed before, the flow separates at $x/C_x \approx 70\%$ for the uncontrolled case and does not reattach to the blade, resulting an open separation region on the

suction surface instead of forming a separation bubble. This is shown in all seven frames for the uncontrolled flow field. For the controlled case, the steady plasma actuator definitely made the flow reattach to the blade near the trailing edge. The flow looks very similar in all the seven frames for the controlled case. No particular structure is seen from these pictures. This is consistent with the idea that the mechanism of steady actuators was tripping.

For unsteady plasma actuators, similar comparison is done in Figure 7.2. The seven frames in the left column in Figure 7.2 represent the flow field when no plasma was operated. The seven frames in the right column represent the flow field when an unsteady plasma actuator was operated. For the controlled case, the plasma was operating at 20 Hz and the plasma duty cycle was 10%. Also a laser chopper was used in this case in order to capture flow structure. The frequency of the chopper was set at 21 Hz. Notice that there is 1 Hz difference between the chopper frequency and the plasma excitation frequency.

The unsteady plasma generated spanwise vortices, which brought the high momentum fluid down to the low momentum fluid near the blade surface and mixed them together. The spanwise vortices generated by the unsteady plasma can be clearly seen in Frame (b) and (e) in the right column of Figure 7.2. The excitation frequency was 20 Hz for $Re_c = 25,000$. A spanwise vortex was generated every time the plasma was generated on the blade surface. The vortex mixed the high and low momentum fluids while being convected downstream. It finally shed from the blade into the wake. At the same time, a new spanwise vortex was generated by the plasma. This way, there was always one vortex presented on the blade surface at any time.

The convection velocity of the spanwise vortex can be evaluated since the length scale is known for the pictures. By comparing Frame (a) and Frame (b) in Figure 7.2,
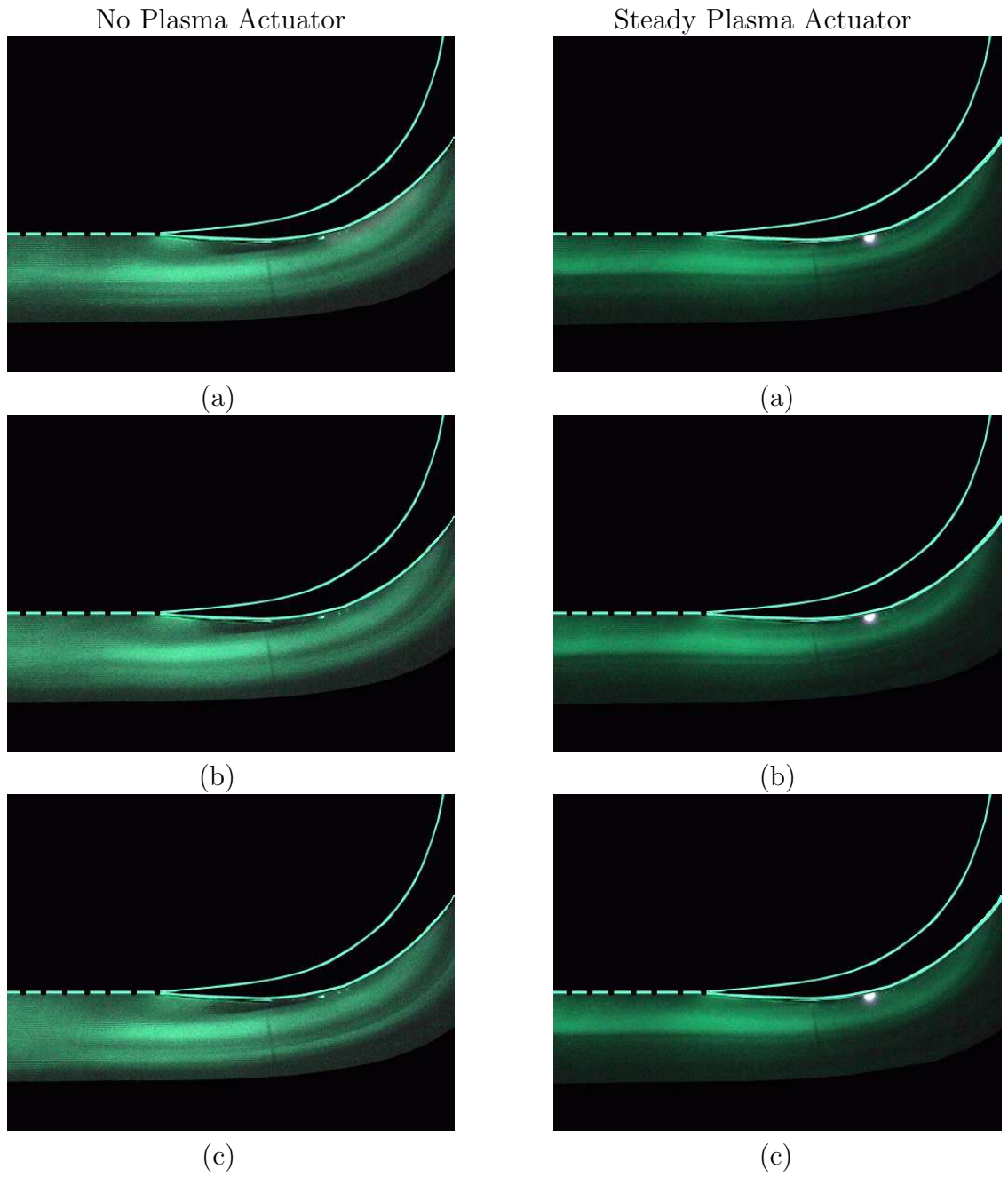
Figure 7.1. Seven consecutive frames taken from the flow videos for $Re_c = 25,000$. The frames in the left column represent the flow field for the uncontrolled case. The frames in the right column represent the flow field when a steady plasma actuator was operated. The steady plasma actuator was located at $x/C_x = 67.5\%$. The actuator amplitude was 8 kV.

(d)

(d)

(e)

(e)

(f)

(f)

Figure 7.1 (continued). Seven consecutive frames taken from the flow videos for $Re_c = 25,000$. The frames in the left column represent the flow field for the un-controlled case. The frames in the right column represent the flow field when a steady plasma actuator was operated. The steady plasma actuator was located at $x/C_x = 67.5\%$. The actuator amplitude was 8 kV.

<center>(g)   (g)</center>

Figure 7.1 (continued). Seven consecutive frames taken from the flow videos for $Re_c = 25,000$. The frames in the left column represent the flow field for the uncontrolled case. The frames in the right column represent the flow field when a steady plasma actuator was operated. The steady plasma actuator was located at $x/C_x = 67.5\%$. The actuator amplitude was 8 kV.

the convection distance of the spanwise vortex was found to be $\Delta x = 7.78$ cm. The time difference between these two frames was $\Delta t = \frac{1}{30}$ s. Thus the convection velocity of the spanwise vortex was

$$U_c = \frac{\Delta x}{\Delta t} = 2.33(m/s). \tag{7.1}$$

The local freestream velocity at $Re_c = 25,000$ was approximately 4.7 m/s. Therefore the convection velocity of the spanwise vortices was almost half of the local freestream velocity. This is the expected convection velocity for spanwise vortices.

7.2 Power Spectrum

7.2.1 The Method to Measure Power Spectrum

To understand more about the mechanism of plasma actuators, the power spectrum of the flow was measured using hot-wire anemometry. For uncontrolled cases, a Dantec IFA-100 constant temperature anemometer (CTA) was used. For controlled cases, a specially designed constant current anemometer (CCA) was built and used to measure the power spectrum when plasma was operated. The CCA

<center>133</center>

No Plasma Actuator

Unsteady Plasma Actuator

(a)

(a)

(b)

(b)

(c)

(c)
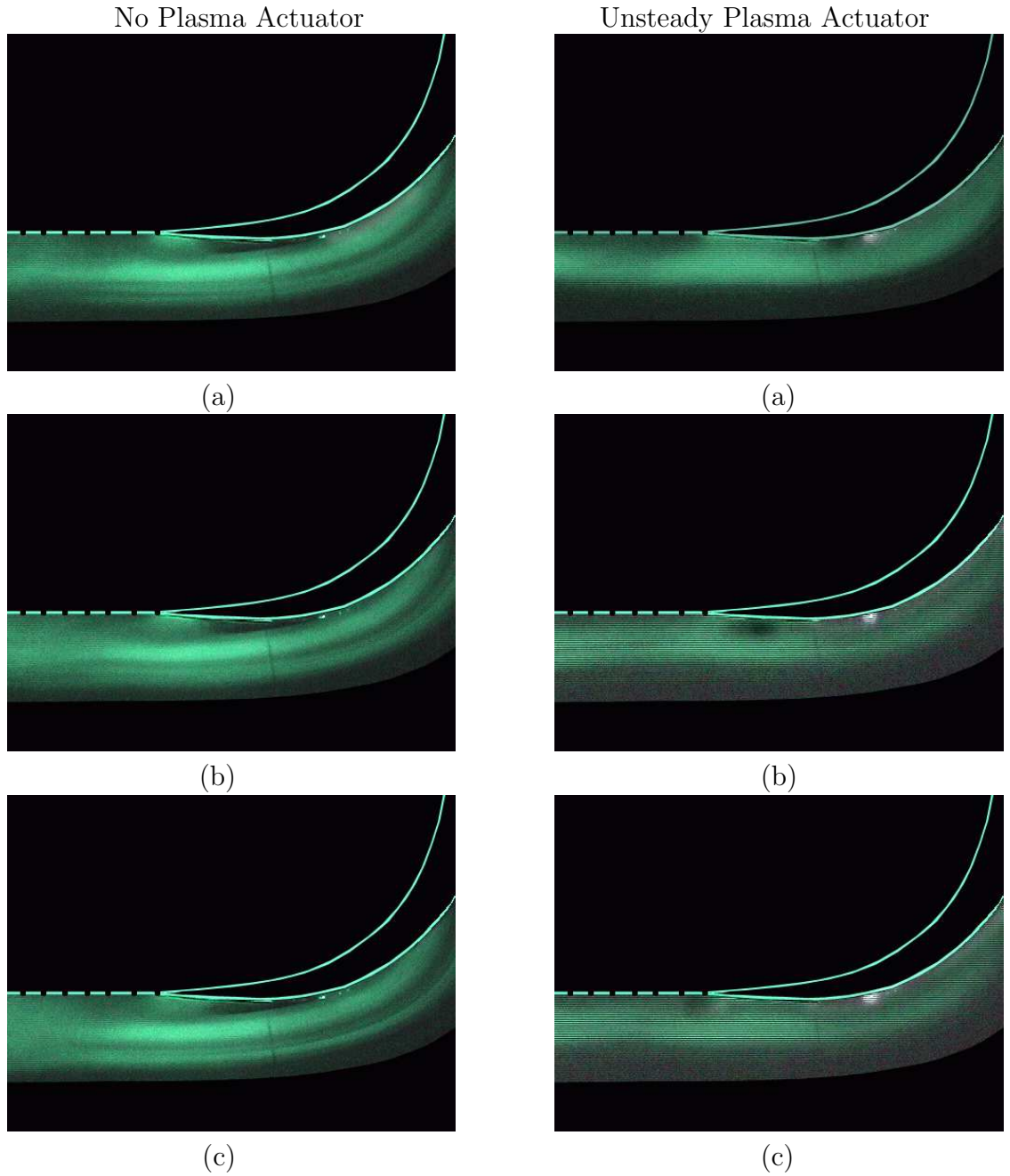
Figure 7.2. Seven consecutive frames taken from the flow videos for $Re_c = 25,000$. The frames in the left column represent the flow field for the uncontrolled case. The frames in the right column represent the flow field when an unsteady plasma actuator was operated. The unsteady plasma actuator was located at $x/C_x = 67.5\%$ and operated at 20 Hz. The actuator amplitude was 8 kV and the plasma duty cycle was 10%.

(d)

(d)

(e)

(e)

(f)

(f)

Figure 7.2 (continued). Seven consecutive frames taken from the flow videos for $Re_c = 25,000$. The frames in the left column represent the flow field for the uncontrolled case. The frames in the right column represent the flow field when an unsteady plasma actuator was operated. The unsteady plasma actuator was located at $x/C_x = 67.5\%$ and operated at 20 Hz. The actuator amplitude was 8 kV and the plasma duty cycle was 10%.

(g)   (g)

Figure 7.2 (continued). Seven consecutive frames taken from the flow videos for $Re_c = 25{,}000$. The frames in the left column represent the flow field for the un-controlled case. The frames in the right column represent the flow field when an unsteady plasma actuator was operated. The unsteady plasma actuator was located at $x/C_x = 67.5\%$ and operated at 20 Hz. The actuator amplitude was 8 kV and the plasma duty cycle was 10%.

contains a $1:31$ wiring ratio transformer, which separates the hot-wire ground and the instrument ground, to allow both hot-wire supports to "float" (see Section 2.6 for details). For the CCA, the d.c. component of the hot-wire was filtered out by the transformer. Therefore, a battery-powered handheld multimeter was used to record the d.c. output of the hot-wire during the hot-wire calibration and the power spectrum measurements.

The hot-wire measurements were conducted at six different streamwise locations for uncontrolled cases when plasma was not operated (see Table 2.5). However, when plasma was operated, the hot-wire measurements were conducted at only three streamwise locations ($x/C_x = 80\%, 85\%$, and 90%). At more upstream locations, the hot-wire was righ above the dielectric layer and the lower electrode of the actuator which was powered with high a.c. voltage. Thus the hot-wire was acting as an electrode and plasma was generated between the hot-wire and the dielectric layer.

For every streamwise locations, the hot-wire was traversed outward from the

blade surface to the local freestream to cover the whole range of the boundary layer. For every spatial point, a total of 131072 samples were acquired. The mean velocity, rms velocity were then calculated from these 131072 samples using hot-wire calibration coefficients. A C code was written to calculate the power spectrum. The flow chart of the code is shown in Figure 7.3. The 131072 samples were divided into 32 blocks and each block contains 4096 samples. For each block, the average value was calculated first and subtract from every sample. A Hanning window was applied to the time-series data before the Fourier transform. A 4096-point Fast Fourier Transform (FFT) was implemented to the time-series data. Then a compensation factor was applied to the data to compensate the error introduced by applying the Hanning window on the time-series data. Finally, an average was taken over 32 blocks to get the power spectrum of the flow.

7.2.2 Electronic Noise Test for Hot-Wire Measurements

Before I measured the power spectra of the flow using hot-wire and the specially designed CCA, a test was conducted to make sure that the hot-wire was not picking up the electronic noise when the plasma was operated. Figure 7.4 shows the setup of this test. There were two plasma actuators bonded to the center blade of the "PakB" blade which were separated by the pressure taps. Both plasma actuators were located at $x/C_x = 67.5\%$ and could be operated independently. In this test, we chose to use unsteady actuation. The hot-wire probe could be placed downstream the plasma actuators at two different spanwise positions: Position A and Position B. Position A was directly behind the upper plasma actuator and Position B was directly behind the lower plasma actuator. In this test, the hot-wire probe was first placed at Position A. The wind tunnel was off, therefore there was no flow in the tunnel. Then either the upper or the lower plasma actuator was operated. The
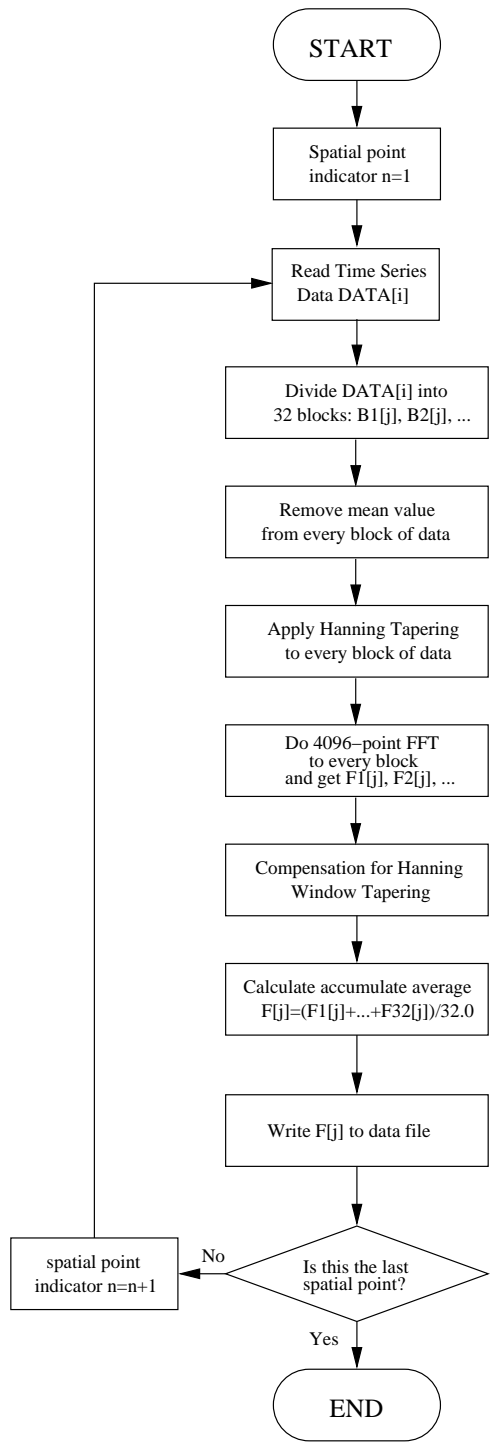
Figure 7.3. The flow chart to calculate the power spectrum.

hot-wire probe was traversed away from the blade surface while acquiring data. Two sets of data were obtained at Position A. After that, the hot-wire probe was placed at Position B and the same measurements were done to obtain another two sets of data. The four sets of data are denoted as Case 1 to 4 as shown in Table 7.1.
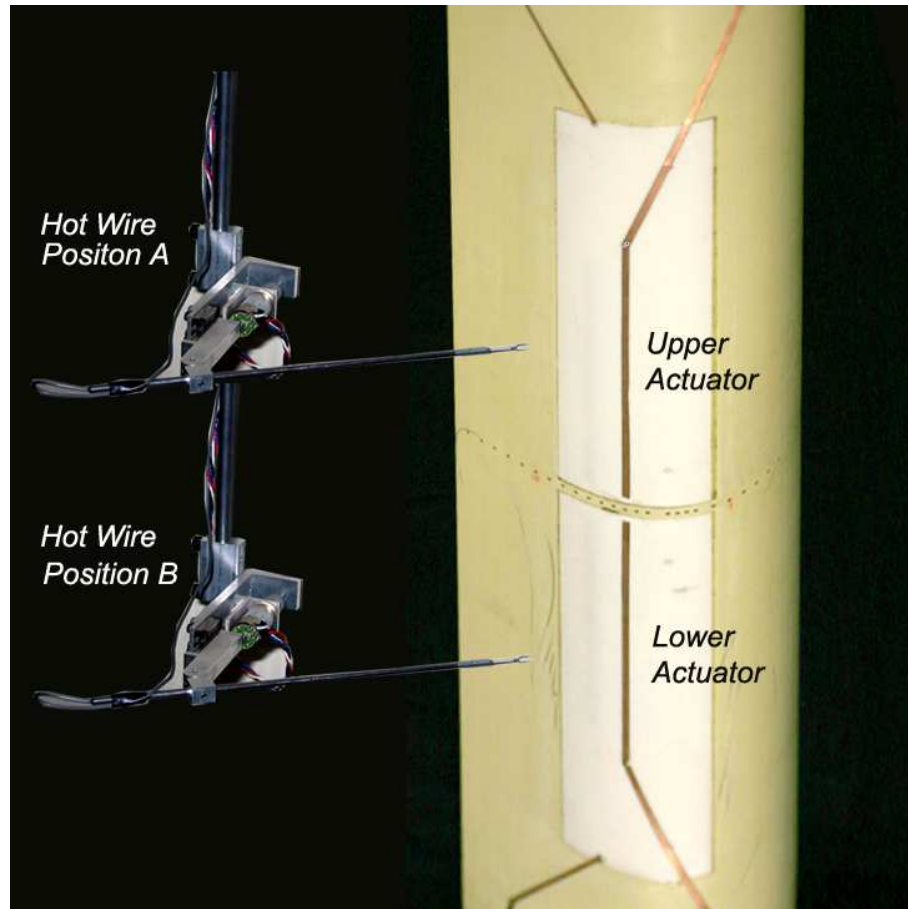
Figure 7.4. The experimental setup to check the electronic noise from plasma actuators for hot-wire measurements.

Figure 7.5 shows the measured power spectra at five different wall normal distances at $x/C_x = 85\%$ for Case 1 in Table 7.1. In this case, the hot-wire was directly behind the upper plasma actuator which was operated at 100 Hz. The lower actuator was off. It can be seen from the power spectra that peaks at 100 Hz and its

TABLE 7.1

HOT-WIRE TEST CASES TO CHECK ELECTRONIC NOISE

Case No.	Hot-Wire	Upper Actuator	Lower Actuator
1	Position A	On	Off
2	Position A	Off	On
3	Position B	On	Off
4	Position B	Off	On

harmonics dominate other frequencies. These peaks are corresponding to the flow disturbances generated by the upper plasma actuator.

Figure 7.6 shows the measured power spectra at five different wall normal distances at $x/C_x = 85\%$ for Case 2 in Table 7.1. In this case, the hot-wire probe was directly behind the upper plasma actuator which was off. The lower actuator was operated at 100 Hz. It can be seen that there are small peaks in the power spectra. However, the amplitude of these peaks are at least two orders less than that in Figure 7.5, which indicates that the hot-wire did not pick up electronic noise from the high a.c. voltage applied to the lower plasma actuator.

The power spectra for Case 3 and Case 4 in Table 7.1 look very similar to Figure 7.6 and Figure 7.5, respectively. Combining the results shown above, a conclusion can be drawn that the peaks shown in Figure 7.5 are not the electronic noise from plasma actuators. Instead, they are related to the flow disturbances generated by the unsteady plasma actuators.

7.2.3   Power Spectra of the Flow With and Without Plasma

The power spectra of the flow field without plasma was measured at six different streamwise locations. Figure 7.7 shows the power spectra for five different wall
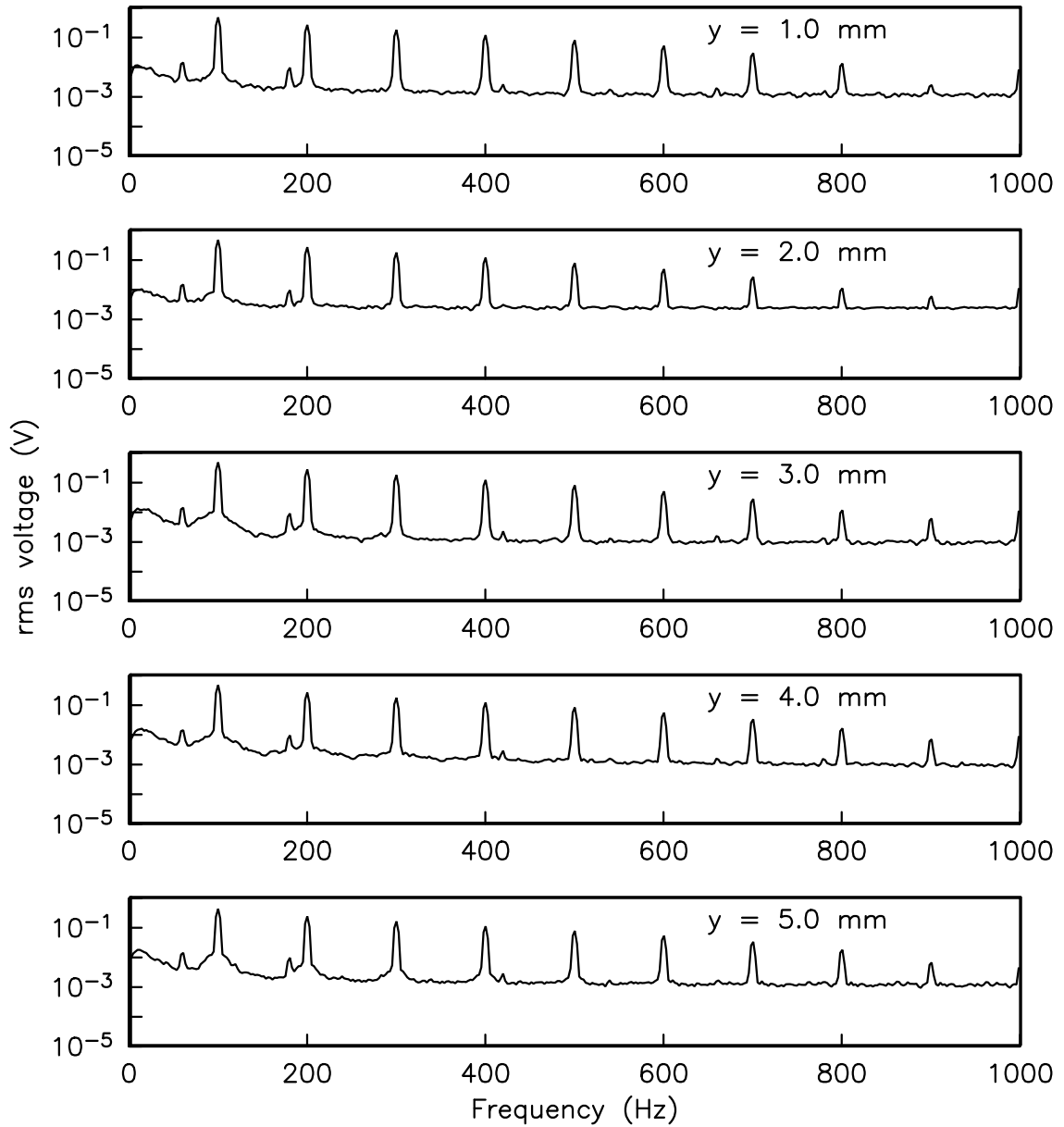
Figure 7.5. Power spectra for five wall normal distances at $x/C_x = 85\%$ for Case 1 in Table 7.1. The unsteady plasma actuator was located at $x/C_x = 67.5\%$ and operated at 100 Hz. The actuator amplitude was 24 kV and the plasma duty cycle was 10%.
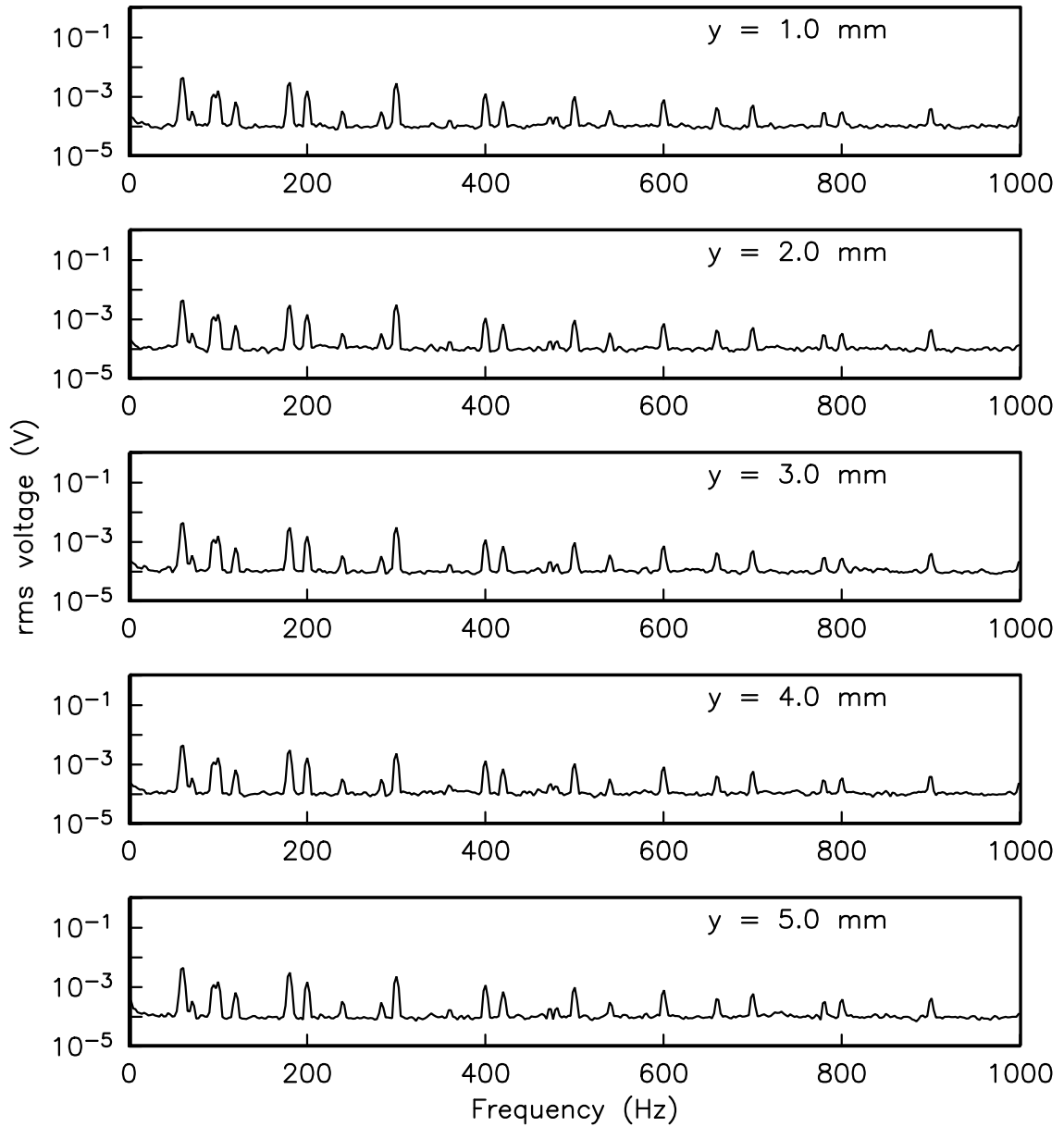
Figure 7.6. Power spectrum for five wall normal distances at $x/C_x = 85\%$ for Case 2 in Table 7.1. The unsteady plasma actuator was located at $x/C_x = 67.5\%$ and operated at 100 Hz. The actuator amplitude was 24 kV and the plasma duty cycle was 10%.

normal distances at $x/C_x = 60\%$ for the uncontrolled flow field at $Re_c = 50,000$. The flow is attached at this streamwise location according to the boundary layer profiles shown in Chapter 3. It can be seen that the energy of the flow is mainly contained in a narrow range of low frequencies around 10 Hz at all five wall normal distances. At $y = 1$ mm, there are two energy peaks at 45 Hz and 60 Hz in addition to the low frequency peak. The peak at 60 Hz is related to the electricity noise and is also shown in other plots. On the other hand, the peak at 45 Hz vanished at other wall normal distances. Since the energy is contained in a narrow range of frequencies instead of distributing in a wide range of frequencies, the flow is still laminar at this streamwise location. Figure 7.8 and Figure 7.9 show the power spectra for five different wall normal distances at $x/C_x = 70\%$ and 75%, respectively, for the uncontrolled flow field at $Re_c = 50,000$. The power spectra at these two streamwise locations look very similar to those at $x/C_x = 60\%$, which indicates that flow is still laminar at these two locations.

Figure 7.10 shows the power spectra for five different wall normal distances at $x/C_x = 80\%$ for the uncontrolled flow field at $Re_c = 50,000$. The flow is separated at this streamwise location. The height of the separation bubble is about 2.5 mm according to the boundary layer profiles shown in Chapter 3. Therefore the first two plots in Figure 7.10 show the power spectra of the low momentum flow inside the separation bubble. For both plots there is a peak at 17 Hz and the energy is narrowly distributed around this frequency. This indicates that the flow in the separation bubble is still laminar. Because of the detachment of the boundary layer, a shear layer is formed at this streamwise location. The third and the fourth plots in Figure 7.10 show the power spectra in the shear layer at this streamwise location. These two plots look very similar. Both have a high, narrow peak at about 17 Hz and some small peaks at higher frequencies. The last plot in Figure 7.10 shows the

143
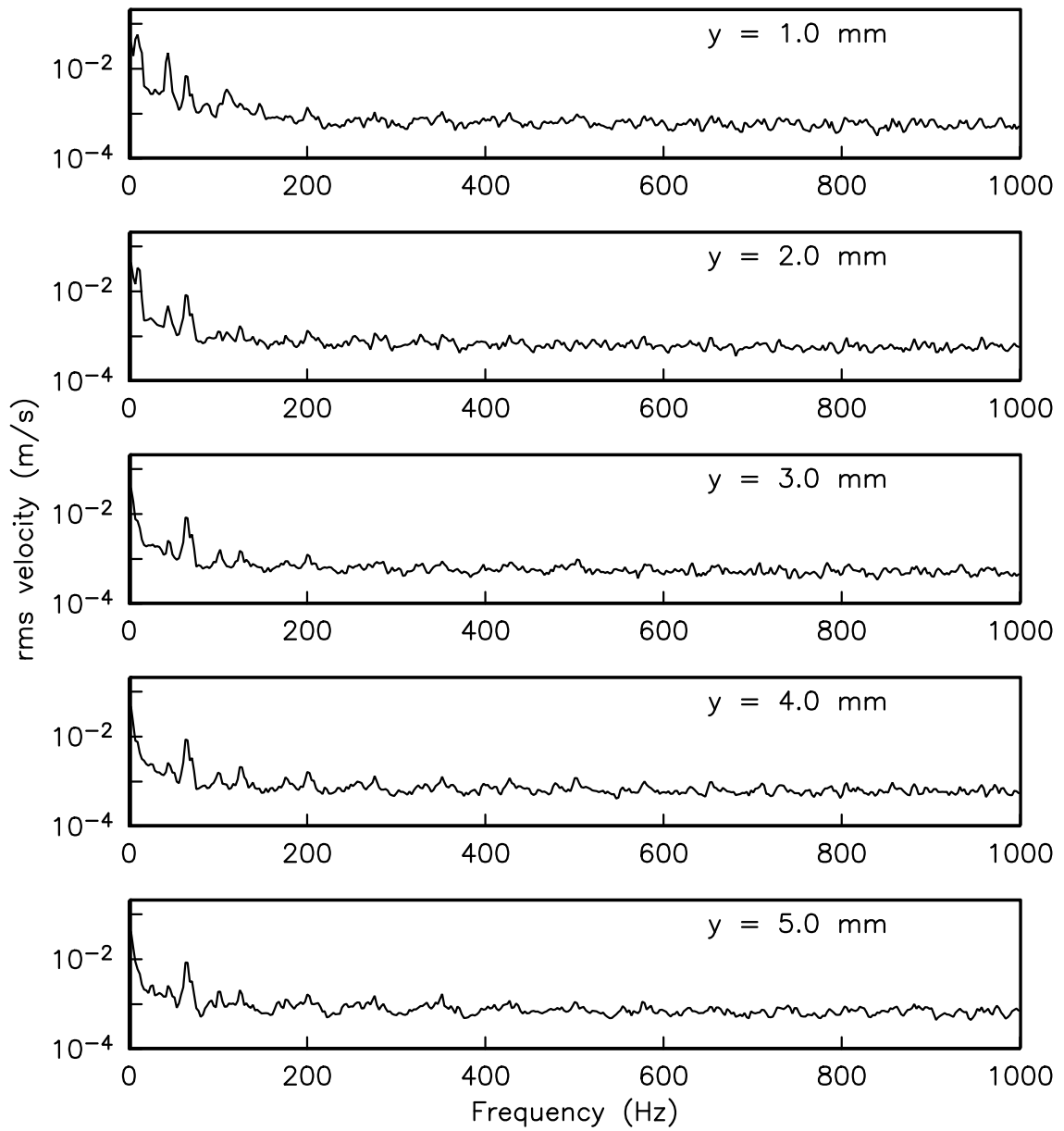
Figure 7.7. Power spectra for five wall normal distances at $x/C_x = 60\%$ for the uncontrolled flow field at $Re_c = 50,000$.

144
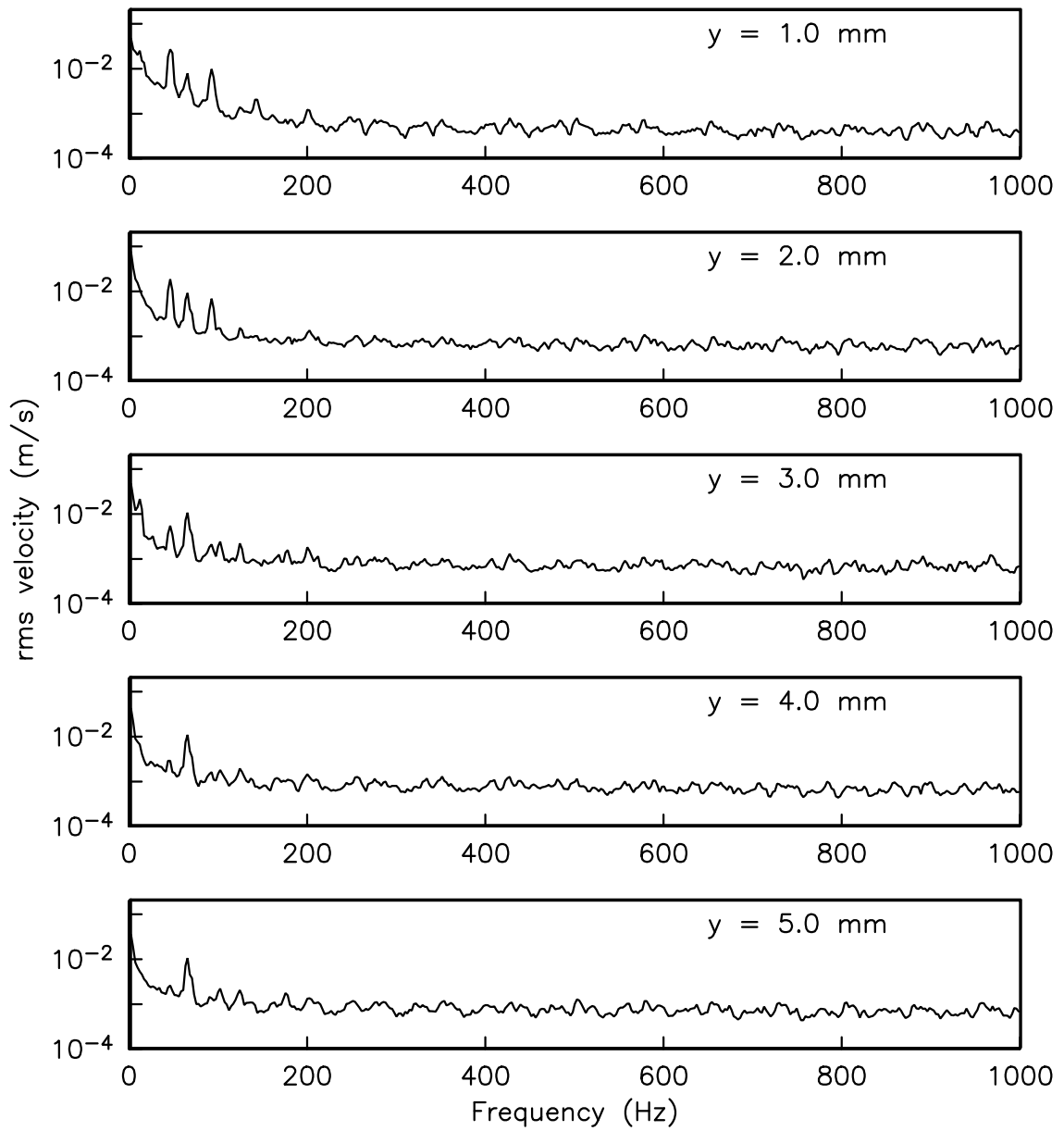
Figure 7.8. Power spectra for five wall normal distances at $x/C_x = 70\%$ for the uncontrolled flow field at $Re_c = 50,000$.
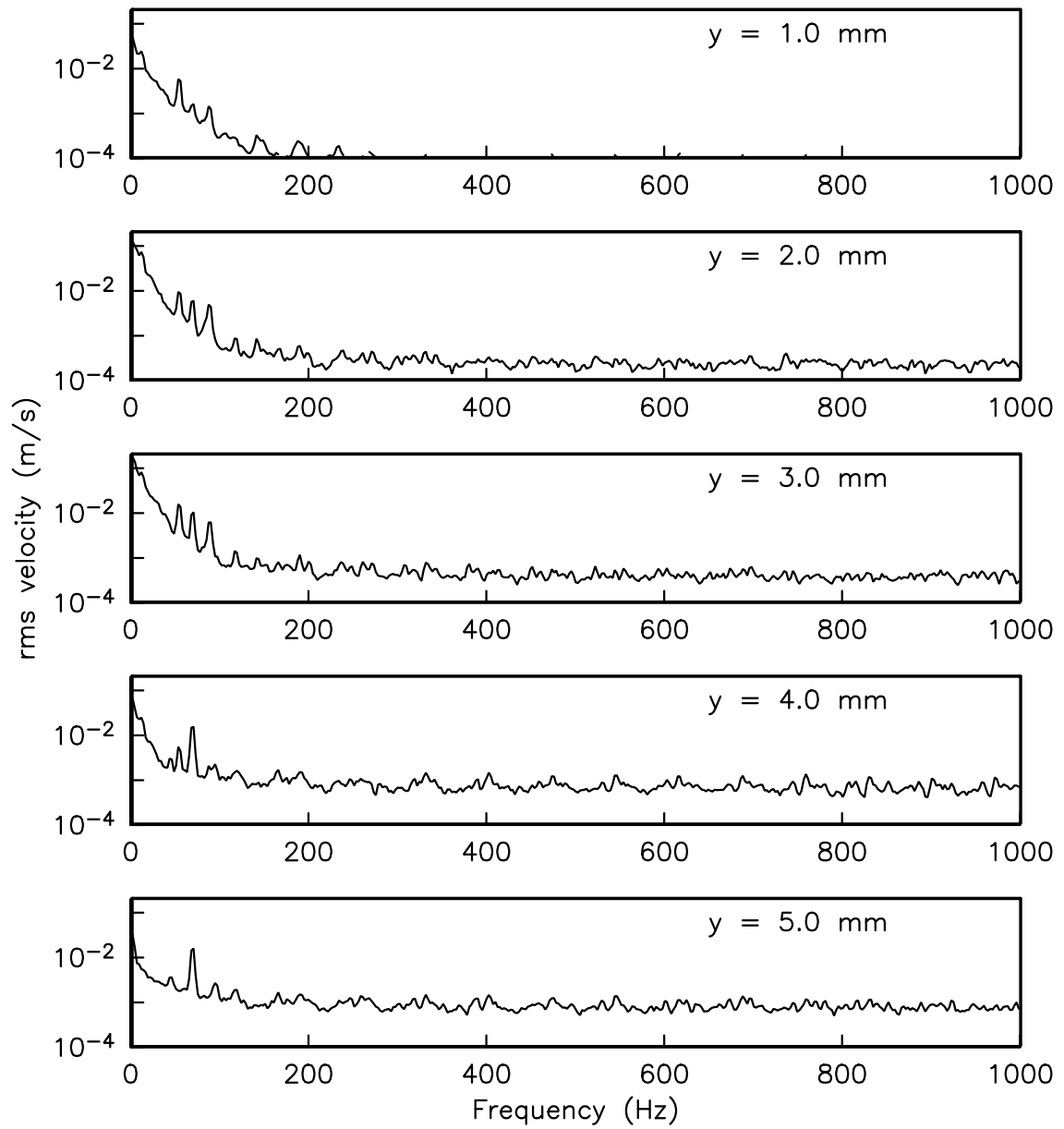
Figure 7.9. Power spectra for five wall normal distances at $x/C_x = 75\%$ for the uncontrolled flow field at $Re_c = 50,000$.

146

power spectrum of local freestream. There is still a peak at 17 Hz, though not as high as that in the third and the fourth plots. There are a few peaks at higher frequencies. This wall normal distance is at the upper edge of the shear layer. Thus the high frequency peaks may be related to the instability frequencies of the shear layer.

Figure 7.11 shows the power spectra for five different wall normal distances at $x/C_x = 85\%$ for the uncontrolled flow field at $Re_c = 50,000$. Note that the flow is still separated at this streamwise location. According to the LDV measurements, the height of the separation bubble at this streamwise location is about 4 mm. Inside the separation bubble is low momentum fluid. There is a shear layer forming from $y = 4$ mm to $y = 6.5$ mm. Thus the first three plots in Figure 7.11 show the power spectra of the low momentum flow in the separation bubble. Not like the power spectra measured at $x/C_x = 80\%$, there is no apparent high peaks in these three plots. Instead, the energy is distributed in a fairly wide range of frequencies $(0 \sim 400$ Hz$)$. This indicates that the flow is not laminar any more. The last two plots in Figure 7.11 shows the power spectrum in the shear layer. The power spectra look fuller that those in the first three plots, which indicate the flow contains more energy in these two wall normal distances. Also a new energy peak around 300 Hz appeared at $y = 5$ mm. This energy peak is believed to be associated to the instability of the shear layer.

Figure 7.12 shows the power spectra for five different wall normal distances at $x/C_x = 90\%$ for the uncontrolled flow field at $Re_c = 50,000$. Again, the flow is still separated at this streamwise location. However, the height of the separation bubble is about 3.5 mm, which is smaller than that at $x/C_x = 85\%$. Although the first four plots show the power spectra of the flow in the separation bubble, the power spectra is much fuller than those measured at $x/C_x = 80\%$ and 85%. The energy is more
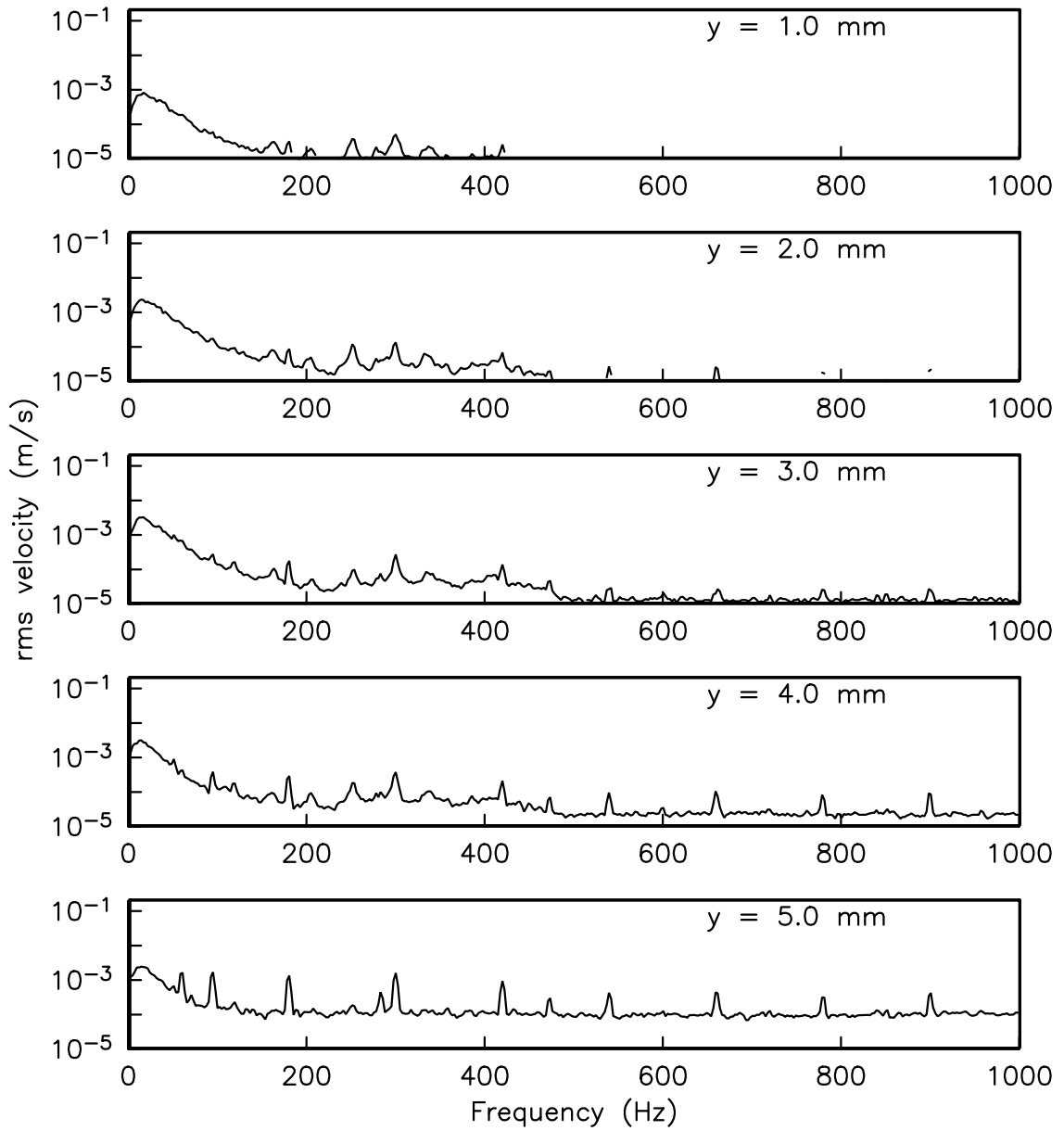
Figure 7.10. Power spectra for five wall normal distances at $x/C_x = 80\%$ for the uncontrolled flow field at $Re_c = 50,000$.
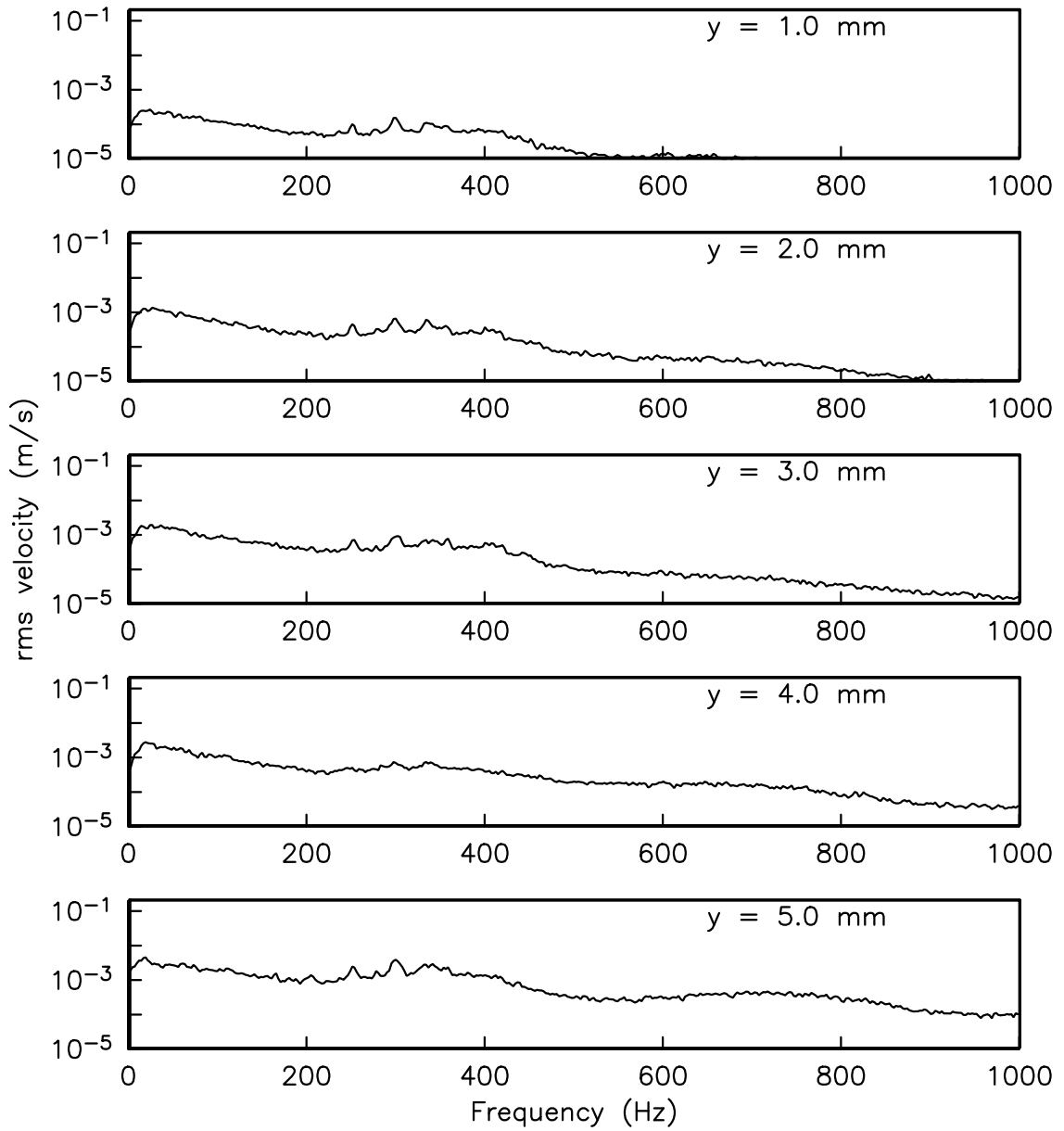
Figure 7.11. Power spectra for five wall normal distances at $x/C_x = 85\%$ for the uncontrolled flow field at $Re_c = 50,000$.

evenly distributed in a wide range of frequencies ($0 \sim 1000$ Hz). This indicates that the flow is already turbulent. The fifth plot looks similar to the other four plots except for the higher amplitude, which indicates that the flow is turbulent too at this wall normal distance.

Figure 7.13 shows the power spectra for five different wall normal distances measured at $x/C_x = 80\%$ for the controlled flow field at $Re_c = 50,000$ when a steady plasma actuator was operated. The steady plasma actuator was located at $x/C_x = 67.5\%$ and the actuator amplitude was 8 kV. The actuator electrodes were oriented so that the actuator generated a steady wall jet when operated. For the steady plasma actuators, the flow is still separated at this streamwise location. However, the height of the separation bubble is much smaller than the uncontrolled case. According to the boundary layer profiles shown in Chapter 3, the height of the separation bubble is about 1.2 mm. The power spectra for the first two plots look similar to those measured at $x/C_x = 85\%$ for the uncontrolled case. There is no apparent peak in the power spectra and the energy is distributed in a fairly wide range of frequencies. This indicates that the flow is not laminar. For the power spectra at $y = 3$ mm and 4 mm, there is a peak at 17 Hz and the energy is distributed at higher frequencies.

Figure 7.14 and Figure 7.15 shows the power spectra for five different wall normal distances measured at $x/C_x = 85\%$ and $x/C_x = 90\%$, respectively, for the controlled flow field at $Re_c = 50,000$ when a steady plasma actuator was operated. At these two streamwise locations, the flow is already reattached due to the tripping of the steady plasma actuator. The energy is distributed in a wide range of frequencies in all the plots in these two figures. This indicates that the flow is fully turbulent at these two streamwise locations. The power spectra for five different wall normal distances looks similar to one another, except that the power spectrum curve becomes
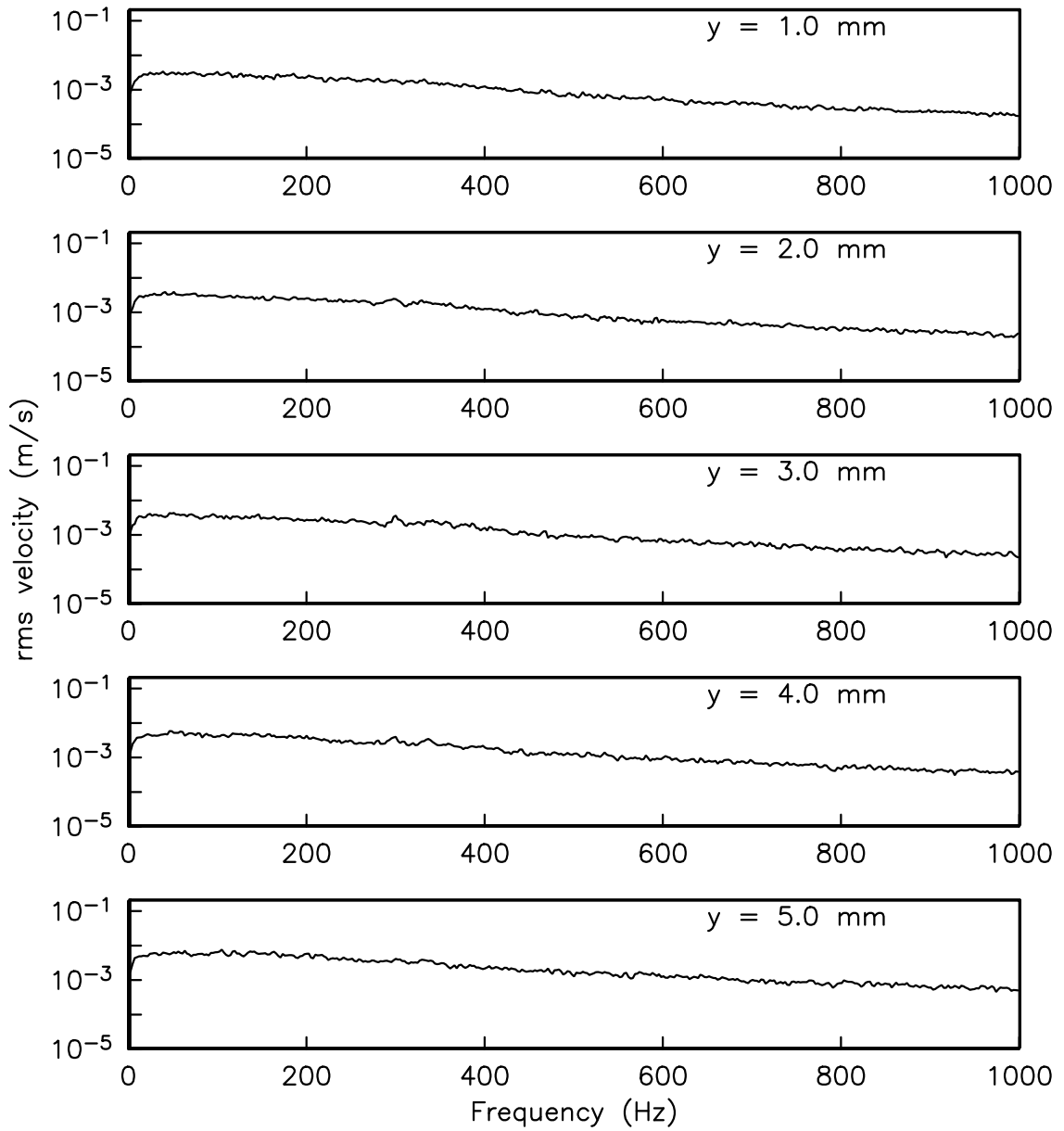
Figure 7.12. Power spectra for five wall normal distances at $x/C_x = 90\%$ for the uncontrolled flow field at $Re_c = 50,000$.
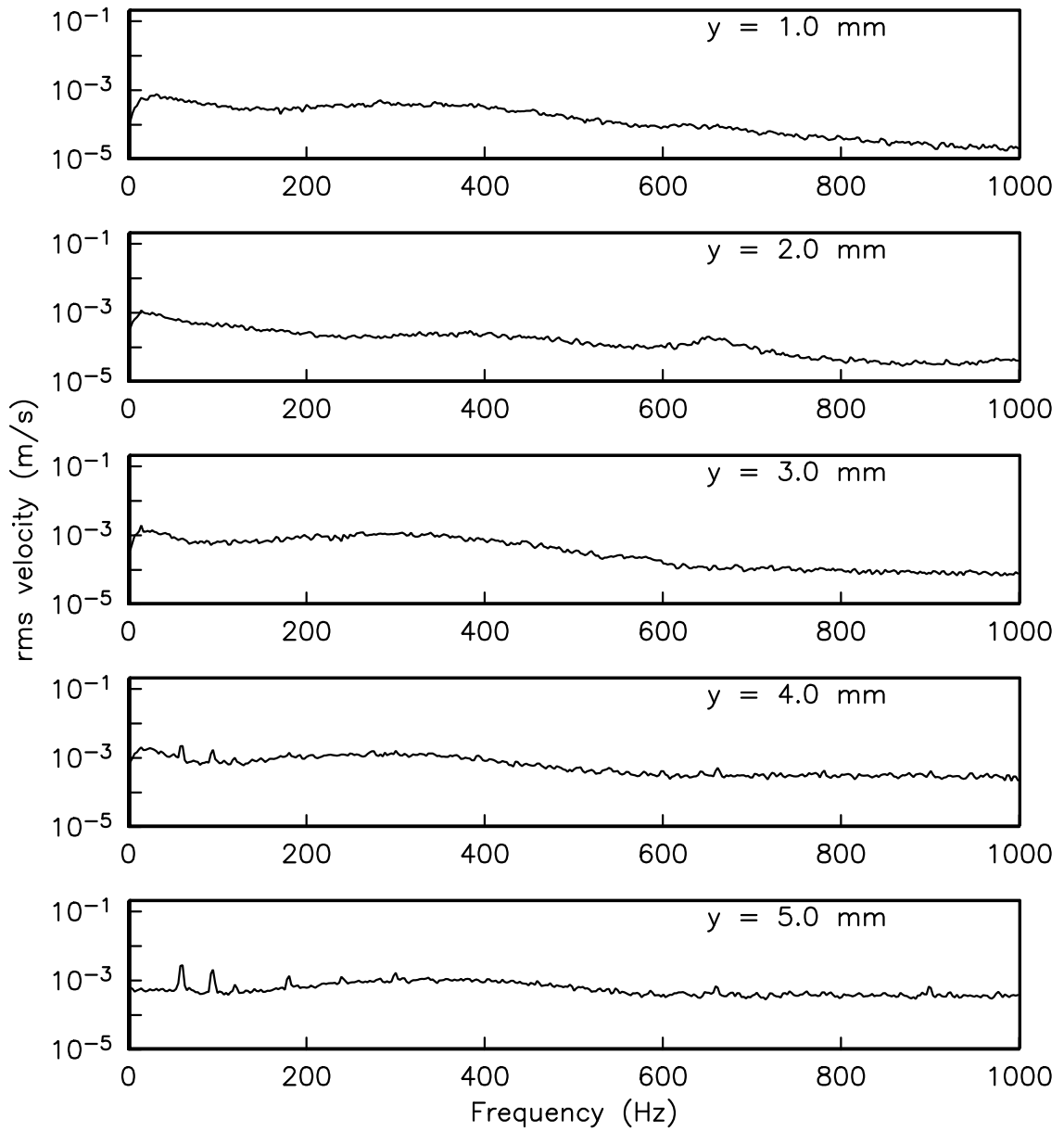
Figure 7.13. Power spectra for five wall normal distances at $x/C_x = 80\%$ for the controlled flow field at $Re_c = 50,000$ using a steady plasma actuator. The actuator was a kapton-based actuator and located at $x/C_x = 67.5\%$. The amplitude of the actuator was 8 kV.

fuller when moving away from the blade surface.

Figure 7.16, Figure 7.17, and Figure 7.18 show the power spectra for five different wall normal distances measured at $x/C_x = 80\%$, 85%, and 90%, respectively, for the controlled flow field at $Re_c = 50,000$. An unsteady plasma actuator was operated in this case. The excitation frequency of the actuator was 100 Hz and the plasma duty cycle was 10%. The energy distribution pattern is dramatically different from that of the uncontrolled case and the steady actuator case. In all the plots in these three figures, the excitation frequency and its harmonics (200 Hz, 300 Hz, 400 Hz, etc.) dominate other frequencies. Actually they are so dominant that the energy contained in other frequencies is barely seen in these plots. These energy peaks are corresponding to the spanwise vortices generated by the unsteady plasma. As shown in the flow visualization section, the unsteady plasma actuator generated spanwise vortices on the blade surface. These vortices were converted downstream and finally shed into the wake. These vortices contains high energy thus leaving peaks on the power spectra.

From the results discussed above, it is clear that the steady plasma actuators resulted in an earlier transition of the flow. When the steady actuators were discussed in Chapter 4, it was found that the orientation of the electrodes made no difference to the separation control. This indicates that the mechanism of the steady plasma actuators is tripping. Therefore the flow was tripped by the steady plasma actuators to transition from laminar to turbulent earlier than the uncontrolled case and reattached to the blade surface earlier than the uncontrolled case. On the other hand, the mechanism of the unsteady plasma actuators is mixing. The mixing is achieved by the spanwise vortices generated by the unsteady plasma actuator, which were observed in both the flow visualizations and the power spectra.
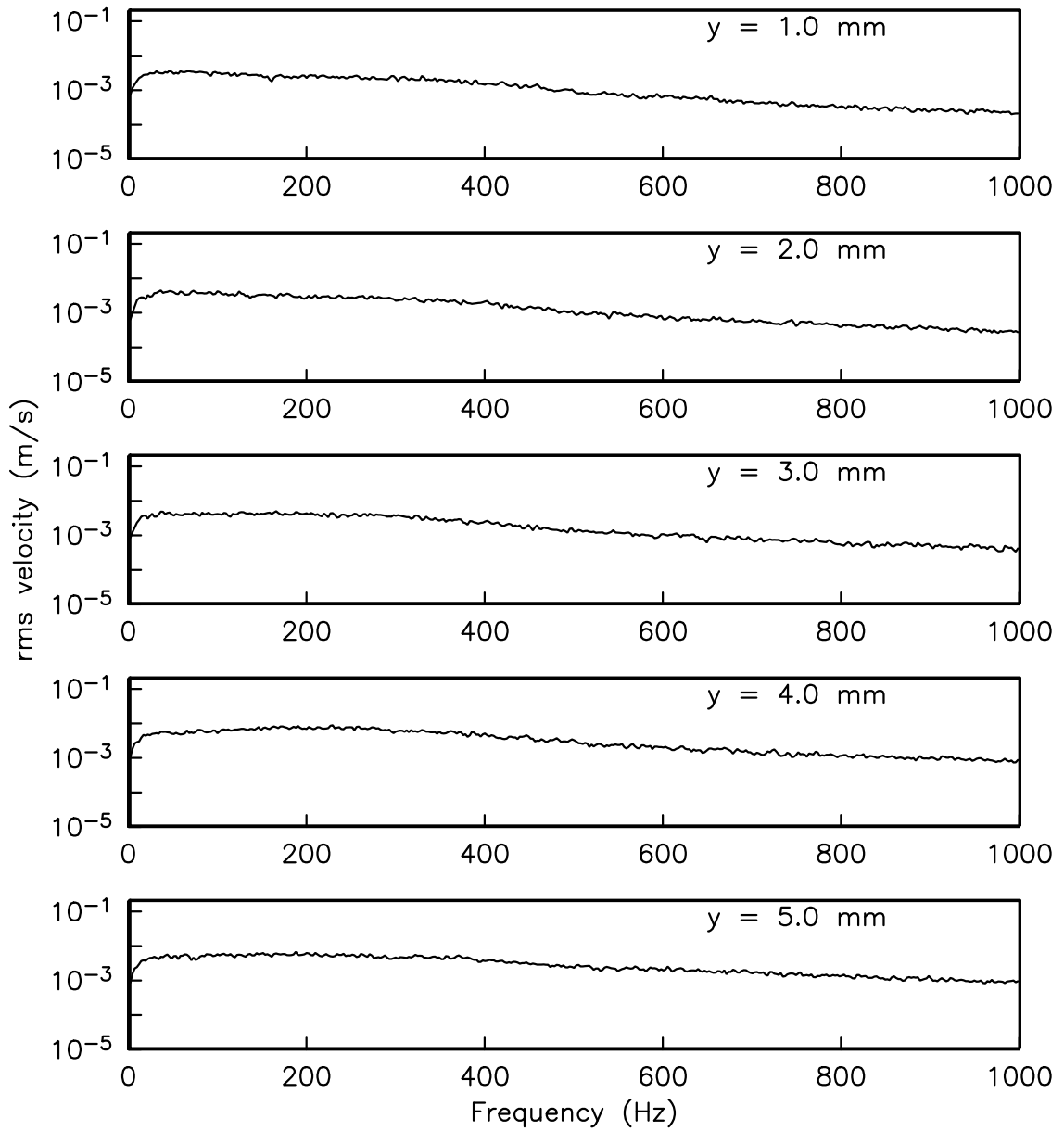
Figure 7.14. Power spectra for five wall normal distances at $x/C_x = 85\%$ for the controlled flow field at $Re_c = 50,000$ using a steady plasma actuator. The actuator was a kapton-based actuator and located at $x/C_x = 67.5\%$. The amplitude of the actuator was 8 kV.
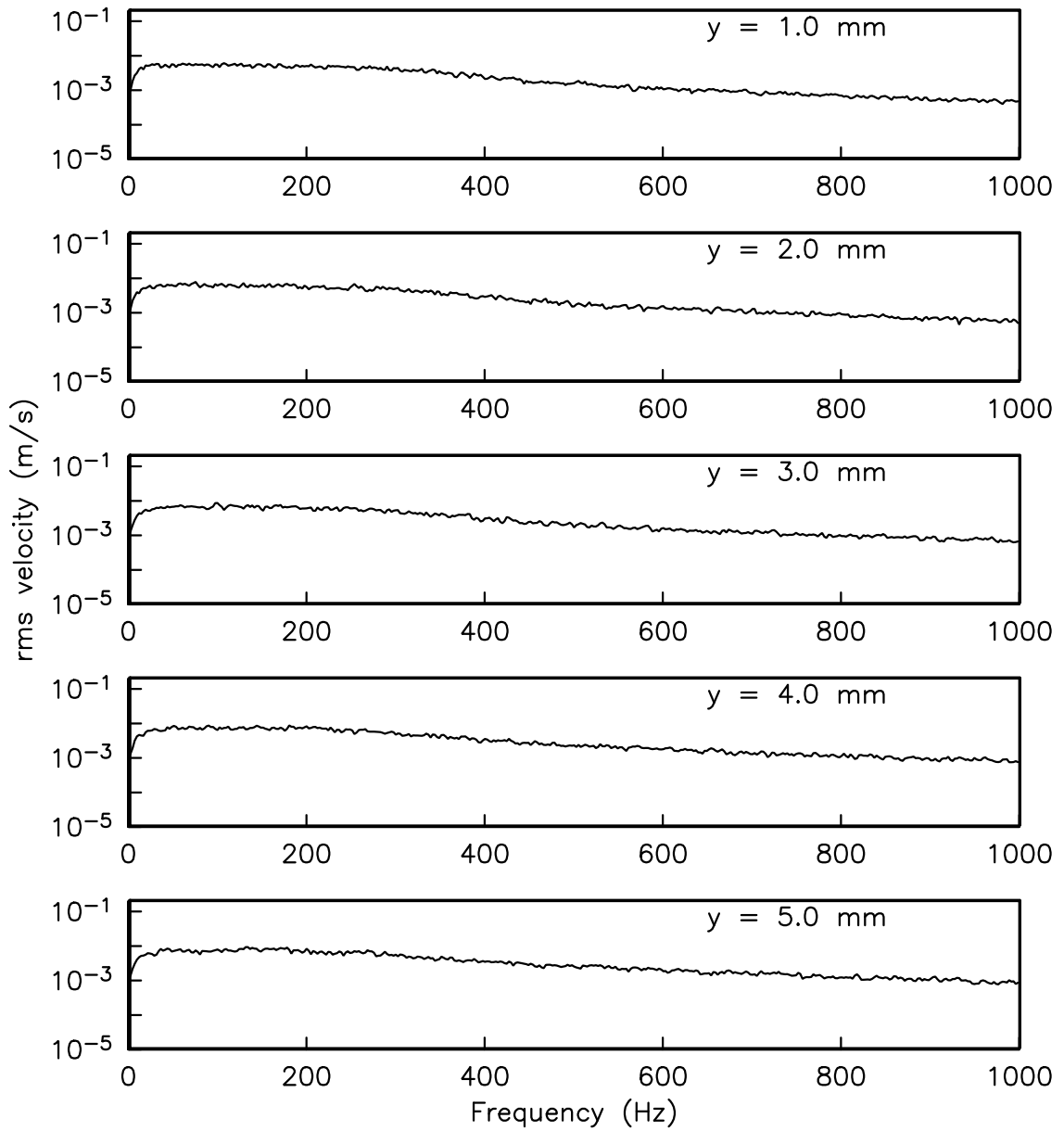
Figure 7.15. Power spectra for five wall normal distances at $x/C_x = 90\%$ for the controlled flow field at $Re_c = 50,000$ using a steady plasma actuator. The actuator was a kapton-based actuator and located at $x/C_x = 67.5\%$. The amplitude of the actuator was 8 kV.
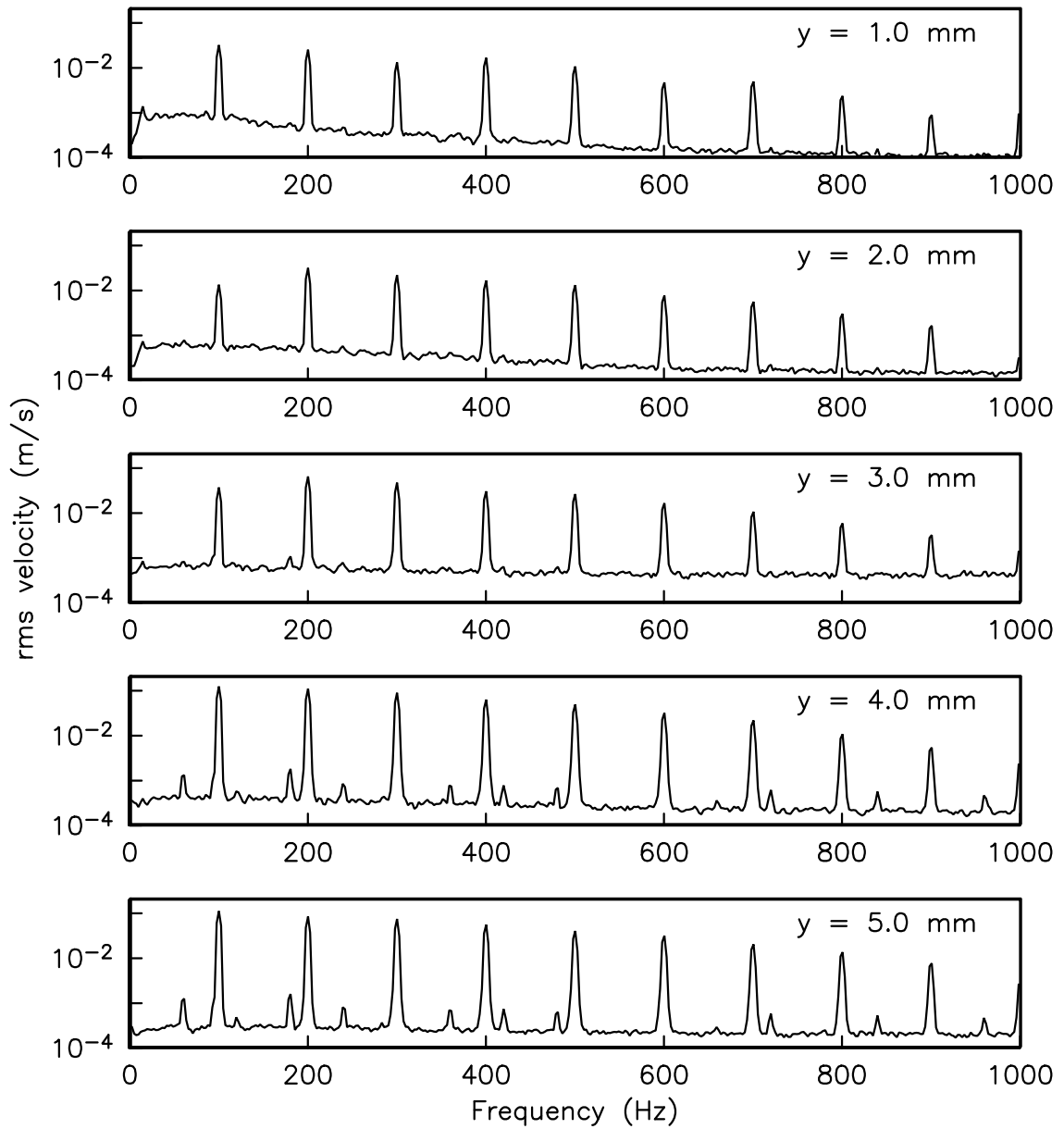
Figure 7.16. Power spectra for five wall normal distances at $x/C_x = 80\%$ for the controlled flow field at $Re_c = 50,000$ using an unsteady plasma actuator. The plasma actuator was a macor-based actuator and located at $x/C_x = 67.5\%$. The actuator amplitude was 24 kV. The excitation frequency was 100 Hz and the plasma duty cycle was 10%.
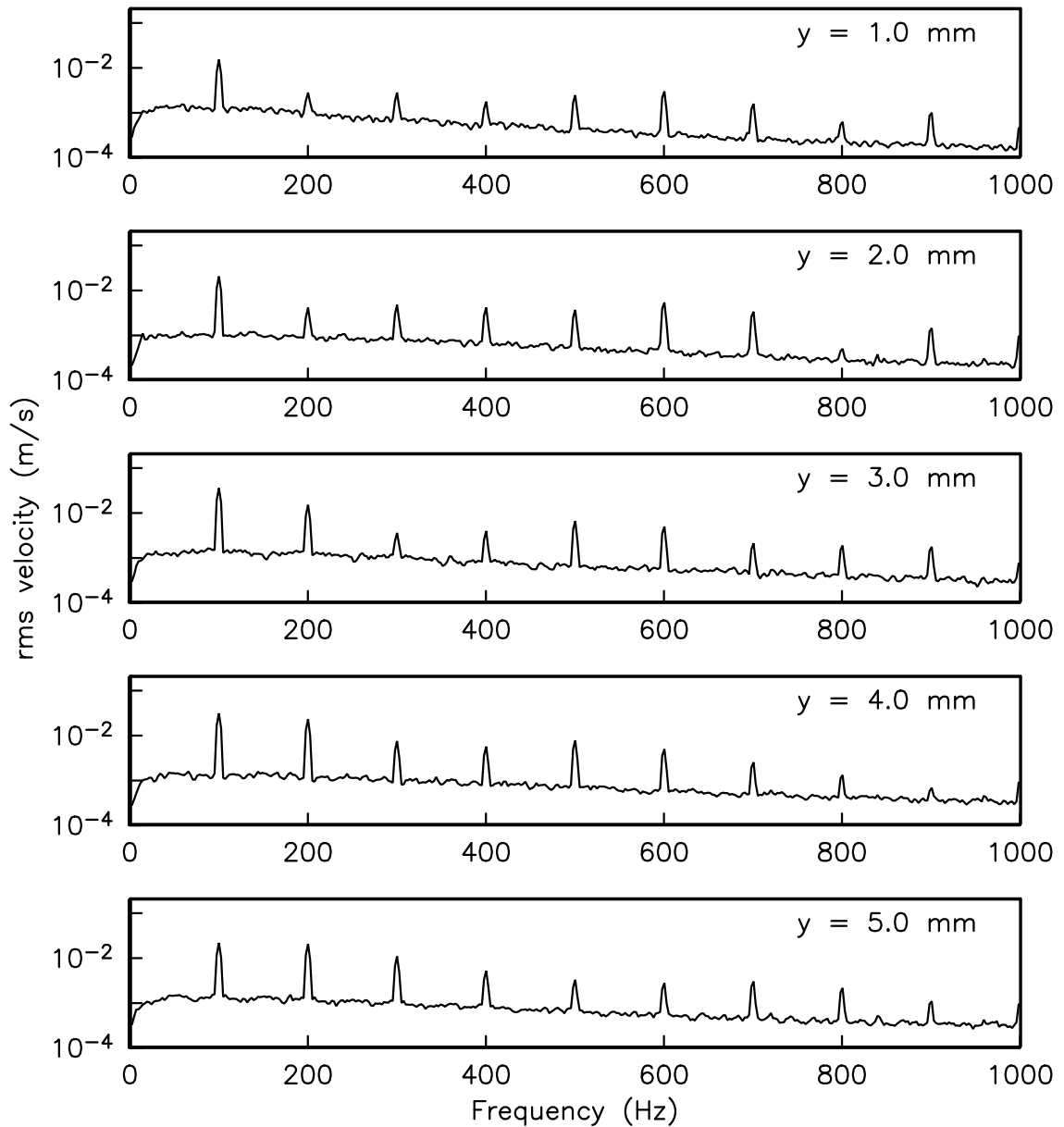
Figure 7.17. Power spectra for five wall normal distances at $x/C_x = 85\%$ for the controlled flow field at $Re_c = 50,000$ using an unsteady plasma actuator. The plasma actuator was a macor-based actuator and located at $x/C_x = 67.5\%$. The actuator amplitude was 24 kV. The excitation frequency was 100 Hz and the plasma duty cycle was 10%.

157
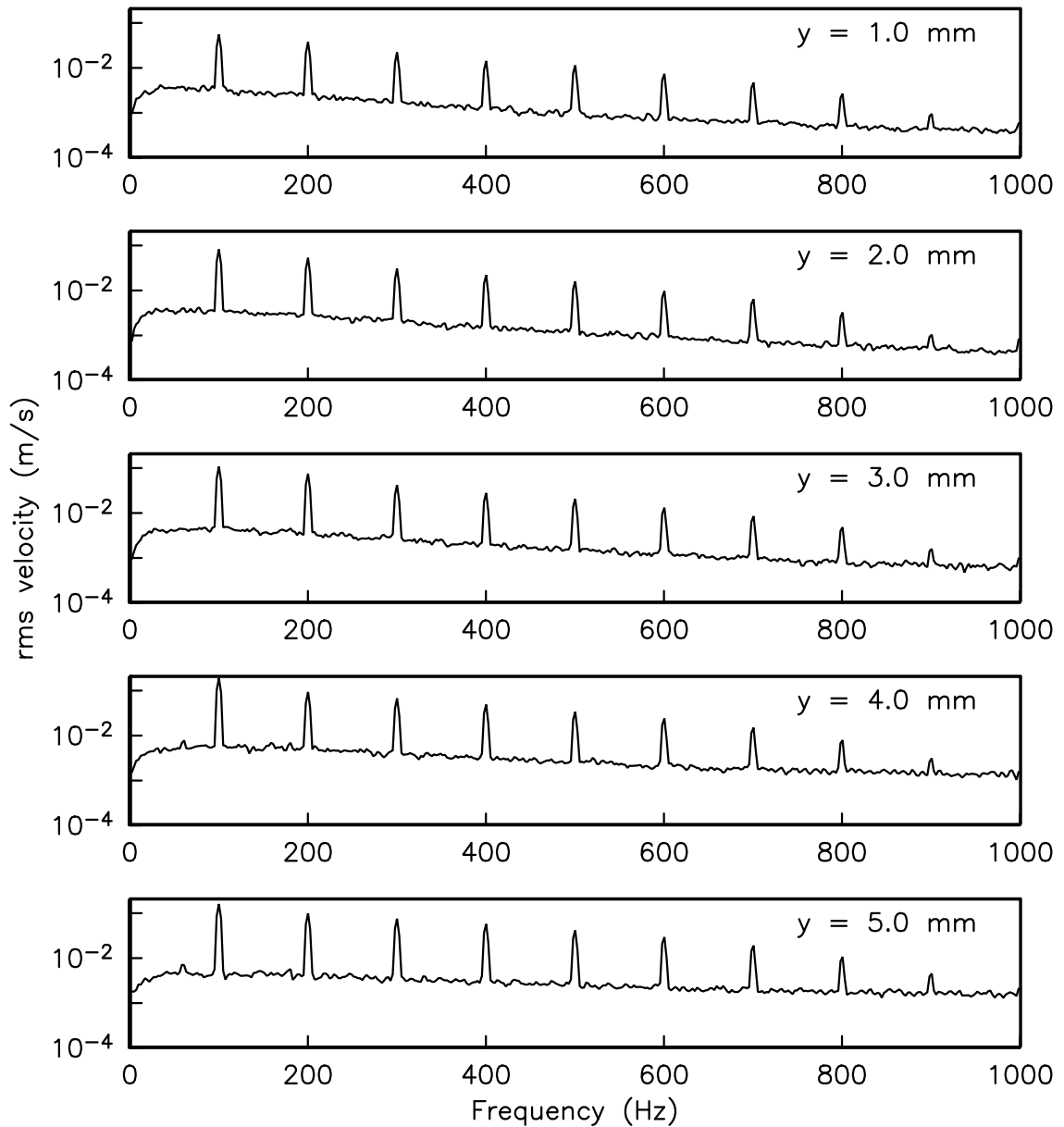
Figure 7.18. Power spectra for five wall normal distances at $x/C_x = 90\%$ for the controlled flow field at $Re_c = 50,000$ using an unsteady plasma actuator. The plasma actuator was a macor-based actuator and located at $x/C_x = 67.5\%$. The actuator amplitude was 24 kV. The excitation frequency was 100 Hz and the plasma duty cycle was 10%.

CHAPTER 8

CONCLUSIONS & RECOMMENDATIONS

8.1 Conclusions

Active boundary layer separation control has been successfully demonstrated on a low pressure turbine (LPT) blade using plasma actuators. The experiments were performed in a specially designed wind tunnel that hosts a generic LPT cascade consisting of nine "PakB" blades. The flow fields around "PakB" blades with and without separation control were thoroughly documented using flow visualization, pressure measurements, LDV measurements, and hot-wire measurements. The experimental conditions were chosen to give a range of chord Reynolds numbers from $10,000$ to $100,000$ and a range of the freestream turbulence intensities from $u'/U_\infty = 0.08\%$ to 2.85%. Plasma actuators were designed and applied to control the flow separation occurring on the suction surface of the "PakB" blade. Both steady and unsteady actuation were implemented and found to be effective at separation control. However, the mechanism is different between steady and unsteady actuators.

8.1.1 Flow Separation on "PakB" Blades

The blade surface pressure distributions were used to define a region of separation on the suction side of the "PakB" blades that depends on the freestream conditions. For the baseline flow (without separation control), the following conclusions can be made based on the experimental results:

159

- Flow separation was observed under all experimental conditions. For $Re_c \leqslant 25,000$, the flow separates and does not reattach. For $Re_c \geqslant 50,000$, the flow separates and reattaches to the blade, forming a separation bubble on the suction surface. The size of separation bubble decreases as the Reynolds number increases.

- The location of separation is insensitive to the freestream conditions and located at $x/C_x \approx 70\%$.

- The location of reattachment is sensitive to the freestream conditions, in particular, the Reynolds number. When the Reynolds number and/or the freestream turbulence intensity increase(s), the location of reattachment moves upstream.

8.1.2 Steady Plasma Actuators

For the steady plasma actuators, the effects of the actuator location, the actuator amplitude, the number of the actuators, and the orientation of the actuator electrodes were studied. A summary of the conclusions for the steady plasma actuators based on the experimental results are:

- The steady plasma actuators are the most effective when applied sightly upstream the location of separation.

- The effectiveness of the steady actuators is not sensitive to the orientation of the actuator electrodes.

- The steady plasma actuators have to be supplied with a voltage larger than a threshold value to show effect of separation control. However, the effect is saturated when the plasma amplitude is large enough.

- The control mechanism of the steady actuators was suggested to be turbulence tripping of the laminar separation flow.

8.1.3 Unsteady Plasma Actuators

For the unsteady actuators, the effects of the excitation frequency and the plasma duty cycle were studied. The wake profiles were measured to calculate the total pressure loss coefficient. The effectiveness of steady and unsteady actuators was compared. Flow visualization and power spectrum measurements were performed to examine the mechanism of the unsteady actuators. A summary of the conclusions for the unsteady actuators are:

- The unsteady plasma actuators are more effective than the steady ones.

- The lowest plasma duty cycle (10%) was as effective as the highest plasma duty cycle (50%) at the same excitation frequency. This indicates a four times saving in energy when compared to the highest duty cycle unsteady plasma actuators, or a nine time saving in energy when compared to the steady actuators.

- There exists an optimum excitation frequency $f_{optimum}$ at which the unsteady plasma actuator is the most effective. This optimum frequency is the one that makes the Strouhal number, defined as $S_t = f L_{sep}/U_{mid-channel}$, unity.

- Both flow visualization and the power spectra show that the control mechanism of the unsteady actuators is the generation of spanwise structures that promote mixing.

- The flow separation over "PakB" blades was completely eliminated using the most optimized unsteady operation when using a macor-based plasma actuator. The plasma actuator was located at $x/C_x = 67.5\%$. The actuator amplitude was 24 kV. The excitation frequency of the actuator was 100 Hz and the plasma duty cycle was 10%.

- A large improvement in total pressure loss coefficient was achieved at $Re_c = 25,000$ by operating an unsteady plasma actuator. However, there was only a slight improvement in total pressure loss coefficient at $Re_c = 50,000$. This is because the flow did not reattach to the blade trailing edge at $Re_c = 25,000$ without separation control. When the unsteady plasma actuator was operated, it reattached the flow to the blade trailing edge, thus significantly changing the flow direction at $Re_c = 25,000$. At $Re_c = 50,000$, the flow was naturally reattached to the blade trailing edge. When the unsteady actuator was operated, it decreased the size of the separation bubble but it had little effect on the flow direction.

8.2 Recommendations

Although flow separation control using steady and unsteady plasma actuators has been successfully demonstrated in this research work, there are further investigations that can be done. Here are some recommendations:

- A better dielectric material needs to be found for practical applications of the plasma actuators. Kapton has excellent electric properties but fails fairly quickly. Macor is very durable but its mechanical properties make it difficult to work with. The ideal dielectric material has to have excellent electric properties. It also has to be very durable and easy to work with.

- It has been suggested by the results that the control mechanism of steady actuators is turbulence tripping and that of unsteady actuators is mixing.

161

However, more work could be done to understand how plasma actuators interact with the flow. The instantaneous flow field when the plasma is operated can be measured using Particle Image Velocimetry (PIV). The structure of the vortices generated by the actuators can be captured, which will help to further understand the mechanism of the plasma actuators.

- It has been mentioned in some literature that the streamwise vortices is the most effective way to mix the low-momentum and high-momentum fluids. Streamwise plasma actuators were not tested in this research work due to the difficulty in making good smooth plasma arrays. The solder joints of the trial streamwise plasma actuators were acting like bumps to the flow and made the flow fully attached even when the plasma actuators were off. A new technique has to be developed to build smooth streamwise plasma actuator arrays.

- The flow speed in this research work is in the low subsonic range. For the low pressure turbine applications, the Mach number is playing an important role. New experiments can be designed and performed to examine the effect of the Mach number.

APPENDIX A

UNCERTAINTY ANALYSIS

A.1 Uncertainty Analysis Approach

The uncertainty in an experimental measurement typically consists of two elements: bias errors and precision errors. A bias error, B_u, is defined as "the average error in a series of repeated calibration accuracies" [?]. Conversely, a precision error, P_u, is defined as "a measure of the random variation to be expected during repeatability trials" [?]. Precision errors are estimated using data collected over a series of experimental measurements. The total error in a measurement may be estimated to a 95% confidence level as

$$u = \sqrt{B_u^2 + \left(S_{\nu,95}^t P_u\right)^2},\tag{A.1}$$

where S^t is the Student-t variable, and ν is the number of degrees of freedom in the measurement.

In this experiment, all uncertainty estimates are given at 95% confidence, and are computed through the Kline-McClintock root-sum-square method:

$$B_u = \sqrt{\sum_{j=1}^{N} B_{u_j}^2},\tag{A.2}$$

$$P_u = \sqrt{\sum_{j=1}^{N} P_{u_j}^2},\tag{A.3}$$

where B_{u_j} and P_{u_j} represent the jth bias and precision errors from N error sources.

To determine the uncertainty in an analytical result, errors are propagated through derivatives of the analytical relationship. For example, given the analytical function

$$g = g(\epsilon, \chi), \tag{A.4}$$

the uncertainty, u_g, can be computed through derivatives of g with respect to ϵ and χ, multiplied by the errors, u_ϵ and u_χ. Thus, the error, u_g, can be computed as

$$u_g = \sqrt{\left(\frac{\partial g}{\partial \epsilon} \cdot u_\epsilon\right)^2 + \left(\frac{\partial g}{\partial \chi} \cdot u_\chi\right)^2}. \tag{A.5}$$

A.2   Pressure Measurements

In this section, the uncertainty of the pressure measurements will be evaluated. The errors of the pressure measurements come from the pressure transducer and the A/D board used to acquire the pressure signal.

A.2.1   Pressure Transducer Error

The pressure transducer used in this experiment was made by Validyne Corporation. The model number is DP103. The companion carrier demodulator is Model CD23. The accuracy specifications for this pressure transducer are given in Table A.1

TABLE A.1

VALIDYNE PRESSURE TRANSDUCER SPECIFICATIONS

Error Source	Nominal Value
Full Scale Output (FS)	$\pm 2.2 in H_2 O$
Accuracy, $u_{accuracy}$	$\pm 0.25\% FS$
Temp. Effect on Zero, u_{zero}	$1\% FS/100°F$
Temp. Effect on Span, u_{span}	5%Typical Pressure$/100°F$

The uncertainty due to the pressure transducer inaccuracy is computed as

$$
\begin{aligned}
B_{u_{11}} &= u_{accuracy} \times FS \\
&= 0.25\% \times 2.2 \\
&= 5.5 \times 10^{-3} (inH_2O).
\end{aligned}
\tag{A.6}
$$

The uncertainty due to the temperature variation can be evaluated as following. The typical temperature variation in my experimental environment is $\Delta T = 4°F$. The typical pressure in this research work is 0.72 inH$_2$O. Thus the uncertainty due to the temperature variation is

$$
\begin{aligned}
B_{u_{12}} &= \sqrt{\left(u_{zero} \times \frac{\Delta T}{100}\right)^2 + \left(u_{span} \times \frac{\Delta T}{100}\right)^2} \\
&= \sqrt{\left(1\% \times 2.2 \times \frac{4}{100}\right)^2 + \left(5\% \times 0.72 \times \frac{4}{100}\right)^2} \\
&= 1.688 \times 10^{-3} (inH_2O).
\end{aligned}
\tag{A.7}
$$

Therefore, the total uncertainty from the pressure transducer is

$$
\begin{aligned}
B_{u_1} &= \sqrt{B_{u_{11}}^2 + B_{u_{12}}^2} \\
&= \sqrt{(5.5 \times 10^{-3})^2 + (1.688 \times 10^{-3})^2} \\
&= 5.753 \times 10^{-3} (inH_2O) \\
&= 0.799\% (Typical).
\end{aligned}
\tag{A.8}
$$

A.2.2 Analog-to-Digital Acquisition Error

A PowerDAQ PD2-MFS-8-500/14DG A/D board was used to acquire data in this research work. The accuracy specifications of this board are given in Table A.2.

Due to the number of car bits, a quantization error was created during digitization of the analog voltage signal. The resolution of this digitized signal is

$$
\begin{aligned}
u_{resolution} &= \frac{2 \times FS}{2^{14}} \\
&= 1.22 \times 10^{-3} V.
\end{aligned}
\tag{A.9}
$$

165

POWERDAQ PD2-MFS-8-500/14DG A/D BOARD SPECIFICATIONS

Error Source	Nominal Value
Full Scale Voltage (FS)	$10V$
Number of Bits	14
Input Range	$\pm 5V$
Accuracy, $u_{accuracy}$	$\pm 0.25\% FS$

With the signal resolution known, the quantization error incurred during the A/D process is

$$
\begin{aligned}
u_Q &= \frac{1}{2} \times u_{resolution} \\
&= 0.61 \times 10^{-3} V.
\end{aligned} \tag{A.10}
$$

Thus, as shown in Equation A.11, the total uncertainty in the digitized voltage, B_{u_2}, is found to be $2.501 \times 10^{-2} V$, or $B_{u_2} = 1.25\%$ of the typical voltage ($2.0V$).

$$
\begin{aligned}
B_{u_2} &= \sqrt{u_Q^2 + u_{accuracy}^2} \\
&= \sqrt{(0.61 \times 10^{-3})^2 + (0.25\% \times 10)^2} \\
B_{u_2} &= 2.501 \times 10^{-2} V = 1.25\% (Typical).
\end{aligned} \tag{A.11}
$$

A.2.3   Calibration Precision Error

At each calibrated pressure, 8192 transducer voltage measurements were collected and averaged. As such, a precision error was incurred in the averaged calibration voltages. This precision error is proportional to the standard deviation of means of the measured voltages at each calibration pressure. The standard deviation of the means, $S_{\bar{x}}$, is defined as

$$
S_{\bar{x}} = \frac{S_x}{\sqrt{N}}, \tag{A.12}
$$

where

$$S_x = \sqrt{\frac{1}{N-1}\sum_{j=1}^{N}(\bar{E} - E_j)^2}.$$ (A.13)

In Equation A.12 and A.13, S_x is the standard deviation, $\bar{E}$ is the average voltage, E_j is the voltage from the jth measurement, and N is the number of measurements ($N = 8192$). Using the calibration of transducer, the standard deviation of the means was found to be $S_{\bar{x}} = 3.72 \times 10^{-3}V$. Since the calibrated transducer constant is $m = 0.902$ inH$_2$O/V, the calibration precision error is computed as

$$
\begin{aligned}
P_{u_3} &= m \times S_{\bar{x}} \\
&= 0.902 inH_2O/V \times 3.72 \times 10^{-3}V \\
&= 3.355 \times 10^{-3} inH_2O \\
&= 0.466\% (Typical).
\end{aligned}
$$ (A.14)

A.2.4   Overall Uncertainty of Pressure Measurements

The overall uncertainty of pressure measurements can be calculated from the bias errors and the calibration error using Equation A.1. Also, when computing the overall uncertainty, a student-t value of $S_{\nu,95}^t = 2.0$ is used. Therefore, the overall uncertainty of pressure measurements is

$$
\begin{aligned}
B_{up} &= \sqrt{B_{u_1}^2 + B_{u_2}^2 + (S_{\nu,95}^t P_{u_2})^2} \\
&= \sqrt{(0.799\%)^2 + (1.25\%)^2 + (2.0 \times 0.466\%)^2} \\
&= 1.75\% (Typical).
\end{aligned}
$$ (A.15)

APPENDIX B

TRAVERSING COORDINATES FOR LDV MEASUREMENTS

B.1 Coordinate System

The triangular beam of the LDV system was aligned parallel to the inlet flow direction. Thus the x-axis of the coordinate system was parallel to the inlet flow direction, as shown in Figure B.1. The y-axis was perpendicular to the x-axis. The origin of the coordinate system was set at the specified streamwise location on the suction surface of the "PakB" blade.
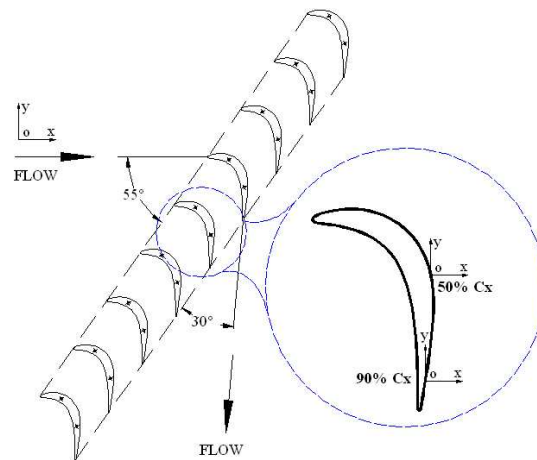
Figure B.1. The coordinate system used in LDV measurements.

B.2 Traversing Coordinates at Different Streamwise Locations

TABLE B.1

TRAVERSING COORDINATES AT $50\%C_x$

Dist. (mm)	x (mm)	y (mm)	Dist. (mm)	x (mm)	y (mm)
0.00	0.000	0.000			
0.10	0.080	0.060	4.10	3.273	2.469
0.20	0.160	0.120	4.20	3.353	2.529
0.30	0.239	0.181	4.30	3.433	2.590
0.40	0.319	0.241	4.40	3.513	2.650
0.50	0.399	0.301	4.50	3.592	2.710
0.60	0.479	0.361	4.60	3.672	2.770
0.70	0.559	0.422	4.70	3.752	2.831
0.80	0.639	0.482	4.80	3.832	2.891
0.90	0.718	0.542	4.90	3.912	2.951
1.00	0.798	0.602	5.00	3.992	3.011
1.10	0.878	0.662	5.10	4.071	3.071
1.20	0.958	0.723	5.20	4.151	3.132
1.30	1.038	0.783	5.30	4.231	3.192
1.40	1.118	0.843	5.40	4.311	3.252
1.50	1.197	0.903	5.50	4.391	3.312
1.60	1.277	0.964	5.60	4.471	3.373
1.70	1.357	1.024	5.70	4.550	3.433
1.80	1.437	1.084	5.80	4.630	3.493
1.90	1.517	1.144	5.90	4.710	3.553
2.00	1.597	1.204	6.00	4.790	3.613
2.10	1.676	1.265	6.10	4.870	3.674
2.20	1.756	1.325	6.20	4.949	3.734
2.30	1.836	1.385	6.30	5.029	3.794
2.40	1.916	1.445	6.40	5.109	3.854
2.50	1.996	1.506	6.50	5.189	3.915
2.60	2.076	1.566	6.60	5.269	3.975
2.70	2.155	1.626	6.70	5.349	4.035
2.80	2.235	1.686	6.80	5.428	4.095
2.90	2.315	1.747	6.90	5.508	4.156
3.00	2.395	1.807	7.00	5.588	4.216
3.10	2.475	1.867	7.10	5.668	4.276
3.20	2.555	1.927	7.20	5.748	4.336
3.30	2.634	1.987	7.30	5.828	4.396
3.40	2.714	2.048	7.40	5.907	4.457
3.50	2.794	2.108	7.50	5.987	4.517
3.60	2.874	2.168	7.60	6.067	4.577
3.70	2.954	2.228	7.70	6.147	4.637
3.80	3.034	2.289	7.80	6.227	4.698
3.90	3.113	2.349	7.90	6.307	4.758
4.00	3.193	2.409	8.00	6.386	4.818

TABLE B.2

TRAVERSING COORDINATES AT $60\%C_x$

Dist. (mm)	x (mm)	y (mm)	Dist. (mm)	x (mm)	y (mm)
0.00	0.000	0.000			
0.10	0.094	0.034	4.10	3.857	1.391
0.20	0.188	0.068	4.20	3.951	1.425
0.30	0.282	0.102	4.30	4.045	1.459
0.40	0.376	0.136	4.40	4.139	1.493
0.50	0.470	0.170	4.50	4.233	1.527
0.60	0.564	0.204	4.60	4.327	1.561
0.70	0.658	0.237	4.70	4.421	1.594
0.80	0.753	0.271	4.80	4.515	1.628
0.90	0.847	0.305	4.90	4.609	1.662
1.00	0.941	0.339	5.00	4.703	1.696
1.10	1.035	0.373	5.10	4.798	1.730
1.20	1.129	0.407	5.20	4.892	1.764
1.30	1.223	0.441	5.30	4.986	1.798
1.40	1.317	0.475	5.40	5.080	1.832
1.50	1.411	0.509	5.50	5.174	1.866
1.60	1.505	0.543	5.60	5.268	1.900
1.70	1.599	0.577	5.70	5.362	1.934
1.80	1.693	0.611	5.80	5.456	1.968
1.90	1.787	0.645	5.90	5.550	2.002
2.00	1.881	0.679	6.00	5.644	2.036
2.10	1.975	0.712	6.10	5.738	2.069
2.20	2.070	0.746	6.20	5.832	2.103
2.30	2.164	0.780	6.30	5.926	2.137
2.40	2.258	0.814	6.40	6.020	2.171
2.50	2.352	0.848	6.50	6.115	2.205
2.60	2.446	0.882	6.60	6.209	2.239
2.70	2.540	0.916	6.70	6.303	2.273
2.80	2.634	0.950	6.80	6.397	2.307
2.90	2.728	0.984	6.90	6.491	2.341
3.00	2.822	1.018	7.00	6.585	2.375
3.10	2.916	1.052	7.10	6.679	2.409
3.20	3.010	1.086	7.20	6.773	2.443
3.30	3.104	1.120	7.30	6.867	2.477
3.40	3.198	1.153	7.40	6.961	2.510
3.50	3.292	1.187	7.50	7.055	2.544
3.60	3.386	1.221	7.60	7.149	2.578
3.70	3.481	1.255	7.70	7.243	2.612
3.80	3.575	1.289	7.80	7.337	2.646
3.90	3.669	1.323	7.90	7.431	2.680
4.00	3.763	1.357	8.00	7.526	2.714

TABLE B.3

TRAVERSING COORDINATES AT $70\%C_x$

Dist. (mm)	x (mm)	y (mm)	Dist. (mm)	x (mm)	y (mm)
0.00	0.000	0.000			
0.10	0.100	0.010	4.10	4.080	0.406
0.20	0.199	0.020	4.20	4.179	0.416
0.30	0.299	0.030	4.30	4.279	0.425
0.40	0.398	0.040	4.40	4.378	0.435
0.50	0.498	0.049	4.50	4.478	0.445
0.60	0.597	0.059	4.60	4.577	0.455
0.70	0.697	0.069	4.70	4.677	0.465
0.80	0.796	0.079	4.80	4.776	0.475
0.90	0.896	0.089	4.90	4.876	0.485
1.00	0.995	0.099	5.00	4.975	0.495
1.10	1.095	0.109	5.10	5.075	0.505
1.20	1.194	0.119	5.20	5.174	0.515
1.30	1.294	0.129	5.30	5.274	0.524
1.40	1.393	0.139	5.40	5.373	0.534
1.50	1.493	0.148	5.50	5.473	0.544
1.60	1.592	0.158	5.60	5.573	0.554
1.70	1.692	0.168	5.70	5.672	0.564
1.80	1.791	0.178	5.80	5.772	0.574
1.90	1.891	0.188	5.90	5.871	0.584
2.00	1.990	0.198	6.00	5.971	0.594
2.10	2.090	0.208	6.10	6.070	0.604
2.20	2.189	0.218	6.20	6.170	0.613
2.30	2.289	0.228	6.30	6.269	0.623
2.40	2.388	0.237	6.40	6.369	0.633
2.50	2.488	0.247	6.50	6.468	0.643
2.60	2.587	0.257	6.60	6.568	0.653
2.70	2.687	0.267	6.70	6.667	0.663
2.80	2.786	0.277	6.80	6.767	0.673
2.90	2.886	0.287	6.90	6.866	0.683
3.00	2.985	0.297	7.00	6.966	0.693
3.10	3.085	0.307	7.10	7.065	0.702
3.20	3.184	0.317	7.20	7.165	0.712
3.30	3.284	0.327	7.30	7.264	0.722
3.40	3.383	0.336	7.40	7.364	0.732
3.50	3.483	0.346	7.50	7.463	0.742
3.60	3.582	0.356	7.60	7.563	0.752
3.70	3.682	0.366	7.70	7.662	0.762
3.80	3.781	0.376	7.80	7.762	0.772
3.90	3.881	0.386	7.90	7.861	0.782
4.00	3.980	0.396	8.00	7.961	0.792

TABLE B.4

TRAVERSING COORDINATES AT 75%C_x

Dist. (mm)	x (mm)	y (mm)	Dist. (mm)	x (mm)	y (mm)
0.00	0.000	0.000			
0.10	0.100	-0.002	4.10	4.099	-0.064
0.20	0.200	-0.003	4.20	4.199	-0.066
0.30	0.300	-0.005	4.30	4.299	-0.067
0.40	0.400	-0.006	4.40	4.399	-0.069
0.50	0.500	-0.008	4.50	4.499	-0.071
0.60	0.600	-0.009	4.60	4.599	-0.072
0.70	0.700	-0.011	4.70	4.699	-0.074
0.80	0.800	-0.013	4.80	4.799	-0.075
0.90	0.900	-0.014	4.90	4.899	-0.077
1.00	1.000	-0.016	5.00	4.999	-0.078
1.10	1.100	-0.017	5.10	5.099	-0.080
1.20	1.200	-0.019	5.20	5.199	-0.082
1.30	1.300	-0.020	5.30	5.299	-0.083
1.40	1.400	-0.022	5.40	5.399	-0.085
1.50	1.500	-0.024	5.50	5.499	-0.086
1.60	1.600	-0.025	5.60	5.599	-0.088
1.70	1.700	-0.027	5.70	5.699	-0.089
1.80	1.800	-0.028	5.80	5.799	-0.091
1.90	1.900	-0.030	5.90	5.899	-0.093
2.00	2.000	-0.031	6.00	5.999	-0.094
2.10	2.100	-0.033	6.10	6.099	-0.096
2.20	2.200	-0.035	6.20	6.199	-0.097
2.30	2.300	-0.036	6.30	6.299	-0.099
2.40	2.400	-0.038	6.40	6.399	-0.100
2.50	2.500	-0.039	6.50	6.499	-0.102
2.60	2.600	-0.041	6.60	6.599	-0.104
2.70	2.700	-0.042	6.70	6.699	-0.105
2.80	2.800	-0.044	6.80	6.799	-0.107
2.90	2.900	-0.046	6.90	6.899	-0.108
3.00	3.000	-0.047	7.00	6.999	-0.110
3.10	3.100	-0.049	7.10	7.099	-0.111
3.20	3.200	-0.050	7.20	7.199	-0.113
3.30	3.300	-0.052	7.30	7.299	-0.115
3.40	3.400	-0.053	7.40	7.399	-0.116
3.50	3.500	-0.055	7.50	7.499	-0.118
3.60	3.600	-0.057	7.60	7.599	-0.119
3.70	3.700	-0.058	7.70	7.699	-0.121
3.80	3.800	-0.060	7.80	7.799	-0.122
3.90	3.900	-0.061	7.90	7.899	-0.124
4.00	3.999	-0.063	8.00	7.999	-0.126

TABLE B.5

TRAVERSING COORDINATES AT $80\%C_x$

Dist. (mm)	x (mm)	y (mm)	Dist. (mm)	x (mm)	y (mm)
0.00	0.000	0.000			
0.10	0.100	-0.008	4.10	4.086	-0.335
0.20	0.199	-0.016	4.20	4.186	-0.343
0.30	0.299	-0.024	4.30	4.286	-0.351
0.40	0.399	-0.033	4.40	4.385	-0.359
0.50	0.498	-0.041	4.50	4.485	-0.367
0.60	0.598	-0.049	4.60	4.585	-0.375
0.70	0.698	-0.057	4.70	4.684	-0.384
0.80	0.797	-0.065	4.80	4.784	-0.392
0.90	0.897	-0.073	4.90	4.884	-0.400
1.00	0.997	-0.082	5.00	4.983	-0.408
1.10	1.096	-0.090	5.10	5.083	-0.416
1.20	1.196	-0.098	5.20	5.183	-0.424
1.30	1.296	-0.106	5.30	5.282	-0.432
1.40	1.395	-0.114	5.40	5.382	-0.441
1.50	1.495	-0.122	5.50	5.482	-0.449
1.60	1.595	-0.131	5.60	5.581	-0.457
1.70	1.694	-0.139	5.70	5.681	-0.465
1.80	1.794	-0.147	5.80	5.781	-0.473
1.90	1.894	-0.155	5.90	5.880	-0.481
2.00	1.993	-0.163	6.00	5.980	-0.490
2.10	2.093	-0.171	6.10	6.080	-0.498
2.20	2.193	-0.180	6.20	6.179	-0.506
2.30	2.292	-0.188	6.30	6.279	-0.514
2.40	2.392	-0.196	6.40	6.379	-0.522
2.50	2.492	-0.204	6.50	6.478	-0.530
2.60	2.591	-0.212	6.60	6.578	-0.539
2.70	2.691	-0.220	6.70	6.678	-0.547
2.80	2.791	-0.228	6.80	6.777	-0.555
2.90	2.890	-0.237	6.90	6.877	-0.563
3.00	2.990	-0.245	7.00	6.977	-0.571
3.10	3.090	-0.253	7.10	7.076	-0.579
3.20	3.189	-0.261	7.20	7.176	-0.588
3.30	3.289	-0.269	7.30	7.276	-0.596
3.40	3.389	-0.277	7.40	7.375	-0.604
3.50	3.488	-0.286	7.50	7.475	-0.612
3.60	3.588	-0.294	7.60	7.575	-0.620
3.70	3.688	-0.302	7.70	7.674	-0.628
3.80	3.787	-0.310	7.80	7.774	-0.636
3.90	3.887	-0.318	7.90	7.874	-0.645
4.00	3.987	-0.326	8.00	7.973	-0.653

TABLE B.6

TRAVERSING COORDINATES AT $85\% C_x$

Dist. (mm)	x (mm)	y (mm)	Dist. (mm)	x (mm)	y (mm)
0.00	0.000	0.000			
0.10	0.099	-0.012	4.10	4.072	-0.480
0.20	0.199	-0.023	4.20	4.171	-0.492
0.30	0.298	-0.035	4.30	4.270	-0.504
0.40	0.397	-0.047	4.40	4.370	-0.516
0.50	0.497	-0.059	4.50	4.469	-0.527
0.60	0.596	-0.070	4.60	4.568	-0.539
0.70	0.695	-0.082	4.70	4.668	-0.551
0.80	0.794	-0.094	4.80	4.767	-0.562
0.90	0.894	-0.105	4.90	4.866	-0.574
1.00	0.993	-0.117	5.00	4.966	-0.586
1.10	1.092	-0.129	5.10	5.065	-0.598
1.20	1.192	-0.141	5.20	5.164	-0.609
1.30	1.291	-0.152	5.30	5.263	-0.621
1.40	1.390	-0.164	5.40	5.363	-0.633
1.50	1.490	-0.176	5.50	5.462	-0.644
1.60	1.589	-0.187	5.60	5.561	-0.656
1.70	1.688	-0.199	5.70	5.661	-0.668
1.80	1.788	-0.211	5.80	5.760	-0.680
1.90	1.887	-0.223	5.90	5.859	-0.691
2.00	1.986	-0.234	6.00	5.959	-0.703
2.10	2.086	-0.246	6.10	6.058	-0.715
2.20	2.185	-0.258	6.20	6.157	-0.726
2.30	2.284	-0.269	6.30	6.257	-0.738
2.40	2.383	-0.281	6.40	6.356	-0.750
2.50	2.483	-0.293	6.50	6.455	-0.762
2.60	2.582	-0.305	6.60	6.555	-0.773
2.70	2.681	-0.316	6.70	6.654	-0.785
2.80	2.781	-0.328	6.80	6.753	-0.797
2.90	2.880	-0.340	6.90	6.852	-0.808
3.00	2.979	-0.352	7.00	6.952	-0.820
3.10	3.079	-0.363	7.10	7.051	-0.832
3.20	3.178	-0.375	7.20	7.150	-0.844
3.30	3.277	-0.387	7.30	7.250	-0.855
3.40	3.377	-0.398	7.40	7.349	-0.867
3.50	3.476	-0.410	7.50	7.448	-0.879
3.60	3.575	-0.422	7.60	7.548	-0.890
3.70	3.675	-0.434	7.70	7.647	-0.902
3.80	3.774	-0.445	7.80	7.746	-0.914
3.90	3.873	-0.457	7.90	7.846	-0.926
4.00	3.972	-0.469	8.00	7.945	-0.937

TABLE B.7

TRAVERSING COORDINATES AT $90\%C_x$

Dist. (mm)	x (mm)	y (mm)	Dist. (mm)	x (mm)	y (mm)
0.00	0.000	0.000			
0.10	0.099	-0.014	4.10	4.058	-0.588
0.20	0.198	-0.029	4.20	4.157	-0.603
0.30	0.297	-0.043	4.30	4.256	-0.617
0.40	0.396	-0.057	4.40	4.354	-0.631
0.50	0.495	-0.072	4.50	4.453	-0.646
0.60	0.594	-0.086	4.60	4.552	-0.660
0.70	0.693	-0.100	4.70	4.651	-0.674
0.80	0.792	-0.115	4.80	4.750	-0.689
0.90	0.891	-0.129	4.90	4.849	-0.703
1.00	0.990	-0.143	5.00	4.948	-0.717
1.10	1.089	-0.158	5.10	5.047	-0.732
1.20	1.188	-0.172	5.20	5.146	-0.746
1.30	1.287	-0.186	5.30	5.245	-0.760
1.40	1.386	-0.201	5.40	5.344	-0.775
1.50	1.484	-0.215	5.50	5.443	-0.789
1.60	1.583	-0.230	5.60	5.542	-0.803
1.70	1.682	-0.244	5.70	5.641	-0.818
1.80	1.781	-0.258	5.80	5.740	-0.832
1.90	1.880	-0.273	5.90	5.839	-0.846
2.00	1.979	-0.287	6.00	5.938	-0.861
2.10	2.078	-0.301	6.10	6.037	-0.875
2.20	2.177	-0.316	6.20	6.136	-0.889
2.30	2.276	-0.330	6.30	6.235	-0.904
2.40	2.375	-0.344	6.40	6.334	-0.918
2.50	2.474	-0.359	6.50	6.433	-0.932
2.60	2.573	-0.373	6.60	6.532	-0.947
2.70	2.672	-0.387	6.70	6.631	-0.961
2.80	2.771	-0.402	6.80	6.730	-0.975
2.90	2.870	-0.416	6.90	6.829	-0.990
3.00	2.969	-0.430	7.00	6.928	-1.004
3.10	3.068	-0.445	7.10	7.027	-1.019
3.20	3.167	-0.459	7.20	7.126	-1.033
3.30	3.266	-0.473	7.30	7.224	-1.047
3.40	3.365	-0.488	7.40	7.323	-1.062
3.50	3.464	-0.502	7.50	7.422	-1.076
3.60	3.563	-0.516	7.60	7.521	-1.090
3.70	3.662	-0.531	7.70	7.620	-1.105
3.80	3.761	-0.545	7.80	7.719	-1.119
3.90	3.860	-0.559	7.90	7.818	-1.133
4.00	3.959	-0.574	8.00	7.917	-1.148

BIBLIOGRAPHY

[1] Bearman, P. W., and Harvey, J. K., *Control of Circular Cylinder Flow by the Use of Dimples*, AIAA Journal, October 1993, 1993.

[2] Bons, J.P., Sondergaard, R., and Rivir, R.B., *Control of Low Pressure Turbine Separation Using Vortex Generator Jets*, AIAA-1999-0367, 1999.

[3] Bons, J.P., Sondergaard, R., and Rivir, R.B., *Turbine Separation Control Using Pulsed Vortex Generator Jets*, Vol. 123, Journal of Turbomachinery, April, 2001.

[4] Byerley, A. R., Störmer, O., Baughn, J. W., Simon, T. W., Van Treuren, K. W., and List, J., *Using Gurney Flaps to Control Laminar Separation on Linear Cascade Blades*, ASME GT-2002-30662, 2002.

[5] Corke, T. C., and Matlis, E., *Phased Plasma Arrays for Unsteady Flow Control*, AIAA Paper, AIAA-2000-2323, 2000.

[6] Dorney, D. J., and Ashpis, D. E., *Study of Low Reynolds Number Effects on the Losses in Low-Pressure Turbine Blade Rows*, AIAA Paper, AIAA-1998-3575, 1998.

[7] Dorney, D. J., Ashpis, D. E., Halstead, D. E., and Wisler, D. C., *Study of Boundary Layer Development in a Two-Stage Low-Pressure Turbine*, AIAA Paper, AIAA-1999-0742, 1999.

[8] Halstead, D. E., Wisler, D. C., Okiishi, T. H., Walker, G. J., Hodson, H. P., and Shin, H. W., *Boundary Layer Development in Axial compressors and Turbines Part 1 of 4: Composite Picture*, ASME 95-GT-461, 1995.

[9] Halstead, D. E., Wisler, D. C., Okiishi, T. H., Walker, G. J., Hodson, H. P., and Shin, H. W., *Boundary Layer Development in Axial compressors and Turbines Part 2 of 4: Compressors*, ASME 95-GT-462, 1995.

[10] Halstead, D. E., Wisler, D. C., Okiishi, T. H., Walker, G. J., Hodson, H. P., and Shin, H. W., *Boundary Layer Development in Axial compressors and Turbines Part 3 of 4: LP Turbines*, ASME 95-GT-463, 1995.

[11] Halstead, D. E., Wisler, D. C., Okiishi, T. H., Walker, G. J., Hodson, H. P., and Shin, H. W., *Boundary Layer Development in Axial compressors and Turbines Part 4 of 4: Computations & Analysis*, ASME 95-GT-464, 1995.

[12] Hollon, B., and Jamey, J., *Experimental Investigation of Separation on Low Pressure Turbine Blades*, AIAA Paper, AIAA-2001-0447, 2001.

[13] Hollon, B., and Jamey, J., *Flow Visualization of Separation and Transition in a Low Pressure Turbine Blade Cascade Model*, Journal of Turbomachinery.

[14] Huang, J., Corke, T. C., and Thomas, F. O., *Plasma Actuators for Separation Control of Low Pressure Turbine Blades*, AIAA Paper, AIAA-2003-1027, 2003.

[15] Huang, P. G., and Xiong, G., *Physics and Prediction of Reynolds Number and Freestream Turbulence Effects for Flows in a Low-Pressure Turbine*, AIAA Journal, March 1999, 1999.

[16] Lake, J.P., King, P.I., and Rivir, R.B., *Reduction of Separation Losses on a Turbine Blade with Low Reynolds Number*, AIAA-1999-0242, 1999.

[17] Lake, J.P., King, P.I., and Rivir, R.B., *Low Reynolds Number Loss Reduction on Turbine Blades with Dimples and V-Grooves*, AIAA-2000-0738, 2000.

[18] McLaughlin, T., Enloe, C., and VanDyken, R., *Mechanisms and Responses of a Single Dielectric Barrier Plasma*, AIAA Paper, AIAA-2003-1021, 2003.

[19] Orlov, D., Erturk, E., Post, M., and Corke, T., *DNS Modeling of Plasma Array Flow Actuators*, Bulletin of the American Physical Society Fluid Dynamics Division, Annual Meeting, 2001.

[20] Orlov, D., Erturk, Corke, T., and Post, M., *DNS Modeling of Plasma Array Flow Actuators*, Bulletin of the American Physical Society Fluid Dynamics Division, Annual Meeting, 2002.

[21] Post, M. L., *Phased plasma actuators for unsteady flow control*, M. S. Thesis, University of Notre Dame, 2001.

[22] Qiu, S., and Simon, T., *An Experimental Investigation of Transition as Applied to Low Pressure Turbine Suction Surface Flows*, ASME 97-GT-455, 1997.

[23] Romeo, Susan-Resiga, *Private Communication*, "Politehnica" University of Timisoara, Romania, 2002.

[24] Sharma, *Impact of Reynolds Number on Low Pressure Turbine Performance*, NASA CP-1998-206958, 65-70, 1998.

[25] Schlichting, H., *Boundary Layer Theory*, Seventh Edition, McGraw-Hill Inc., 1987.

[26] Shyne, R. J., *Experimental Study of Boundary Layer Behavior in a Simulated Low Pressure Turbine*, NASA/TM-1998-208503, October, 1998.

[27] Sohn, K. H., and DeWitt, K. J., *Experimental Study of Transitional Flow Behavior in a Simulated Low Pressure Turbine*, NASA report, August, 1998.

[28] Sohn, K. H., Shyne, R. J., and DeWitt, K. J., *Experimental Investigation of Boundary Layer Behavior in a Simulated Low Pressure Turbine*, ASME 98-GT-34, 1998.

[29] Solomon, W. J., *Boundary Layer Development in Multistage Low Pressure Turbines*, September 1998, 1998.

[30] Suzen, Y. B., Xiong, G., and Huang, P. G., *Predictions of Transitional Flows in a Low-Pressure Turbine Using an Intermittency Transport Equation*, AIAA Paper, AIAA-2000-2654, 2000.

[31] Volino, R. J., *Separated Flow Transition under Simulated Low Pressure Turbine Airfoil Conditions: Part 1 - Mean Flow and Turbulence Statistics*, ASME GT-2002-30236, 2002.

[32] Volino, R. J., *Separated Flow Transition under Simulated Low Pressure Turbine Airfoil Conditions: Part 2 - Turbulence Spectra*, ASME GT-2002-30236, 2002.

[33] Walker, G. J., Hughes, J. D., and Solomon, W. J., *Periodic Transition on an Axial Compressor Stator - Incidence and Clocking Effects Part I - Experimental Data*, ASME 98-GT-363, 1998.

[34] Walker, G. J., Hughes, J. D., and Solomon, W. J., *Periodic Transition on an Axial Compressor Stator - Incidence and Clocking Effects Part II - Transition Onset Predictions*, ASME 98-GT-364, 1998.

[35] White, F. M., *Viscous Fluid Flow*, McGraw-Hill Inc., 1991.